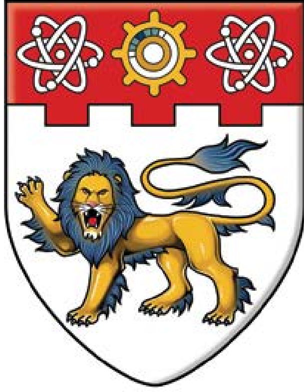

MODELING, OPTIMIZATION AND THERMAL CHARACTERIZATION OF MICROPILLAR EVAPORATOR BASED HIGH PERFORMANCE SILICON VAPOR CHAMBER

WEI MENGYAO

SCHOOL OF ELECTRICAL AND ELECTRONIC ENGINEERING

A thesis submitted to the Nanyang Technological University in partial fulfillment of the requirement for the degree of Doctor of Philosophy

2017

Acknowledgement

First of all, I owe my deepest gratitude to my supervisors, Prof Tan Chuan Seng and Prof Evelyn N. Wang. Without their continuous guidance, strong support, valuable suggestions and encouragement, the completion of this research was not possible. Their immense knowledge and expertise in extensive areas are strongly appreciated.

I wish to acknowledge my thesis advisor committee, Prof Edwin Teo and Prof Holden Li, for providing constructive comments and broadening my horizon in different perspectives that made my research more comprehensive and effective.

I would like to offer my special thanks to my labmates, Dr. He Bin, Dr. Liang Qian, Dr. Sivanand Somasundaram, Dr. Dion Antao, and Dr. Zhu Yangying, for their valuable support during the experiment conduction processes and for always being open for discussion. They were great friends, teachers who accompanied me, taught me and influenced me in various aspects of my life. I would also like to extend my thanks to the technicians, Dr. Chong Gang Yih, Ms. Ngo Ling Ling, Mr. Chung Kowk Fai and Mr. Mohamad Shamsul Bin Mohamad, in Nanyang NanoFabrication Center (N2FC) Cleanroom 1 (CR1) and Cleanroom 2 (CR2), for training me in cleanroom equipment operation and helping me to solve the problems encountered during microfabrication process. I am also indebted to many of my colleagues in Singapore-MIT Alliance for Research and Technology Center (SMART) for supporting me in conducting the thermal tests in the lab and inspiring me mentally.

Moreover, funding support from National Research Foundation (NRF) Singapore through Singapore MIT Alliance for Research and Technology (SMART) Center's Low Energy Electronic Systems (LEES) IRG is acknowledged.

Last but not least, I am also deeply grateful to my parents and my boyfriend Yan Jun, for their eternal and warmest inspiration during my Ph.D. study. They were always by my side to provide me endless love, blessing, and encouragement that equipped me with confidence. I am also thankful to my friends in Singapore and Boston, especially Li Luying and Zhu Di, who brought me countless happiness and helped me to adapt to the new environment at MIT.

Table of Contents

Acknowledgement i

Abstract v

List of Publications vii

List of Tables ix

List of Figures x

List of Symbols xv

Chapter 1: Introduction and Literature Review 1

1.1. Thermal Management for Electronic Devices 1

1.2. Vapor Chamber 7

1.2.1. Working Mechanism 7

1.2.2. Performance Limit of Vapor Chamber 9

1.2.3. Studies on Vapor Chambers 11

1.3. Evaporators 21

1.3.1. Introduction to Evaporators 21

1.3.2. Types of Evaporator Wicks 21

1.3.3. Uniform Micropillar Evaporators 23

1.3.4. Biporous Evaporators 29

1.4. Motivations and Objectives of the Thesis 31

1.5. Scope of the Thesis 36

Chapter 2: Analytical Modeling 37

2.1. Uniform Evaporator Modeling 37

2.2. Vapor Chamber with Uniform Evaporator Modeling 43

2.3. Biporous Evaporator Modeling 46

2.4. Summary 49

Chapter 3: Microfabrication 51

3.1. Evaporator 51

3.1.1. Evaporator Design 51

3.1.2. Evaporator Microfabrication 52

3.1.3. Evaporator Samples 56

3.2. Vapor Chamber 59

3.2.1. Vapor Chamber Design 59

3.2.2. Vapor Chamber Microfabrication 60

3.2.3. Vapor Chamber Samples 62
3.3. Summary 64
Chapter 4: Thermal Characterizations 65
4.1. Thermal Characterization of Evaporators 65
4.2. Thermal Characterization of Vapor Chambers 67
4.3. Calibration and Data Interpretation 69
4.4. Uncertainty Analysis 72
4.5. Summary 74
Chapter 5: Performance, Optimization and Parametric Studies 75
5.1. Uniform Evaporator 75
5.1.1. Wettability 75
5.1.2. Liquid Propagation 76
5.1.3. Optimization 77
5.1.4. Parametric Studies 79
5.1.5. Model Validation 84
5.2. Silicon Vapor Chambers 87
5.2.1. Optimization 87
5.2.2. Transient Temperature 88
5.2.3. Parametric Studies 90
5.2.4. Temperature Distribution 93
5.2.5. Performance Comparison 94
5.3. Biporous Evaporators 95
5.3.1. Parametric Studies 95
5.3.2. Uniform vs. Biporous Evaporator 99
5.3.3. Biporous Evaporator Optimization 102
5.4. Summary 104
Chapter 6: Heat Transfer Suppression on Microengineered Surfaces 106
6.1. Background 106
6.2. Experimental Methods 109
6.2.1. Sample Preparation 109
6.2.2. Tests 110
6.3. Droplets Behavior on Various Surfaces 112
6.4. Parametric Studies 116

6.5. Summary 121
Chapter 7: Conclusions and Future Work 122
7.1. Conclusions 122
7.2. Future Recommendations 126
References 128

Abstract

To overcome the high heat generation challenge and ensure sustainable development in the semiconductor industries, thermal management for high density electronic devices has drawn much attention in recent years. Being a passive thermal management device with high heat removal capability, vapor chamber that spreads concentrated heat via liquid-to-vapor phase change phenomena was proven to be a promising cooling technique. The evaporator is the determinant section that governs the performance of a vapor chamber. Silicon vapor chamber with micropillar evaporator possess large thin film evaporation area, mature manufacturing technique and can be integrated with electronic devices homogeneously to eliminate excess thermal interface layer as well as avoid thermal expansion mismatch. However, a comprehensive and systematic study on silicon vapor chamber and micropillar evaporators is lacking. Predictive models that evaluate the performance limits of vapor chamber and evaporators are limited, selection of micropillar geometries is trial-and-error based on previous work. Investigation on wettability performance of micropillar structures was not systematically extended to a high temperature regime. In this thesis, we developed three semi-analytical models in predicting the capillary-limited dryout heat flux of uniform evaporators, biporous evaporators and sealed silicon vapor chambers. We performed optimization to determine the best geometric combinations of the evaporators and vapor chambers by taking the temperature rise into consideration. Accordingly, we fabricated the evaporators and vapor chambers by micro-electro-mechanical-systems (MEMS) process. We defined the micropillar patterns with deep-reactive-ion-etching (DRIE) and measured the temperature with embedded resistance-temperature-detectors (RTDs). We also conducted systematic experiments to determine the dryout heat flux and heat transfer coefficient of samples with various geometries. The models were validated against experiment results with less than 20% over-prediction. A 1 cm × 1 cm uniform and biporous evaporators could dissipate a maximum dryout heat flux of 25.7 and 55.9 W/cm^2, respectively. A thin Si vapor chamber with a thickness of 1.25 mm can handle 98.1 W/cm^2 heat flux before dryout. Heat transfer coefficient was found to increase with larger micropillar diameter/pitch ratio, smaller micropillar height, wider micropillar islands

and narrower microchannel width. Besides the characterization of heat dissipation capabilities, we also examined the droplet behavior on superheated micropillar surfaces. Non-wetting droplets were observed to reside on top of micropillar structures at a temperature much lower than the Leidenfrost point of flat Si. Two peaks on droplet lifetime was observed, the nucleate boiling to non-wetting droplet transition temperature and Leidenfrost point were found to increase with l and h. This thesis provides deep insights, with experimental verification, into the design and optimization of the vapor chamber with micropillar evaporators.

List of Publications

1. **M. Wei**, S. Somasundaram, B. He, Q. Liang, C. S. Tan, and E. N. Wang, "Experimental characterization of Si micropillar based evaporator for advanced vapor chambers," in *Electronics Packaging Technology Conference (EPTC), 2014 IEEE 16th*, 2014, pp. 335 – 340.
2. **M. Wei**, J.W.C. Ho, and Z. Chen, "Effect of Titania Nano-Fillers on the Fracture Toughness and Mechanical Performance of Hybrid Sol-Gel Coatings," Nanoscience and Nanotechnology Letters, vol. 7, pp. 226 – 232, 2015.
3. **M. Wei**, S. Somasundaram, B. He, Q. Liang, R. Raj, C. S. Tan, and E. N. Wang, "Optimization of Biporous Micropillar Array for Enhanced Heat Transfer Performance, " in *International Mechanical Engineering Congress & Exposition(IMECE), 2015 ASME*
4. B. He, **M. Wei**, Q. Liang, C. S. Tan, and E. N. Wang, "Experiments on the Biporous Micropillar Array for Enhanced Heat Transfer Performance," in *5th International Conference on Micro/Nanoscale Heat and Mass Transfer, 2016 ASME*
5. **M. Wei**, B. He, S. Somasundaram, C. S. Tan, and E. N. Wang, "Optimization and Thermal Characterization of Uniform Micropillar Based Silicon Evaporator in Advanced Vapor Chambers," in *The Intersociety Conference on Thermal and Thermomechanical Phenomena in Electronic Systems*, 2016 IEEE
6. B. He, **M. Wei**, S. Somasundaram, C. S. Tan, and E. N. Wang, "Experiments on the Ultrathin Silicon Vapor Chamber for Enhanced Heat Transfer Performance," in *The Intersociety Conference on Thermal and Thermomechanical Phenomena in Electronic Systems*, 2016 IEEE
7. S. Somasundaram, K. Bagnall, S. Adera, B. He, **M. Wei**, C. S. Tan, and E. N. Wang "Detailed Thermal Resistance Model for Characterization of the overall Effective Thermal Conductivity of A Flat Heat Pipe," in *The Intersociety Conference on Thermal and Thermomechanical Phenomena in Electronic Systems*, 2016 IEEE
8. **M. Wei**, B. He, Q. Liang, S. Somasundaram, C. S. Tan, and E. N. Wang, "A Comprehensive Study of Silicon Micropillar Based Biporous Evaporator", in 4th International Conference on Heat Transfer and Fluid Flow (HTFF 17), 2017
9. **M. Wei**, B. He, Q. Liang, S. Somasundaram, C. S. Tan, and E. N. Wang, "Study of Ultra-Thin Advanced Silicon Vapor Chamber: Optimization, Fabrication and Thermal Characterization", in 4th International Conference on Heat Transfer and Fluid Flow (HTFF 17), 2017
10. S. Somasundaram, Y. Zhu, Z. Lu, **M. Wei**, B. He, C.S. Tan and E.N. Wang, "Thermal design optimization of evaporator micropillar wicks", International Journal of Thermal Sciences, *under review*

11. **M. Wei**, B. He, Q. Liang, S. Somasundaram, C. S. Tan, and E. N. Wang, "Modeling, optimization and thermal characterization of uniform silicon micropillar based evaporator", *under review*
12. **M. Wei**, B. He, Q. Liang, S. Somasundaram, C. S. Tan, and E. N. Wang, "Modeling, thermal characterization and optimization of silicon micropillar based biporous evaporator", *in preparation*
13. **M. Wei**, Y. Song, D. J. Preston, S. Adera, Y. Zhu, C. S. Tan, and E. N. Wang, "Heat transfer suppression by suspended droplets on microstructured surfaces", *under review*

List of Tables

Table 1: Summary of vapor chamber literature: list of metal, polymer and silicon vapor chamber geometries, structures and performances 19

Table 2: Summary of literature on permeability K and capillary pressure P_{cap} models in micropillar arrays 26

Table 3: Summary of literature on thermal performance of uniform micropillar wicks 33

Table 4: Summary of literature on thermal performance of biporous evaporator wicks 33

Table 5: Values for the summation series in *Equation (25)* for different *b/a* ratios 44

Table 6: Comparison between simulation and calculated values of f 49

Table 7: List of uniform evaporator geometries. The d, h, and l values were actual geometric sizes measured by SEM 57

Table 8: List of biporous evaporator geometries. The d, h, l, $2i$ and $2w$ values were actual geometric sizes measured by SEM 58

Table 9: List of Si vapor chamber with various micropillar geometries 64

Table 10: Sources and values of uncertainties in thermal characterization 73

Table 11: List of samples with various micropillar geometries for droplet behavior study 109

List of Figures

Figure 1: (a) Microprocessor trend data in the past 40 years. Dotted lines are the extrapolation of Moore's Law (Data collected and plotted by M. Horowitz *et al.* [2]) (b) Heat flux of integrated chips as a function of year [4] 1
Figure 2: (a) Cause of electronic component failure (source from US Air Force Avionics Integrity Program AVIP) [3] (b) Thermal management technology market of various areas in north America [6] 2
Figure 3: Schematic illustration of direct liquid cooling (a) Immersion cooling (b) Jet impingement cooling [8] (c) Spray cooling [8] (d) Microchannel cooling [9] 3
Figure 4: Schematic illustration of cooling techniques (a) Thermoelectric cooling [15] (b) Phase change spreader-heat pipe 6
Figure 5: Schematic illustration of a vapor chamber: a vapor chamber is composed of the evaporator, condenser, and adiabatic regions, which is a closed and evacuated chamber charged with working fluid. It works passively through the evaporation and condensation of working fluid. 7
Figure 6: 6 performance limitations of a vapor chamber 11
Figure 7: Various kinds of evaporator wicks: (a) Wire meshes/screen wick: Wire meshes in a Cu heat pipe [58] and SEM image of woven Cu mesh made of 56 μm wires with 76 μm spacing by Oshman *et al.* [46] (b) Sintered particle wick: heat pipe with exposed sintered Cu particle wick [58] and SEM image of sintered Cu particle wick with particle diameter of 71 μm, scale bar is 100 μm, fabricated by Ju *et al.* [34] (c) Microgroove wick: heat pipe with exposed microgroove wick [58] and design of axial converging microchannel wick by [42] (d) Micropillar wick: hexagonal Cu micropillars [59], square Si micropillars [60] and cylindrical Si micropillars [56].22
Figure 8: Schematic illustration of uniform micropillar based evaporator (a) Top view of the micropillar evaporator: The uniform evaporator is composed of uniformly distributed cylindrical micropillars with diameter d, pitch l, height h and wicking distance L (b) Cross-sectional view: Liquid reservoir, which mimics the condenser/adiabatic regions of vapor chamber, supplies liquid to compensate the liquid loss through evaporation in micropillar arrays. The liquid propagates in micropillar arrays with velocity u due to capillary pumping effect. Uniform heat flux q'' is applied on the back of the evaporator to induce uniform evaporation on the front side. The evaporation is assumed to be uniform with velocity v 37
Figure 9: Schematic illustration of uniform micropillar based evaporator in a vapor chamber (a) Top view: the evaporator has a size of $2a \times 2b$ with micropillar diameter d, pitch l and height h. Fluid flows from the edges of the evaporator to the center and is driven by the meniscus curvature variation from the edge to the center. (b) Cross-sectional view: uniform heat flux q'' is applied from the back of the evaporator. Evaporation occurs at the liquid/vapor interface with uniform velocity v..............43

Figure 10: Schematic illustration of biporous evaporators (a) Top view: the biporous evaporator is composed of micropillar arrays, named as micropillar islands with width $2i$, separated by microchannels with width $2w$. The micropillar islands consist of cylindrical micropillars with diameter d, pitch l and height h. (b) Cross-sectional view of the unit cell in the red box: microchannels serve as local liquid reservoir to shorten the liquid propagation distance. The evaporator is subject to uniform heat flux q'' from the bottom. Evaporation and heat transfer in microchannels are neglected. 46
Figure 11: Photomask design for evaporator samples (a) Chrome mask for 6 inch Si wafers contains several pieces of evaporator samples (b) Closer look of evaporator sample with total size of 1.7 cm × 2 cm and total micropillar area of 1.5 cm × 1 cm , out of which 1 cm × 1 cm is used for evaporation (c) Design of heater and 4 resistance-temperature-detectors (RTDs) (d) The heater has a zig-zag pattern of 590 μm wires spans over an area of 1 cm × 1 cm (e) RTD has 25 μm zig-zag wires span over an area of 2.24 mm × 0.525 mm 52
Figure 12: Fabrication process of evaporator sample front side with evaporator wicks 53
Figure 13: (a) SEM images of cylindrical micropillars with diameter d, height h, and pitch l. The micropillars have scallop sidewalls. (b) Images of front side and backside of uniform evaporator sample (c) Illustration of macroscopic meniscus 56
Figure 14: (a) Picture and SEM images of biporous evaporators with micropillar arrays separated by microchannels (b) Backside heater and RTDs of biporous evaporator sample 58
Figure 15: Mask designs for sealed Si vapor chambers (a) Backside of top wafer with cavity and supporting posts (b) Front side of top wafer with 1/8'' and 1/16'' holes (c) Front side of bottom wafer with micropillar structures (d) Back side of bottom wafer with RTDs and heater. 59
Figure 16: Steps of microfabrication process for sealed Si vapor chambers 61
Figure 17: Images of Si vapor chambers (a) Backside of top wafer with 3 cm × 3 cm cavity (b) Front side of top wafer with 1/8'' and 1/16'' holes (c) Backside of bottom wafer with heater and RTDs (d) Front side of bottom wafer with micropillar structures and SEM image of micropillars (e) Sealed Si vapor chamber with thin thickness and 2 tubes. 63
Figure 18: Schematic illustration of the experimental setup for uniform/biporous evaporators: The evaporator sample was mounted on a PCB with pogo pins to connect to power supply and data acquisition system. Thermal characterization was conducted inside vacuum chamber under vacuum condition. Working fluid used in the characterization was degassed in degassing tank. Evaporator dryout was monitored by high speed camera. 65

Figure 19:(a) Schematic illustration of the experimental setup for vapor chamber characterization: The vapor was mounted onto a PCB and evacuated by the turbo pump. Degassed DI water was filled into the vapor chamber to serve as working fluid. A copper cooler was used to cool the condenser side of the vapor chamber. Power was applied to the vapor chamber while resistance readings of RTDs were measured by DAQ. (b) The design of PCB: 8 contact pads corresponded to 3 RTDs and 1 heater, which were connected to an RS232 9 pin connector (c) Layout of vapor chamber mounted on PCB with 7 thermocouples to measure condenser temperature...........68
Figure 20: Temperature versus resistance readings of RTDs obtained by calibration inside an oven against a high precision Pt 100 RTD. Good linearity can be observed with $R^2 \approx 1$ 70
Figure 21: Heat dissipation not via evaporation in micropillar wicks, which includes evaporation from the macroscopic meniscus, convection, conduction and radiative heat transfer. And 1D conduction assumption of heat from the sensor to the micropillar bottom 72
Figure 22: High-speed camera image of (a) Water droplet on the plain silicon surface. The plain silicon surface is hydrophilic (b) Liquid spreading on uniform micropillar structured surface with superhydrophilic liquid spreading.....................................75
Figure 23: High-speed camera image of liquid climbing in a vertically aligned uniform micropillar evaporator at different time. Liquid front is indicated by the dotted lines. 76
Figure 24: Liquid propagation distance as a function of time 77
Figure 25:(a) Optimized geometric combinations with superheat range of 1 – 15 ℃ (b) The corresponding dryout heat flux at different superheat. 78
Figure 26: Effect of *d/l* ratio on uniform micropillar evaporators performance (a) Heat flux vs. superheat curve and (b) Heat transfer coefficient vs. heat flux curve for evaporator samples with constant h =39.5 μm, l = 41.0 μm while d changed from 28.2 to 25.9, 23.4 and 22.1 μm; (c) Heat flux vs. superheat curve and (d) Heat transfer coefficient vs. heat flux curve for evaporator samples with constant h = 39.5 μm, d = 23.4 μm while l varied from 34.0 to 36.0, 41.0 and 44.0 μm. 80
Figure 27: (a) Regions of liquid meniscus around a micropillar: intrinsic meniscus region governed by surface tension and non-evaporating region governed by intermolecular force, where evaporation was suppressed. The transition region accounted for more than 80% total heat transfer (b) Micropillars with same d, different l (c) Micropillars with same l, different d 81
Figure 28:Liquid meniscus at various heat flux levels (a) Low to moderate heat flux (b) Higher heat flux prior to the inception of dryout (c) High heat flux after dryout. The liquid meniscus receded as heat flux increased, curvature and more evaporation areas before dryout (a – b). After dryout (c), evaporation areas decreased as there was no liquid in between of some micropillars 82

Figure 29:Effect of *h* on uniform micropillar evaporators performance (a) Heat flux vs. superheat curve (b) Heat transfer coefficient vs. heat flux curve for evaporator samples with *h* changed from 39.5 to 79.7 and 84.5 µm. 83
Figure 30: (a) Dryout heat flux for different uniform samples – model prediction vs. experimental measured values. Model overestimated the dryout heat flux within a difference of less than 20%. (b) Dryout superheat for various uniform evaporators, difference between model predicted and experimental measured dryout heat flux was within 2 K. 85
Figure 31: Optimization results of silicon vapor chamber evaporators for a superheat range of 1 ˚C to 20 ˚C (a) Optimized evaporator geometries *d*, *h*, and *l* (b) Corresponding dryout heat flux at various dryout superheats 88
Figure 32: Heat flux and RTD temperature of vapor chamber *sample H* as a function of time 89
Figure 33: Parametric studies (a) Heat flux *q''* versus temperature difference between evaporator and condenser curve for silicon vapor chamber *A* to *G* (b) Effective thermal resistance versus heat flux curve. Out of which *sample G* is a reference sample without liquid charging...90
Figure 34: Condenser side temperature distribution of (a) *sample A* (b) *sample D*93
Figure 35: Performance comparison between our silicon vapor chambers and the most up-to-date silicon vapor chamber fabricated by Cai *et al.* [56].......................94
Figure 36:Parametric studies of biporous evaporators with various micropillar island width 2*i* and microchannel width 2*w*. (a) Heat flux versus superheat curve and (b) Heat transfer coefficient versus heat flux curve of *sample 1 – 4* with constant *d* = 3.4 µm, *h* =8.9 µm, *l* = 6 µm, 2*w* = 117 µm and various 2*i* ranged from 120, 202, 240 to 280 µm. (c) Heat flux versus superheat curve and (d) Heat transfer coefficient versus heat flux curve of sample 2, 5 – 7 with constant *d* = 3.4 µm, *h* =8.9 µm, *l* = 6 µm, 2*i* = 202 µm and various 2*w* ranged from 60, 90, 117 to 150 µm. 96
Figure 37:Dryout heat flux of uniform evaporators (black square dots) and biporous evaporators (red round dots): experiment measured vs. model predicted dryout heat flux 99
Figure 38:High speed camera images of dryout on evaporator samples (a) 1s and 100s after dryout of biporous evaporator sample (b) 1s and 17.4s after the onset of dryout on uniform evaporator sample..101
Figure 39:(a) Geometric optimization results (micropillar height *h*, half micropillar island width *i* and half microchannel width *w*) of biporous evaporator for an allowable superheat range of 5 – 30℃ (b) Dryout heat flux comparison between biporous and uniform evaporators with superheat range of 5 – 30 ℃...................103
Figure 40: SEM images for the droplet behavior test samples with various micropillar geometries (a) *Sample D* and (b) *Sample C* with the same *d* and *h*, while

l varies from 50 to 30 µm (c) *Sample E* (d) *Sample F* and (e) *Sample G* with the same *d* and *h*, while *l* varies from 80, 110 to 120 µm..110
Figure 41: Schematic illustration of experimental setup for droplet lifetime measurement (not to scale): The micropillar structured surfaces were heated by a hot plate with a thick copper block. Droplets with constant volume of 10 µl were dispensed by micropipette on the superheated micropillar surface with stable temperature. Droplet lifetime was captured by high speed camera, while the surface temperature was measured by three K type thermocouples..................................111
Figure 42: 3 stages for water droplets encountered a superheated plain silicon surface: *stage 1* – vigorous boiling stage with droplet lifetime decrease with temperature, the high-speed camera image was captured at 225 ˚C; *stage 2* – transition stage between nucleate boiling and Leidenfrost state, image was taken at 255 ˚C; *stage 3* – Leidenfrost state with droplet suspended by a vapor layer, image was obtained at 300 ˚C..113
Figure 43: 5 stages when water droplets encountered a superheated microengineered Si surface with micropillar structures. The sample presented was *sample B*. *Stage 1*: vigorous boiling, pictures captured at 143.7 ˚C; *Stage 2*: first transition regime between boiling and non-wetting stage, image took at 179.7 ˚C; *Stage 3*: non-wetting stage, droplet did not wet the superhydrophilic surface, instead it rested on top of the microengineered surface and was in contact with the micropillar tops, picture obtained at 219.7 ˚C; *Stage 4*: second transition regime between non-wetting and Leidenfrost state, droplet was in contact with micropillars at first, and then levitated by a vapor layer to suspend above the surface when it became smaller due to evaporation at 282.3 ˚C; *Stage 5*: Leidenfrost state with suspended droplet supported by a vapor layer at 356.6 ˚C...115
Figure 44: Lifetime of droplets at different temperature for microengineered surfaces with various geometries and flat Si surface (*sample A*). (a) Effect of *l*: *sample B – D* have *h* = 21.4 µm, *d* = 6 µm and *l* ranges from 20 to 50 µm (b) Effect of *l*: *sample E – G* with *h* = 38.3 µm, *d* = 36.4 µm and *l* ranges from 80 to 120 µm (c) Effect of *h*: *sample B* and *sample G – I* with the same solid fraction of 0.07 and various *h* of 21.3, 27.4, 38.3 and 74.9 µm. The transition temperature from boiling to non-wetting regime and the Leidenfrost point were indicated by the arrows. Both transition temperature and Leidenfrost point were found to increase with higher *l* and larger *h*. 118

List of Symbols

Symbol	Description
A	area, m^2
D	uncertainty, %
I	current, A
K	permeability, m^2
L	wicking length, cm
P	pressure, Pa
R	resistance, Ω
S	calculated parameter
T	temperature, $^\circ C$
U	voltage, V
V	volume, m^3
a	the slope of the resistance-temperature relationship
b	the intercept of resistance-temperature relationship
c	solid fraction
d	micropillar diameter, μm
h	micropillar height, μm
i	half island width, μm
k	thermal conductivity, $W/m\cdot K$
l	micropillar pitch (center-to-center distance), μm
m	measured parameter
q	heat flux, W/cm^2
t	thickness, μm
u	flow velocity, m/s
w	half microchannel width, μm
h_c	heat transfer coefficient, $W/cm^2\cdot K$
rf	roughness factor, $\pi/2$
x	Cartesian coordinates, x direction
y	y direction
z	z direction

Subscripts

Subscript	Description
app	applied
c	coefficient
cap	capillary
eff	effective
fg	latent heat
l	liquid
$loss$	heat loss
la	drop in the microchannel
m	actual meniscus
n	n^{th}
p	projected meniscus
$pillar$	micropillar
sat	saturation
$sensor$	Pt RTD sensors
Si	silicon
SiO_2	silicon dioxide
$vapor$	water vapor
$wafer$	silicon wafer
$2D$	planar

Greek symbols

Symbol	Description
Δ	difference
ε	porosity
θ	contact angle, $^\circ$
v	evaporation rate, m/s
μ	viscosity, $Pa\cdot s$
π	pi constant,
ρ	density, kg/m^3
σ	surface tension of the liquid, N/m

Chapter 1: Introduction and Literature Review

1.1. Thermal Management for Electronic Devices

According to the famous Moore's law established in the year of 1964, the number of transistors per integrated circuit was predicted to double almost every two years [1]. This self-fulfilling prophecy has proven to be accurate and became the leading principle in guiding the semiconductor industry's future. Driven by the rapid development of semiconductor industries, the miniaturization of electronic component size, increasing density integration of chips and enhancement in device functionality were inevitable trends. As shown in *Figure 1*, the microprocessor power [2] increased rapidly as transistor number increased in the past few decades. As a result, the heat flux per high performance chip also increased significantly as a function of time [3, 4].

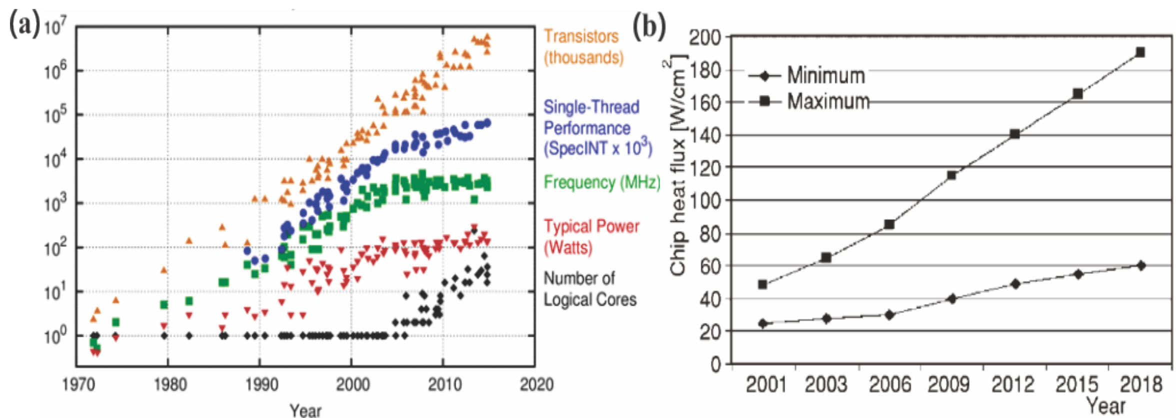

Figure 1: (a) Microprocessor trend data in the past 40 years. Dotted lines are the extrapolation of Moore's Law (Data collected and plotted by M. Horowitz et al. [2]) (b) Heat flux of integrated chips as a function of year [4]

The high temperature associated with a high heat flux of integrated chips may cause the thermal expansion mismatch, thermal fracture, excessive thermal mechanical stress and thermal de-bonding that lead to the failure of electronic devices. As shown in *Figure 2 (a)*, 55% of failures in electronics were caused by thermal issues and the lifetime of electronic devices was found to decrease almost exponentially with temperature [5]. Therefore, thermal issues became the critical threshold in the development of advanced electronics. Concentrated high heat flux need to be dissipated effectively in order to

maintain the electronic devices to work within the reasonable temperature range. Thermal management market grew very fast in the past years as shown in *Figure 2(b)* and thermal management techniques were widely studied.

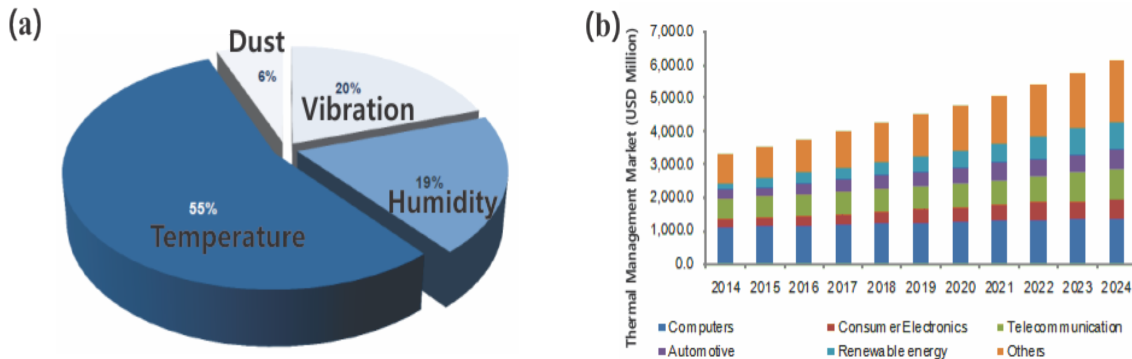

Figure 2: (a) Cause of electronic component failure (source from US Air Force Avionics Integrity Program AVIP) [3] (b) Thermal management technology market of various areas in north America [6]

Thermal management techniques for electronic devices can be classified into 5 categorizes, namely air cooling, liquid cooling, thermal electric cooling, phase change materials cooling, and phase change spreaders.

Air cooling

Air cooling is a heat dissipation method that removes heat by convection/ radiation. When the power of electronic devices is lower than 5 W, it can be cooled via natural convection and radiation by providing sufficient ventilation. In the case where natural convection is not effective enough for higher heat flux dissipation, forced convection was adopted through the installation of fans, pumps or utilization of air jets. Natural convection and forced convection air cooling can be further enhanced by extending the heat transfer area with heat sinks. Air cooling is a simple, reliable cooling technique with low cost. However, the maximum heat flux it can dissipate is only around 1.6 W/cm^2 [7], which was inadequate for high density electronic devices. Beyond the low efficiency of air cooling, thermal interface materials are usually required for the installation of heat sinks and external pumps. This introduces excess thermal resistance.

Liquid Cooling

Due to the high heat transfer coefficients of liquid than air, liquid cooling is a more effective cooling technique for high power electronic devices. It can be divided into immersion liquid cooling, jet impingement cooling, spray cooling and microchannel cooling. Heat transfer modes in liquid cooling can be natural convection, forced convection or boiling depends on the actual working condition and liquid properties.

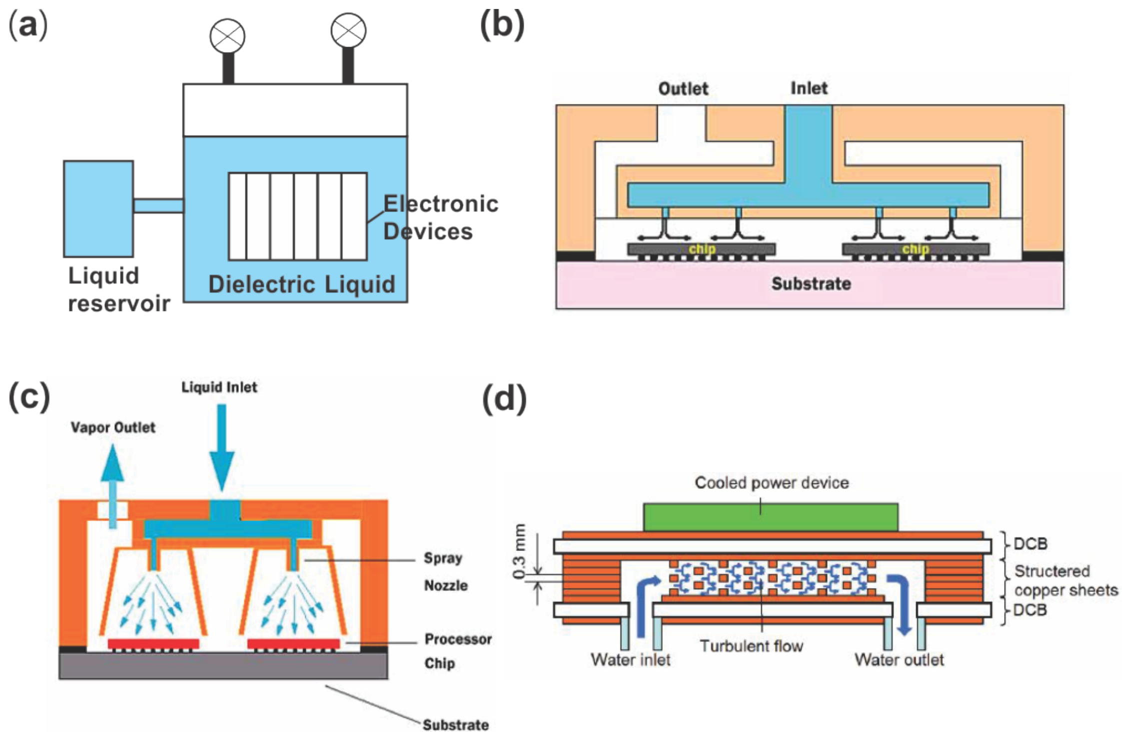

Figure 3: Schematic illustration of direct liquid cooling (a) Immersion cooling (b) Jet impingement cooling [8] (c) Spray cooling [8] (d) Microchannel cooling [9]

Immersion Cooling

Immersion cooling refers to a cooling technique of submerging the electronic devices in thermally conductive but electrically insulating liquid to achieve heat dissipation through pool boiling. Schematic illustration of immersion cooling is shown in *Figure 3(a)*. Commonly used dielectric liquid for immersion cooling are *Fluorient*^{TM} and *Novec*^{TM} developed by *3M*. It is an energy saving cooling technique with relatively high efficiency compared to air cooling. Immersion cooling also possesses the advantage of

accommodating electronic devices with any size, shape, and forms. However, corrosion may be caused by prolonged exposure of electronic devices to the coolant and leakage protection needs to be carefully secured.

Jet Impingement Cooling

Figure 3 (b) illustrates the schematic of jet impingement cooling. Jet impingement cooling works by directing a high velocity liquid jet onto a high temperature hotspot. Cooling is achieved through single or two-phase heat transfer with large heat transfer coefficient on the local impingement spot. According to Wang *et al.* [10], a heat flux of 90 W/cm^2 can be dissipated with a temperature rise of 100 °C by four 76 μm diameter jets at a flowrate of 8 ml/min [10]. Flowrate and flow regimes can be optimized for effective heat transfer. Heat dissipation capabilities of jet impingement cooling depend on a vast number of parameters, such as jet velocity, jet size, and distance from orifice to hotspots, orifice shapes, liquid thermophysical properties *etc.* It is an active cooling technique that requires external pumps and is relatively complicated to implement.

Spray Cooling

Spray cooling is a similar cooling method to jet impingement cooling, where liquid droplets are impinged on the hot electronic devices, as shown in *Figure 3 (c)*. A thin liquid was formed on the hot surface and a large amount of heat was dissipated through evaporation. Lin *et al.* [11] constructed a spray cooling setup. Like the case in jet impingement cooling, fluid for spray cooling is dielectric liquids that are electrically insulating. Promising candidatures include Fluorinert^{TM} liquids, methyl silaxones, refrigerant R134a *etc.* [3]. Protective layers need to be deposited on electronic devices to prevent a short circuit if water is used as the fluid. Heat flux of 90 W/cm^2, 490 W/cm^2 and > 500 W/cm^2 can be removed with FC-87/FC-82, methanol and water, respectively. Non-uniform heat dissipation of 270 W/cm^2 was demonstrated by thermal inkjet spray cooling technology [12]. In comparison to jet impingement cooling, spray cooling requires lower fluid flow rates, promotes better temperature uniformity. However, extremely high pressure drop (several hundreds of kPa) at the nozzle is required for both

spray and jet impingement cooling. For instance, 7 W power consumption and 300 kPa was needed to realize a cooling of around 180 W/cm^2 in [10].

Microchannel Cooling

Microchannel cooling works by forcing a flow with pumps through a small hydraulic diameter channel, as shown in *Figure 3 (d)*. High heat flux removal can be achieved due to flow boiling inside microchannels. With external pumping power of 1 W, the heat flux of 230 W/cm^2 to 350 W/cm^2 can be removed with microchannel cooling techniques demonstrated by Gillot *et al.* [13]. To promote flow stability and facilitate bubble removal, micropillars with a diameter of 5 – 10 μm, pitch 10 – 20 μm and height 25 μm was introduced to silicon microchannels with 500 μm × 500 μm by Chu *et al.*. A high heat removal capability of 614 W/cm^2 can be achieved [14]. Microchannel cooling is a promising thermal management technology in terms of its high heat transfer coefficient, low thermal resistance and medium pressure drop of several dozens kPa. However, formation and expansion of vapor bubbles during the boiling process may cause large temperature non-uniformity, result in local dryout and lead to back flow of liquid. Large flow instabilities in microchannel cooling make the system complicated and it is very hard to have a reliable prediction on the heat dissipation performance by microchannel cooling.

Thermoelectric Cooling

Thermoelectric cooling utilizes Peltier effect, where electricity was converted to thermal energy for cooling. As shown in *Figure 4 (a)*, when a p-n junction is subjected to a current from the right direction, electron and hole pairs will be generated. Electrons and holes flow away from the junction in n type and p type materials, respectively, which consumes energy and results in the cooling effect of the junction [15]. Capabilities of traditional air and liquid cooling devices were proven to be enhanced by integrating thermoelectric cooling with the devices at low heat loads [16, 17]. Thermoelectric cooling offers a simple, flexible, quiet, leakage-free and reliable cooling method for electronic devices. However, it also results in excess power consumption of 50 – 60 W and is suitable for small capacity heat removal of 5 – 10 W/cm^2 only.

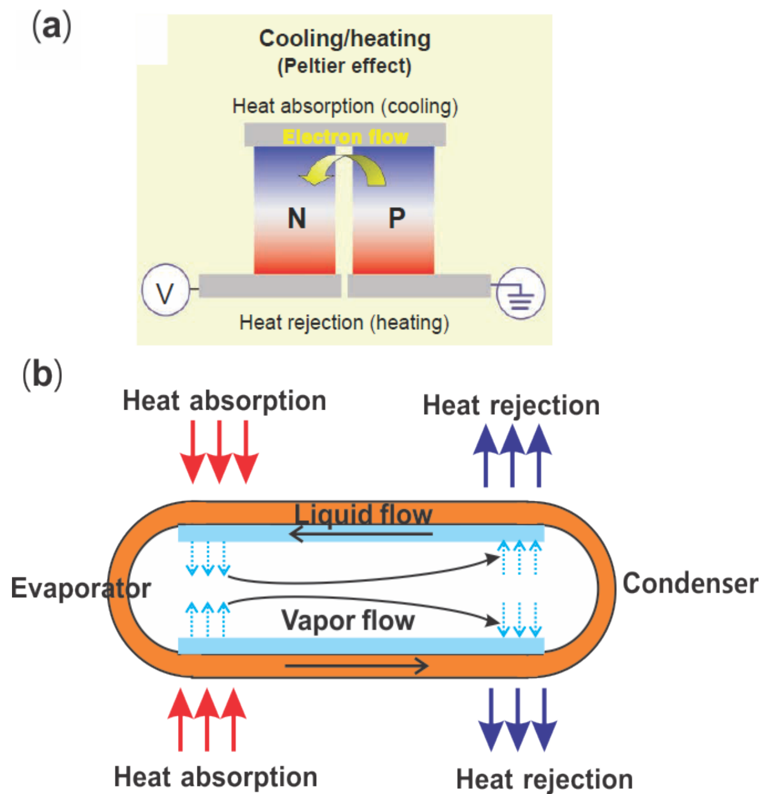

Figure 4: Schematic illustration of cooling techniques (a) Thermoelectric cooling [15] (b) Phase change spreader-heat pipe

Phase Change Materials

Phase change materials, which has the high latent heat of melting, are also used for portable device cooling. It can store and release energy based on different phase change processes. According to Tan *et al.* [18], the temperature of wearable electronic devices can be maintained below 50° C for 2 hrs with n-eicosane phase change material. Performance of phase change materials filled heat sinks was found to increase with heat input as the phase change material melt rate increases [19]. Phase change materials can be divided into organic, inorganic, eutectic, hygroscopic and solid/solid phase change materials. Phase change material cooling is a simple, light weight and space saving technique for transient electronic cooling. Possible problems of material compatibility, leakage, high thermal resistance and environmental hazards need to be addressed to use phase change materials for thermal management.

Phase Change Spreaders

Liquid/vapor phase change mechanism is utilized in phase change spreaders such as heat pipes, thermosyphons, and vapor chambers. Schematic illustration of a heat pipe phase change spreader is shown in *Figure 4 (b)*. Heat is absorbed to cause liquid evaporation in evaporator, while the vapor is condensed into liquid and heat is rejected at the condenser. Owing to the high latent heat involved in the phase change process, phase change spreaders can dissipate a large amount of heat with low temperature rise and good temperature uniformity. A porous evaporator wick can circulate the fluid inside the spreader automatically. Therefore, the phase change spreader is a passive cooling device. Unlike active cooling techniques that require additional bulky and costly pumping systems, for example, jet impingement cooling, forced convection with fans, spray cooling and thermoelectric cooling, the passive cooling technique with phase change spreaders offers a compact, light-weight and high-performance solution for electronic cooling. Therefore, developing high performance phase change spreaders has been an emerging hot topic in thermal management areas.

1.2. Vapor Chamber

1.2.1. Working Mechanism

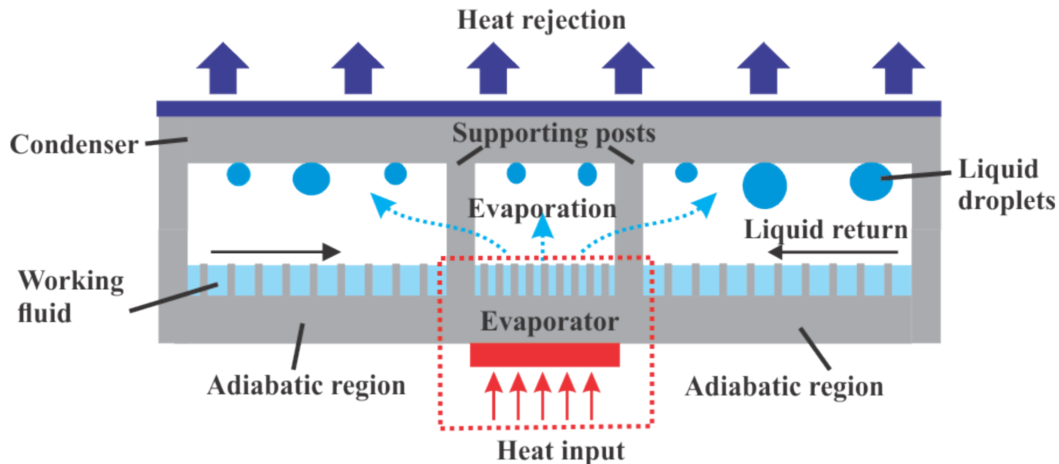

Figure 5: Schematic illustration of a vapor chamber: a vapor chamber is composed of the evaporator, condenser, and adiabatic regions, which is a closed and evacuated chamber charged with working fluid. It works passively through the evaporation and condensation of working fluid.

Heat pipes and vapor chambers are commonly used phase change spreaders for electronic cooling. Shapes of heat pipes are often cylindrical with circular cross-sectional areas, while vapor chambers are 2D flat heat pipes with rectangular cross-sectional areas. Typical schematic of a vapor chamber is illustrated in *Figure 5*. A vapor chamber is a sealed vessel that is evacuated and charged with working fluid. It can be divided into 3 sections, evaporator, condenser and adiabatic regions. During operation, heat inputs from the hotspots located at the evaporator. This causes the evaporation of the working fluid into vapor and results in higher local vapor pressure. A pressure gradient is induced between the evaporator and condenser, which drives the vapor to flow to the condenser. After that, the vapor is condensed back into liquid as the condenser possess lower temperature. Then the liquid is transported back to the evaporator by the capillary action of porous adiabatic and evaporator regions. The continuous and passive operation of vapor chamber is achieved through repeat cycles of aforementioned processes. Due to the high latent heat phase change processes, vapor chambers can remove a large amount of heat and work isothermally. It can operate against gravity and demonstrate large effective thermal conductivity compares to solid heat spreading materials. In summary, the vapor chamber is a reliable, light weight and hermetic cooling device. In comparison with a heat pipe in *Figure 4 (b)*, which transports heat to a remote location with a circular cross-sectional area, a vapor chamber has a flat shape and reduced liquid transportation distance. So the vapor chamber can fit with the thin-plate-shape electronic components to reduce contact resistance and is capable of dissipating higher heat flux with lower thermal resistance. This makes it suitable for compact and light weight electronic devices at nowadays. Thus, there is an increasing demand for thin, high performance vapor chambers.

The vessel/chamber serves the purpose of isolating the working fluid from outside ambient. Thus the selection of chamber material should be able to satisfy the following requirements [20]. First of all, it needs to be leak proof with desired mechanical strength, since the vapor chamber works under vacuum condition and the chamber material should be able to sustain the internal operating pressure and external atmospheric pressure. Secondly, the material should be easy to fabricate and compatible with enclosed working

fluid. Superior strength to weight ratio and high effective thermal conductivity are also preferred to produce light weight and high-performance vapor chamber. Promising candidates for the chamber materials include copper, aluminum, polymer, glass, ceramics, silicon *etc.*.

The wick structures in the evaporator regions serve the function of developing a capillary force to transport liquid for continuous operation of a vapor chamber. A superior evaporator should be able to provide large capillary pressure for liquid transportation and high permeability for low flow resistance. It is usually the pivotal and performance determinant part of a vapor chamber [21], stem from its highest thermal resistance and temperature drop among various sections of a vapor chamber [22].

A vapor chamber dissipates heat via the phase change processes of the working fluid. An important parameter in the selection of proper working fluid of a vapor chamber is denoted as $Me = \rho_l \sigma h_{fg} / \mu$, which is known as figure of merit of the working fluid [23]. ρ_l, σ, h_{fg} and μ are working fluid density, surface tension, latent heat of vaporization and viscosity, respectively. Working fluid with higher *Me* is preferred, which corresponds to a fluid with higher density, surface tension, latent heat and low viscosity. Water is a commonly used working fluid with high figure of merit. Despite a high figure of merit, selection of working fluid should consider of the thermal stability, material compatibility and operating temperature range of a vapor chamber as well [24]. The performance of vapor chamber was found to be enhanced by incorporating nanoparticles into the working fluid to reduce the thermal resistance [25]. Working fluids for normal electronic cooling include water, methanol, and acetone *etc.*.

1.2.2. Performance Limit of Vapor Chamber

The heat dissipation capability of a vapor chamber is determined by 6 limitations that can be classified into 2 main types: limitations that lead to vapor chamber failure and non-failure limitations [20]. Failure of a heat pipe is reached when the liquid supply to the evaporator at a certain heat flux cannot sustain the liquid amount evaporates, which leads to the dryout of the evaporator and a dramatic increase of vapor chamber thermal resistance [23]. Detail of vapor chamber performance limitations are described below.

Limitations lead to failure

Capillary limit

The capillary limitation is the most commonly encountered and primary performance limitation of a vapor chamber. It occurs when the capillary pressure developed in the wick structures is not large enough to overcome the pressure drop at high heat loads. This limitation can be extended with well-designed wick structures that possess high capillary force and high permeability.

Boiling limit

Boiling limit is reached when the applied heat flux is large enough to initiate nucleate boiling, which results in drastic vapor bubble generation. The vapor bubbles act as vapor blankets to hinder further phase change and liquid return, which ultimately cause dryout of the vapor chambers. An effective wick structure with excellent vapor escaping and liquid transportation design can be adopted to avoid boiling limit at low heat fluxes.

Entrainment limit

Entrainment limit is triggered when the liquid return to the evaporator is constrained by the high velocity vapor. This reduces the amount of liquid return to the evaporator and causes dryout. Entrainment limit can be avoided by operating the vapor chamber at high temperature or having a larger vapor core size.

Non-failure limitations

Viscous limit/Vapor pressure limit

At low operation temperature where the saturation pressure of the vapor is close to the pressure difference between the evaporator and condenser, the pressure to drive the vapor is not sufficient for vapor to flow to the condenser. In this case, the viscous limit is reached. This can be avoided at high operating temperatures or changing the working fluid for the vapor chambers.

Sonic limit

At the initial stage of vapor chamber operation, the sonic limit may be encountered when the flow is choked by high vapor velocity.

Condenser limit

Condenser limit is triggered when the condenser side of the vapor chamber cannot be cooled effectively by natural convection or heat sinks.

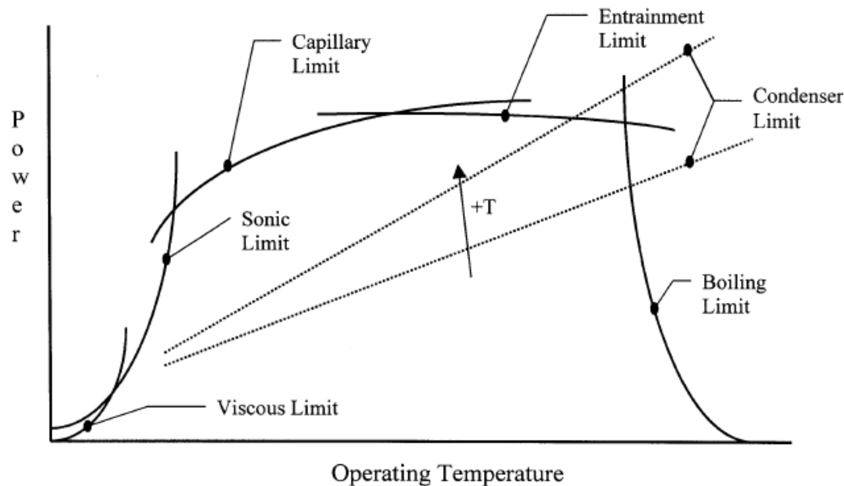

Figure 6:6 performance limitations of a vapor chamber

Collectively, the 6 limitations govern the performance capability of a vapor chamber as shown in *Figure 6*. As discussed above, vapor chamber needs to be well designed to avoid these limitations within its operating heat load range. Evaporator wick design also plays a significant role in increasing the capillary and boiling limit of a vapor chamber. Thus, the evaporator is the most pivotal part of the vapor chamber.

1.2.3. Studies on Vapor Chambers

Recently, the vapor chamber became more and more popular in electronics thermal management and was widely investigated. Researchers constructed various models [26 – 29] in predicting the thermal performance of vapor chambers. Vapor chambers made of different materials, various evaporator wicks were fabricated and tested with different working fluids, charging ratios *etc.*. Prasher [27] modeled the total thermal resistance, thermal resistance limited maximum heat load transport capability and capillary limited heat load of circular vapor chambers based on conduction. It was found that both the heat load transport capability and heat load carrying capability of the vapor chamber decrease with the thickness of the vapor chamber. The model was validated against experiments with active and remote cooling modes and good agreement was

demonstrated. Transient response of evaporator, condenser and adiabatic region temperatures were predicted by Chen *et al.* [26]. Transient temperature as a function of time was measured for a copper vapor chamber with 76 mm × 60 mm × 6 mm size, 30 mm × 30 mm heater and 0.14 mm sintered powder wick to verify the model prediction. An overestimation less than 1.8 K for the temperature rise < 20 K was an indication of high accuracy for their model. Wang *et al.* [28] provided a simple solution to accurately calculate the effective thermal conductivity of the vapor chamber. The heat source and vapor chamber size were found to affect the effective thermal conductivity significantly. Vapor chamber was proven to have effective thermal conductivity several times higher than that of solid metal. Ranjan *et al.* [29] developed a model to estimate the heat transfer performance of ultra-thin vapor chambers. Model validation and vapor space/ wick thickness optimization were conducted. For an ultra-thin vapor chamber (1 mm thickness) with vapor space size of 0.2 – 0.4 mm, the thermal resistance of vapor space was found to be very large due to the large pressure and temperature drop in the vapor space. A vapor chamber with larger vapor space thickness and higher condenser side temperature is recommended for the use of ultra-thin vapor chamber in heat dissipation.

Metal Vapor Chambers

Metals with high thermal conductivity, strong mechanical strength, and mature manufacturing processes were often used as the casing materials for conventional vapor chambers [30 – 45]. Commonly used metals for vapor chambers are stainless-steel, Cu, Al, Ti and alloys (*e.g.* CuMoCu). Among various metals, Cu is the most widely used material for a vapor chamber. This is due to its high thermal conductivity and low cost. Al is also popular as it has high flexibility, low cost, and light weight. Go *et al.* [33] fabricated Al vapor chamber with double-side spray etched stainless steel wicks. The wick was composed of concentrically converging liquid channels with 150 μm width. The vapor chamber could handle heat flux of 80 W/cm^2 at a temperature of 85℃. Al vapor chambers with sintered Al powder and radial artery wicks were fabricated by Chen *et al.* [42]. The prototypes had a size of 58 mm× 58 mm× 6 mm. Lowest thermal resistance of 0.72 K/W and 0.69 K/W can be obtained for vapor chambers with sintered

powder wick and groove wick, respectively. The low thermal resistance of sintered powder wick was explained by its high capillary performance. Chen *et al.* [39] studied the spreading thermal resistance of solid metal plate and vapor chamber. Thermal resistance of vapor chamber was found to decrease with increase heat load, which was due to the high latent heat in phase change process. In contrary, thermal resistance of solid plate was not a function of heat load. Vapor chamber demonstrated better temperature uniformity and low temperature rise compared to solid metal spreader. Chang *et al.* [43] studied the influence of non-uniform heating on the thermal resistance of vapor chambers. The effect of non-uniform heating on vapor chamber thermal resistance was not profound according to their model and tests on Cu vapor chambers. Hsieh *et al.* [31] fabricated a wickless Cu vapor chamber with size of 300 mm × 300 mm×100 mm that relied on gravity for liquid return. Evaporator was proven to have the highest thermal resistance among different sections of a vapor chamber. A maximum heat flux of 220 W/cm^2 can be removed with a total effective chamber resistance of 0.5 K/W and spreading resistance of 0.2 K/W. Wong *et al.* [36] studied the performance of a novel Cu vapor chamber with sintered Cu wicks. Their vapor chamber had dimensions of 100 mm × 89 mm with 2 mm/1.6 mm triangular grooves on the condenser side, which served as vapor pathway and liquid flow path. The evaporator and condenser resistance were proven to increase with heat loads, and the evaporator resistance played a dominant part of the vapor chamber total resistance. Lowest vapor chamber resistance of 0.042 K/W was obtained at 350 W heat load. Ji *et al.* [44] fabricated and investigated the performance of circular Cu vapor chamber with different working fluids (water, acetone, ethanol) and inclination angles (0˚, 60˚, 90˚). Their vapor chamber had Cu foam wicks on the evaporator and condenser. The vapor chamber was found to possess best temperature uniformity at 60˚ tilted angle at low heat load < 75 W while it performed best at 0˚ inclination for heat load > 75 W. Water was the optimal working fluid which can demonstrate 216 W/cm^2 heat removal capability at a thermal resistance of 0.09 K/W. Later on, Ji *et al.* [30] tested their circular vapor chamber with extended condenser. The condenser was composed of circular grooves and fins with capillary holes on them. With a diameter of 95 mm, the circular vapor chamber can dissipate a large heat flux of up to

450 W/cm^2 without dryout. Napthon *et al.* [35] compared the thermal performance of vapor chamber with conventional cooling methods on an actual CPU. They concluded that vapor chamber can result in 6.89% reduction of CPU temperature with 10.53% lower power consumption compared to that of conventional solid material cooling. Tang *et al.* [37] presented a Cu vapor chamber that had multi-artery to act as liquid pathway. The condenser and evaporator of their 90 mm × 90 mm× 3 mm vapor chamber was covered by sintered Cu wicks. The vapor chamber could dissipate heat flux more than 300 W/cm^2 with low thermal resistance of 0.08 K·cm^2/W.

A group of researchers from University of California Santa Barbara fabricated and tested the performance of all-Ti vapor chambers [38, 41]. The high fracture toughness, light weight, water compatible and compliant properties of Ti made it a promising material for compact and ultra-thin vapor chambers. Ding *et al.* [41] developed a 30 mm × 30 mm × 0.6 mm Ti vapor chamber with multi-scale evaporator wick. The wick was microfabricated Ti micropillars with 5 μm diameter, 10 μm pitch and 50 μm height. To further enhance the wettability of Ti micropillar wick, a layer of 200 nm nanowires was created on the micropillars by oxidizing the wick with hot hydrogen peroxide. The nanowires increased liquid propagation velocity in micropillar arrays by 161%. An effective thermal conductivity of 350 W/m·K at 7.2 W was demonstrated by the Ti vapor chamber. A large (300 mm × 76 mm × 45 mm) but yet light (500 g) Ti vapor chamber was fabricated later by Sigurdson *et al.* [38]. The evaporator of this large Ti vapor chamber was Ti nanowires coated microgrooves with 250 μm depth and 350 μm width. The geometries of microgrooves were determined based on theoretical optimizations. A highest effective thermal conductivity 0f 8000 W/m·K was demonstrated by this vapor chamber. The vapor chamber was proven to handle 500 W and 1000 W heat load at 100℃ and 150℃, respectively.

Researchers also extensively studied metal vapor chambers with innovative evaporator wick or condenser designs [32, 34, 40, 45]. Multiscale wicks with 30 – 100 μm micro-size pores and 200 – 800 nm nanopores were chemically deposited on the condenser and evaporator sections of Cu vapor chamber fabricated by Sun *et al.* [45]. The adoption of the multiscale wick was found to reduce the vapor chamber thermal resistance by 18%,

owing to the high capillary force developed by small scale nanopores. Ju *et al.* [34] systematically studied the performance of 3 kinds of evaporator wicks, i.e. wick with vertical arteries, biporous sintered Cu, and converging liquid arteries. The hybrid wicks were proven to possess high heat flux limit and low thermal resistance attributed to the presence of high permeability liquid arteries and large evaporation areas. A 100 mm× 100 mm vapor chamber with converging artery wick could remove heat flux over 350 W/cm^2 with a thermal resistance as low as 0.075 K·cm^2/W. Lu *et al.* [40] presented an AlSi vapor chamber prototype with graphite foam wick. Attribute to the high thermal conductivity of graphite, the 25 mm × 25 mm × 6 mm vapor chamber can dissipate 80 W/cm^2 heat flux with a heater size of 10 mm × 10 mm and ethanol as working fluid, which was superior to Cu sintered wick. Higher heat flux can be dissipated with water as working fluid. Chen *et al.* [32] selected Cu-diamond wick for their 90 mm × 90 mm × 4.2 mm vapor chambers to take advantage of the high thermal conductivity (2400 W/m·K) of the diamond. By mixing Cu with diamond at different ratios (4:1, 6:1 and 8:1) and capture the temperature image of vapor chamber at different heat loads using IR camera, a low thermal resistance of 0.07 K/W can be demonstrated at a heat load of 360 W. Vapor chamber with Cu-diamond wicks performed superior to solid copper block and sintered Cu wick vapor chambers.

Polymer Vapor Chambers

Some literature on metal vapor chambers were summarized in the aforementioned section. As discussed, metal was usually selected as the casing material for vapor chamber, this was originated from the high thermal conductivity, high mechanical strength, ease of fabrication and excellent sealing properties. However, the high electrical conductivity of metal and high stiffness made it challenging for metal vapor chambers to be used in some special and compact applications. Therefore, researchers paid attentions to fabricate vapor chambers with polymers [46 – 50], which could take advantages of the electrical insulating property, low cost and high flexibility of polymers.

Oshman *et al.* [49] utilized liquid-crystal-polymer (LCP) to fabricate a remote mode polymer vapor chamber. LCP was selected due to its superior chemical resistance,

excellent sealing, and low water absorption properties. With a condenser size of 20 mm × 20 mm and 10 mm × 10 mm microgrooves bonded with copper mesh evaporator, the vapor chamber was capable of dissipating 11.94 W/cm^2 heat flux. Later, they developed another LCP based vapor chamber with condenser size of 20 mm × 20 mm and evaporator size of 8 mm × 8 mm [46, 47]. Wicks for this vapor chamber were copper mesh integrated with 100 μm tall Cu micropillars fabricated by electroplating. The highest effective thermal conductivity of the vapor chamber was measured to be 1653 W/m·K. The vapor chamber could remove a heat flux of up to 63 W/cm^2. Oshaman *et al.* [48] also tried to use PAVVF4W (Al sandwiched in between of polyethylene terephthalate and polyethylene) to fabricate a larger scale flat heat pipe (130 mm × 70 mm × 1.31 mm). A Cu woven mesh consisted of 3 layers was adopted as the wick. Effective thermal conductivity of this vapor chamber was found to be 4.6 times of that of solid Cu block. Hsieh *et al.* [50] reported the fabrication and testing of silicone-rubber based polymer flat heat pipe with dimensions of 80 mm × 20 mm × 4 mm. The flat heat pipe had Cu mesh as a wick and DI water as working fluid. Tests were conducted at 15 – 90° bending angles with various charging ratios. The optimal performance of the flat heat pipe was achieved at 15° bending angle with 40% liquid charge ratio. It could dissipate 12.67 W heat load with thermal resistance of 5 K/W. Yang *et al.* [51] developed a FR4 polymer based flat heat pipe which was mechanically supported by 1 mm Cu frame. The flat heat pipe had an array of 0.2 mm thermal via to enhance its thermal conductivity. The flat heat pipe was tested under different inclination angles (0°, 90° and-90°) with various charging ratios (0 – 41%). It exhibited lowest thermal resistance of 3.86 K/W, 3.84 K/W, 4.45 K/W at 28% liquid charging and 90°, 0° and –90°, respectively.

Silicon Vapor Chambers

According to the polymer vapor chamber/ flat heat pipes reviewed in the previous section, vapor chambers made of polymer usually possessed high thermal resistance owning to their intrinsically low thermal conductivity. Moreover, there were challenges of utilizing polymer vapor chambers practically, as the high flexibility of the polymer made it hard to sustain a high vacuum. Top and bottom surfaces of polymer vapor chambers tend to

collapse together when it was evacuated. Most importantly, both polymer and metal vapor chambers required additional thermal interface material to be attached to the electronic components. This induces excess thermal interface resistance of the cooling devices. Polymer and metal vapor chambers also had different thermal expansion coefficients to semiconductor devices, which may subject to thermal expansion mismatch that could lead to catastrophic failure in actual use. Thus, to keep up with the development of semiconductor electronic devices and achieve direct integration between cooling and electronic devices, vapor chamber made of Si has drawn the attention of researchers in recent years. The mature Micro-Electro-Mechanical-Systems (MEMS) fabrication technology, higher stiffness, and thermal conductivity than polymer, same thermal expansion coefficient as most of the semiconductor materials make it an excellent material candidate for vapor chambers. The thermal interface resistance and expansion mismatch risks can be eliminated by using integrated Si vapor chambers.

Vadakkan *et al.* [52] performed thermal performance and stress analysis of Si vapor chambers numerically with Brinkman's equation and finite element analysis. They demonstrated that Si vapor chamber can perform equally or even superior to conventional Cu vapor chamber. Meanwhile, 96% reduction of compressive stress can be achieved by substituting Cu vapor chamber with a Si one. Cai *et al.* [53] microfabricated a hexagonal Si vapor chamber with 10 mm hexagonal side length and 2 mm thickness. The vapor chamber was sealed by attaching 2 Si wafers with eutectic bonding. The condenser and evaporator surfaces were covered by 50 μm diameter and 50 μm spacing Si micropillars to transport liquid, while the sidewalls of the vapor chamber had 50 μm wide, 150 μm deep grooves with 50 μm for liquid return. Reliable hermetic sealing was found to be difficult to achieve with eutectic bonding. However, the hexagonal vapor chamber was able to remove 300 W/cm^2 heat flux with 2 mm × 2 mm heater. After that, they developed a square Si vapor chamber prototype and conducted systematic studies in investigating the thermal performance [54] and material compatibility issues of Si vapor chamber [55]. The vapor chamber was fabricated with 3 Si wafers bonded together with glass frit bonding. The footprint of the vapor chamber was 38 mm × 38 mm×3 mm. The condenser side was a 220 μm thick fine micropillar

wick with 10 μm diameter and 15 μm pitch, while the evaporator side was a 300 μm thick coarse square micropillar wick with 200 μm× 200 μm × 300 μm dimensions. 8 supporting posts with 2 mm× 2 mm size was added to enhance the structural strength of the vapor chamber. This Si vapor chamber was proven to have hermetic sealing, high mechanical strength and had a thermal conductivity > 2500 W/m·K. Surface oxidation and working fluid purification were found to be significant in sustaining the high performance of this vapor chamber [55]. Later, Cai *et al.* [56] developed a larger (50 mm × 70 mm) and ultra-thin (1 mm) Si vapor chamber by bonding 3 Si wafers. Like the prototype presented in their previous studies, the new vapor chamber is composed of fine micropillar wick with 10 μm diameter and 15 μm pitch on the condenser, 100 μm coarse micropillars with 50 μm spacing wicks on the evaporator and 100 μm wide grooves on the sidewalls. The top and bottom surface were supported by 13 × 8 posts with diameter of 2 mm. A high effective thermal conductivity of over 10000 W/m·K in both lateral and vertical directions can be demonstrated by this vapor chamber. Yang *et al.* [57] fabricated 2 vapor chambers with the identical size of 40 mm × 35 mm×1.525 mm. The 2 vapor chambers had different wick structures, one with converging microchannels (width 0.1 – 0.3 mm) while another had discrete 0.3 mm microchannels. With a liquid filling ratio of 48%, the vapor chamber with converging microchannels performs superior to the other one, due to a better liquid return with converging microchannels. The Si vapor chamber with converging microchannels had a lowest thermal resistance of 1.46 K/W at 28 W.

The geometries, structures and performance of aforementioned metal, polymer and Si vapor chambers are summarized in *Table 1*.

Table 1: Summary of vapor chamber literature: list of metal, polymer and silicon vapor chamber geometries, structures and performances

Literature	Chamber material	Wick Type	Working fluid	Vapor Chamber Size	Heater Size	Results
Chen *et al*. [26]	Cu	0.14 mm thick Cu sintered powder, porosity 0.68	Water	76 mm × 60 mm × 6 mm	30 mm × 30 mm	R = 0.18 W/K
Ranjan *et al.* [29]	CuMoCu alloy	100 µm Cu sintered powder, porosity 0.5	Water	30 mm × 30 mm × 1 – 3 mm	5 mm × 5 mm	q'' > 100 W/cm^2
Ji *et al.* [30]	Cu	Cu foam, porosity 0.95	Water	95 mm (diameter) × 44 mm	0.785 cm^2	R_{min} = 0.03 K/W q''=450 W/cm^2
Hsieh *et al.* [31]	Cu + glass	No wick	Water	300 mm × 300 mm × 100 mm	80 mm × 80 mm 100 mm×200 mm 80 mm × 300 mm	Total R = 0.5 K/W Spreading R = 0.2 K/W q''=220 W/cm^2
Chen *et al.* [32]	Cu	0.6 mm thick 200/325 Cu powder: 140/170 diamond powder = 4:1	Water	90 mm × 90 mm × 4.2mm	25 mm × 25 mm	Total R = 0.12 K/W (50 W) Total R = 0.1 K/W (360 W)
Chen *et al.* [32]	Cu	0.6 mm thick 200/325 Cu powder: 140/170 diamond powder = 6:1	Water	90 mm × 90 mm × 4.2mm	25 mm × 25 mm	Total R = 0.15 K/W (50 W) Total R = 0.1 K/W (360 W)
Chen *et al.* [32]	Cu	0.6 mm thick 200/325 Cu powder: 140/170 diamond powder = 8:1	Water	90 mm × 90 mm × 4.2mm	25 mm × 25 mm	Total R = 0.19 K/W (50 W) Total R = 0.15 K/W (360 W)
Chen *et al.* [32]	Cu	0.6 mm thick 80/140 Cu powder: 80/100 diamond powder = 6:1	Water	90 mm × 90 mm × 4.2mm	25 mm × 25 mm	Total R = 0.12 K/W (50 W) Total R = 0.07 K/W (360 W)
Go *et al.* [33]	Al	Stainless steel wick with concentrically converging arteries	Water	40 mm × 40 mm × 2 mm	12 mm × 12 mm	q'' = 80 W/cm^2 R_{min} = 0.76 K/W
Ju *et al.* [34]	Cu	Converging liquid arteries	Water	100 mm × 100 mm	10 mm× 10 mm	Effective R_{min} = 0.075 K·cm^2/W q'' >350 W/cm^2
Wong *et al*. [36]	Cu	Sintered Cu	Degassed DI water	100 mm × 89 mm	21 mm × 21 mm 11 mm × 11 mm	Total R = 0.08 K/W (80 W) Total R = 0.042 K/W (350 W)
Tang *et al.* [37]	Cu	Sintered Cu particle	DI water	90 mm × 90 mm × 3 mm	10 mm × 10 mm	R_{min} = 0.08 K/W q'' =300 W/cm^2
Sigurdson *et al.* [38]	Ti	250 µm deep and 350 µm wide microgrooves, covered by Ti nanowires	Water	300 mm × 76 mm × 45 mm	24 heat sources	Effective k = 8000 W/cm·K
Chen *et al.* [39]	Cu	0.5 mm Cu sintered powder, porosity 0.36	Water	81 mm × 76 mm × 5 mm	10 mm × 10 mm 20 mm × 20 mm 40 mm × 40 mm	R = 0.092 W/K (30 W) R = 0.074 W/K (60 W)
Lu *et al.* [40]	AlSi alloy	1 mm thick Graphite foam, porosity 0.71	Ethanol	25 mm × 25 mm × 6 mm	10 mm × 10 mm	q'' =80 W/cm^2 R = 0.4 W/K

Ding *et al.* [41]	Ti	5 μm diameter, 10 μm pitch and 50 μm height Ti micropillars covered by 200 nm Ti nanowires	Water	30 mm × 30 mm × 0.6 mm		Effective k = 350 W/cm·K (7.2 W)
Chen *et al.* [42]	Al	Sintered Al powder, porosity 0.32	Acetone	58 mm × 58 mm × 6 mm	13.91 mm × 13.91 mm	R_{min} = 0.69 K/W
Chen *et al.* [42]	Al	Axial grooves, 0.4 mm width, 0.91 – 1.65 mm depth	Acetone	58 mm × 58 mm × 6 mm	13.91 mm × 13.91 mm	R_{min} = 0.72 K/W
Ji *et al.* [44]	Cu	Cu foam	Water, acetone, ethanol	100 mm (diameter) × 8 mm	–	R_{min} = 0.09 K/W q'' = 216 W/cm^2
Oshman *et al.* [46, 47]	Liquid-crystal-polymer	100 μm Cu micropillars + copper woven mesh (51 μm diameter, 76 μm spacing)	DI water	40 mm × 40 mm × 1.2 mm	8 mm × 8 mm	q'' = 63 W/cm^2 k = 1653 W/m·K
Oshman *et al.* [48]	PAVVF4W	3 Cu woven mesh layers	DI water	130 mm × 70 mm × 1.31 mm	8 mm × 8 mm	4.6 times thermal conductivity of Cu block
Oshman *et al.* [49]	Liquid-crystal-polymer	200 μm wide grooves + copper woven mesh	DI water	20 mm × 20 mm condenser 10 mm × 10 mm evaporator	10 mm × 10 mm	q'' = 11.94 W/cm^2
Hsieh *et al.* [50]	Silicone – rubber	Cu mesh	DI water	80 mm × 20 mm × 4 mm	1 mm × 1 mm	Q = 12.67 W R = 5 K/W
Yang *et al.* [51]	FR 4 + 1 mm Cu frame	2 layers of Cu mesh (fine mesh 50 μm diameter; coarse mesh 115 μm diameter)	Degassed DI water	–	–	R = 3.86 K/W (90°) R = 3.84 K/W (0°) R = 4.45 K/W (–90°) Charge ratio 28%
Cai *et al.* [53]	Si	Si micropillar, 50 μm diameter and 50 μm spacing	Water	10 mm (hexagonal side length) × 2 mm	2 mm × 2 mm	q'' = 300 W/cm^2
Cai *et al.* [54]	Si	Condenser: fine Si micropillar, 10 μm diameter and 15 μm spacing Evaporator: square Si micropillar, 200 μm× 200 μm × 300 μm	Water	38 mm × 38 mm ×3 mm	–	k > 2500 W/m·K
Cai *et al.* [56]	Si	Condenser: fine Si micropillar, 10 μm diameter and 15 μm spacing Evaporator: square Si micropillar	Water	50 mm × 70 mm × 1 mm	5 mm × 8 mm	Lateral & vertical k > 10000 W/m·K

1.3. Evaporators

1.3.1. Introduction to Evaporators

Evaporators are made of porous wicks that can circulate working fluid passively by capillary effect, by which water can flow in the porous media without the assistance of external forces. As discussed in the foregoing literature, the evaporator is the determinant part that governs the thermal performance of a vapor chamber. This was attributed to the large thermal resistance, highest temperature drop [31, 36] and the essential role of evaporators in the operation cycles of a vapor chamber. Therefore, a vapor chamber with good design significantly relies on superior evaporator design. An excellent evaporator should possess high thermal conductivity, large capillary force, and low viscous resistance to remove heat efficiently. There are two significant parameters that indicate the performance of an evaporator, namely capillary pressure P_{cap} and permeability K. Capillary pressure P_{cap} refers to the pressure developed in the porous evaporator wick that drives liquid to flow. It is developed by the pressure difference across the interface between two immiscible fluids (*e.g.* water and air). Permeability K is the capability of porous media to allow fluid to pass through. Evaporators with high capillary pressure P_{cap} to drive liquid propagation and high permeability K to minimize the viscous drag are preferred. According to different structures and fabrication methods, evaporator wicks can be divided into sintered particle wicks, metal meshes, microgrooves, and micropillars *etc.*. Each category of evaporator wick will be discussed in detail below.

1.3.2. Types of Evaporator Wicks

Wire Meshes/Screen Wicks

Wire meshes/screen are the most widely available wick type in heat pipes and vapor chambers. It is composed of multi-layer braided structures of metal wires as shown in *Figure 7(a)*. This kind of evaporator wick offers high permeability and thermal conductivity. However, the selection of mesh sizes is limited by the manufacturing constraints and wire meshes wick has low permeability.

Sintered Particle Wicks

Sintered particle wicks are fabricated by packing, pressing and heating metal or glass particles to form a continuous and compact porous wick. Cu sintered particle wicks are

the most commonly used type of vapor chamber wick, as discussed in [32, 36, 37]. The Cu sintered wick inside a heat pipe is shown in *Figure 7(b)*. Sintered particle wicks offer advantages of high capillary pressure, anti-gravity operation that can handle large heat flux. However, the sintering process requires high temperature and is hard to control. Heterogeneous wicks may be obtained due to the non-uniform particle distribution and packing. Moreover, the permeability of sintered particle wick is relatively low and the small contact areas between particles result in high contact thermal resistance of the wick.

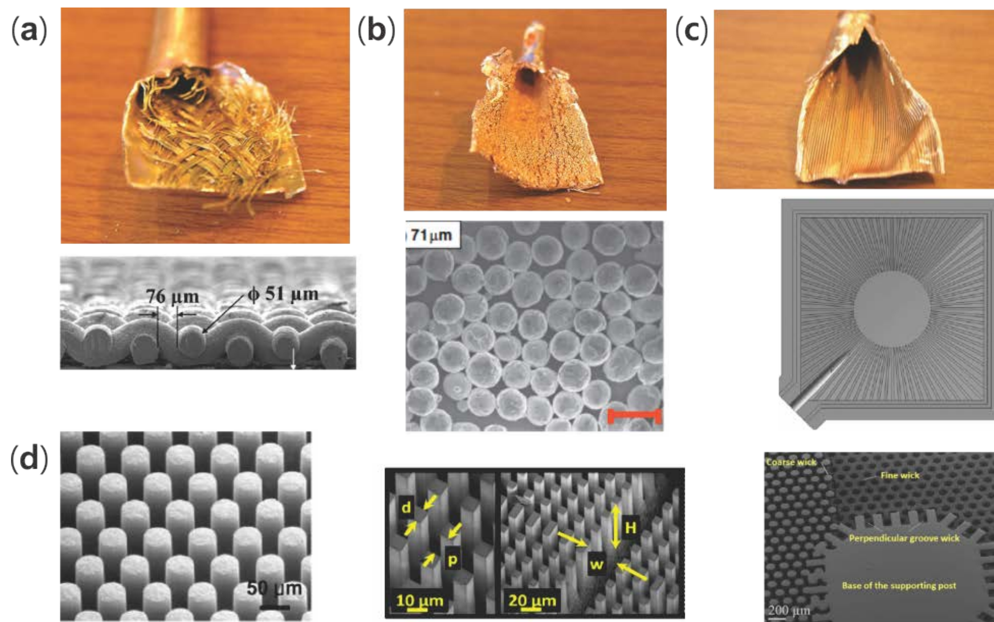

Figure 7: Various kinds of evaporator wicks: (a) Wire meshes/screen wick: Wire meshes in a Cu heat pipe [58] and SEM image of woven Cu mesh made of 56 μm wires with 76 μm spacing by Oshman et al. [46] (b) Sintered particle wick: heat pipe with exposed sintered Cu particle wick [58] and SEM image of sintered Cu particle wick with particle diameter of 71 μm, scale bar is 100 μm, fabricated by Ju et al. [34] (c) Microgroove wick: heat pipe with exposed microgroove wick [58] and design of axial converging microchannel wick by [42] (d) Micropillar wick: hexagonal Cu micropillars [59], square Si micropillars [60] and cylindrical Si micropillars [56]

<u>Microgrooves/Microchannels/Arteries Wick</u>

Microgrooves with various width, depth and different layouts, such as parallel grooves, radially converging grooves etc., are fabricated on flat substrate surfaces by

micromachining. *Figure(c)* shows the heat pipe with microgroove wicks. Microgrooves provide high permeability, high thermal conductivity and are easy to fabricate. However, the capillary pumping by microgrooves is limited due to the large sizes of microgrooves, which are often a few hundred micrometers. Grooves with smaller sizes and higher precisions are difficult to make and may lead to high manufacturing costs.

Micropillar Wicks

In recently years, evaporator wicks with micropillar structures have drawn much attention. Micropillar wicks compose of small posts with micrometer sizes and various shapes, such as circular, pyramidal, hexagonal, square and so on, as shown in *Figure 7(d)*. The micropillars were fabricated by electroplating of metals or Micro-Electro-Mechanical-Systems (MEMS) microfabrication. Micropillar wicks are promising evaporator structures that have high thermal conductivity, high capillary pressure, extended thin film evaporation areas and good thermal contact between the micropillars and substrate. As micropillar wicks have uniformly and periodically distributed micropillars, the modeling and performance prediction are rather simple to achieve compared with sintered particle wicks. Due to the aforementioned reasons, micropillars have become excellent candidates for vapor chamber evaporators and were widely studied.

1.3.3. Uniform Micropillar Evaporators

Due to the highly ordered structures of micropillars, extensive theoretical modeling has been established to predict the permeability K and capillary pressure P_{cap} of micropillar structure wicks.

Sangani *et al.* [61] modeled the viscous permeability of micropillar arrays with square and hexagonal shapes. This model was valid for micropillars with very sparse or very dense arrays. Drummond *et al.* [62] and Gebart *et al.* [63] modeled pillar permeability in high and low porosity homogeneous pillar arrays with cell approach and lubrication approximate, respectively. After that, Yazdchi *et al.* [64, 65] compared, combined and extended their models to establish an equation that held for all porosities and even randomly distributed micropillar arrays. Sobera *et al.* [66] conducted scaling analysis of

Stokes flow with Darcy's law. The characteristic length was taken as half of the micropillar spacing while characteristic velocity was defined as superficial velocity divided by porosity. Tamayol *et al.* [67, 68] constructed a permeability model by solving Stokes equation with 2D flow assumption. The velocity profile was assumed to be parabolic. The model can be further extended to micropillar arrays with a different pitch in x and y directions. Zhang *et al.* [69] developed the permeability model semi-analytically by assuming the micropillars as straight walls with a width of micropillar diameter. Permeability was obtained by solving Navier-Stokes Equation and Darcy's law. Xiao *et al.* [70] obtained the expression for velocity profile of flow through cylindrical micropillar arrays by solving Brinkman's equation. They also provided a semi-analytical solution for capillary pressure with energy minimization approach, where capillary pressure was denoted as the surface energy change per unit volume of micropillar cell. Srivastava *et al.* [71] predicted the permeability of micropillar arrays by simulation. Hale *et al.* [72] summarized and compared various permeability models to their simulation results. They developed their own permeability model by assuming a 2D velocity profile and dividing the micropillar unit cell into two regions. The first section was defined as the region without any micropillars where a constant channel width was used, while the width of section region with micropillars varies from l to $l - d$. Permeability was obtained for different velocity profiles. According to the comparison with simulation results, their model was proven to be accurate for $h/d \leq 5$ while the Brinkman permeability model of Xiao *et al.* [70] captured the permeability with high accuracy for $h/d > 5$. An optimal micropillar spacing exists for each micropillar height and the spacing increased with taller micropillars. Ranjan *et al.* [73] obtained a correlation between the permeability and geometry of micropillar structures with cylindrical, pyramidal and conical micropillars. They also compared the performance of micropillar structures with traditional sintered particle wicks with spherical structures. It was concluded that the micropillar structures outperformed sintered particle wicks, especially for high heat flux vapor chambers. For the aforementioned permeability models, a flat liquid meniscus was assumed for simplification purpose. However, this will lead to deviations in predicting the actual permeability where the liquid meniscus had a curvature. Byon *et al.* [74] constructed a

semianalytical model for squarely and hexagonally packed micropillar arrays by considering the meniscus curvature effect and extending the model of Sangani *et al.* [61]. Their model was proven to have high accuracy with < 5% error compared to experimental measured and simulated results for $0.06 < d/l < 0.6$ and $h/l > 0.2$. Permeability was found to be over predicted by assuming a flat liquid meniscus. Adera *et al.* [75] adopted the same approach in predicting the permeability of micropillar structures with meniscus shape effect. Instead of the semi-analytical approach of modeling the meniscus shape, the effective height of liquid meniscus was derived theoretically by assuming a linear variation of meniscus thickness from the edge of micropillar to the center.

Besides the widely studied permeability models, capillary pressure of micropillar arrays was also modeled by Xiao *et al.* [70]and Srivastava *et al.* [71]. Xiao *et al.* [70] predicted the permeability by energy minimization approach and the meniscus shapes for various micropillar geometries were simulated using Surface Evolver. Their model predictions were validated experimentally and showed great accuracy. Srivastava *et al.*[71] calculated capillary pressure by determining the force as energy change per unit distance. The capillary pressure was defined as force per cross-sectional area. Adera *et al.* [75] derived the model for capillary pressure in micropillar arrays through force balance of capillary force and surface tension. Zhu *et al.* [76] predicted capillary pressure in cylindrical micropillars more accurately by capturing the change of 3D meniscus curvature along the direction of wicking. They were also able to predict the dryout heat flux in micropillar arrays by defining the dryout as the point where the receding contact angle has been reached.

Expressions for permeability K and capillary pressure P_{cap} discussed above are summarized in *Table 2*.

Table 2: Summary of literature on permeability K and capillary pressure P_{cap} models in micropillar arrays

Literature	Model	Applicable to
Sangani *et al.* [61]	$K_S = l^2 \frac{lnc^{-1/2} - 0.738 + c - 0.887c^2 + 2.038c^3 + o(c4)}{4\pi}$ $c = \frac{\pi d^2}{4l^2}$, $K_{S,h} = \frac{l^2 \ln(c^{-0.5} - 0.745 + c - 0.25c^2)}{4\pi}$ $c = \frac{\pi d^2}{2\sqrt{3}l^2}$	Hexagonally and Squarely packed cylindrical micropillar arrays, $d/l < 0.57$
Drummond *et al.* [62]	$K_D = \frac{1}{32c}(\ln(\frac{1}{c}) - 1.476 + \frac{2c - 0.796c^2}{1 + 0.489c - 1.605c^2})$	Squarely packed cylindrical micropillar arrays with high porosity
Gebart *et al.* [63]	$K_G = \frac{4}{9\sqrt{2}\pi}(\frac{l}{d} - 1)^{5/2}$	Squarely packed cylindrical micropillar arrays with low porosity
Yazdchi *et al.* [64, 65]	$K_Y = \frac{K_G}{1 + 0.336(\pi/4 - \varepsilon)} + (K_D - \frac{K_G}{1 + 0.336(\pi/4 - \varepsilon)})\frac{1 - \tanh(\frac{0.25 - \varepsilon}{0.037})}{2}$	Squarely packed cylindrical micropillar arrays
Tamayol *et al.* [67, 68]	$K_{\mathrm{T}} = d^2\{\frac{12\sqrt{\pi/4c} - 1}{c\sqrt{\pi/4c}}[\frac{2 - (1.274\varepsilon - 0.274)}{2}] + \frac{18 + 12(\pi/4c - 1)}{\sqrt{\pi/4c}(1 - \sqrt{\pi/4c})^2} + \frac{18\sqrt{\pi/4c}[\tan^{-1}(\frac{1}{\sqrt{\pi/4c} - 1}) + \frac{\pi}{2}]}{(\pi/4c - 1)^{5/2}}\}^{-1}$	Squarely packed micropillar arrays, with or without the same spacing in x and y directions
Zhang *et al.* [69]	$K_{\mathrm{Z}} = \left[\frac{3(l - d)}{(l - d)h^2} + \frac{12.0256d}{(l - d)^3}\right]^{-1}$	Squarely packed cylindrical micropillar arrays
Xiao *et al.* [70]	$K_X = \frac{1}{K_S d^2} + \frac{\mu}{-\frac{dP}{dx}d^2 h}\left[\frac{A}{\sqrt{\varepsilon/K_S}}(e^{\sqrt{\frac{\varepsilon}{K}}h} - 1) - \frac{B}{\sqrt{\varepsilon/K_S}}(-e^{\sqrt{\frac{\varepsilon}{K}}h} - 1)\right]$ $A = \frac{dP}{dx}\frac{\exp(-h\sqrt{\varepsilon/K_S})}{K_S\mu[\exp(h\sqrt{\varepsilon/K_S}) + \exp(-h\sqrt{\varepsilon/K_S})]}$ $B = \frac{dP}{dx}\frac{\exp(h\sqrt{\varepsilon/K_S})}{K_S\mu[\exp(h\sqrt{\varepsilon/K_S}) + \exp(-h\sqrt{\varepsilon/K_S})]}$	Squarely packed cylindrical micropillar arrays
Srivastava *et al.* [71]	$K_{S2} = \frac{l}{30h}(\frac{\phi_1}{\phi_2 - 1})^{1.17}(\phi_2 - 1)^{2.5}$	Squarely packed cylindrical micropillar arrays
Ranjan *et al.* [73]	Cylindrical: $K_R = \frac{27.6r^2\varepsilon^{8.43}}{(1 - \varepsilon)^{-2.88}}, r = 0.5d$,Conical: $K_R = \frac{0.0964r^2\varepsilon^{3.55}}{(1 - \varepsilon)^{0.6}}$,Pyramidal: $K_R = \frac{9.3\times10^4 r^2\varepsilon^{27.4}}{(1 - \varepsilon)^{-4.55}}$	Squarely packed cylindrical, conical and pyramidal micropillar arrays
Hale *et al.* [72]	$K_H(u_s = 1) = \left\{3\frac{\phi_2 - 1}{\phi_1^2\phi_2} + \left(\int_{-\frac{1}{2\phi_1}}^{\frac{1}{2\phi_1}}\frac{h}{u_{avg}w_{eff}}d(x/h)\right)(\frac{2}{\phi_1^2})\right\}^{-1}$, $K_H(u_s = 0) = \left\{2\frac{\phi_2}{\phi_1^2\phi_2 u_{avg}} + \left(\int_{-\frac{1}{2\phi_1}}^{\frac{1}{2\phi_1}}\frac{h}{u_{avg}w_{eff}}d(x/h)\right)(\frac{2}{\phi_1^2})\right\}^{-1}$ $K_H(u_s = f(x)) = \left\{\frac{2}{\phi_1^2\phi_2}\int_1^{\phi_2}\frac{1}{u_{avg}}d(x/d) + \left(\int_{-\frac{1}{2\phi_1}}^{\frac{1}{2\phi_1}}\frac{h}{u_{avg}w_{eff}}d(x/h)\right)(\frac{2}{\phi_1^2})\right\}^{-1}$, $\phi_1 = h/d, \phi_2 = l/d$	Squarely packed cylindrical micropillar arrays

Byon *et al.* [74]	$K_B = A_1 A_2 K_S \left[1-\frac{\exp(2\sqrt{\frac{\varepsilon}{K_S}}h_{eff})-1}{\sqrt{\frac{\varepsilon}{K_S}}h_{eff}(\exp(2\sqrt{\frac{\varepsilon}{K_S}}h_{eff})+1)}\right]$ $A_1=\frac{h_{eff}+\frac{\varepsilon d}{4(1-\varepsilon)}}{h+\frac{\varepsilon d}{4(1-\varepsilon)}}$, $A_2=\frac{h_{eff}}{h}$ $h_{eff} = h-d[0.01476+0.85009\cos\theta+0.215\frac{d}{l}+0.18979(\cos\theta)^2-3.46929(\frac{d}{l})(\cos\theta)$ $-0.28868(\frac{d}{l})^2+1.05357(\frac{d}{l})(\cos\theta)^2+3.12583(\cos\theta)(\frac{d}{l})^2-1.4243(\frac{d}{l})^2(\cos\theta)^2]$	Squarely packed cylindrical micropillar arrays
Byon *et al.* [74]	$K_{B,h} = A_1 A_2 K_S \left[1-\frac{\exp(2\sqrt{\frac{\varepsilon}{K_{S,h}}}h_{eff})-1}{\sqrt{\frac{\varepsilon}{K_{S,h}}}h_{eff}(\exp(2\sqrt{\frac{\varepsilon}{K_{S,h}}}h_{eff})+1)}\right]$ $A_1=\frac{h_{eff}+\frac{\varepsilon d}{4(1-\varepsilon)}}{h+\frac{\varepsilon d}{4(1-\varepsilon)}}$, $A_2=\frac{h_{eff}}{h}$	Hexagonally packed cylindrical micropillar arrays.
Adrea *et al.* [75]	$K_{B,h} = A_1 A_2 K_S \left[1-\frac{\exp(2\sqrt{\frac{\varepsilon}{K_{S,h}}}h_{eff})-1}{\sqrt{\frac{\varepsilon}{K_{S,h}}}h_{eff}(\exp(2\sqrt{\frac{\varepsilon}{K_{S,h}}}h_{eff})+1)}\right]$ $A_1=\frac{h_{eff}+\frac{\varepsilon d}{4(1-\varepsilon)}}{h+\frac{\varepsilon d}{4(1-\varepsilon)}}$, $A_2=\frac{h_{eff}}{h}$ $h_{eff}=h-\frac{(\sqrt{2}l-d)(1-\sin\theta_{rec})}{4\cos\theta_{rec}}$	Squarely packed cylindrical micropillar arrays
Xiao *et al.* [70]	$P_{cap,X}=\frac{\Delta E}{\Delta V}=\frac{\sigma rf\cos\theta\pi dh+\sigma\cos\theta A_p-\sigma A_m}{\Delta V}$ $A_p=l^2-\frac{1}{4}\pi d^2$ $A_m=[0.43+0.73rf\cos\theta+3.76(\frac{d}{l})-0.046(rf\cos\theta)^2-5.53(rf\cos\theta)(\frac{d}{l})-4.05(\frac{d}{l})^2$ $-0.124(rf\cos\theta)^3+1.77(rf\cos\theta)^2(\frac{d}{l})+4.66(rf\cos\theta)(\frac{d}{l})^2]\times(l^2-\frac{\pi d^2}{4})$ $\Delta V=hA_p-[-0.175-0.345rf\cos\theta+4.07(\frac{d}{l})+0.924(rf\cos\theta)^2-5.83(rf\cos\theta)(\frac{d}{l})-2.80(\frac{d}{l})^2$ $-0.439(rf\cos\theta)^3+2.41(rf\cos\theta)^2(\frac{d}{l})+2.71(rf\cos\theta)(\frac{d}{l})]\times A_p(l-d)$	Squarely packed cylindrical micropillar arrays
Srivastava *et al.* [71]	$P_{cap,S}=\frac{\sigma}{l^2h}[\cos\theta(\pi dh+l^2-\frac{\pi d^2}{4})-(l^2-\frac{\pi d^2}{4})]$	Squarely packed cylindrical micropillar arrays

In addition to the theoretical models constructed on micropillar arrays with various shapes and packing styles, thermal tests were also widely conducted to determine the maximum heat transport capabilities of micropillar arrays. Nam *et al.* [59, 77, 78] fabricated squarely packed hexagonal Cu micropillars with a total area of 3 cm^2 via electroplating method. The micropillars were covered by chemically synthesized nanostructured CuO layer to further enhance its wettability. The capillary rate of rising experiments was conducted on micropillar arrays with different geometries. The liquid propagation distance was captured using a high-speed camera and plotted as a function of time. Nano-structuring of micropillars was found to facilitate the capillary performance and enlarge the areas for evaporation without affecting the permeability significantly. Micropillars with taller height and high porosity were found to have larger permeability. Cai *et al.* [79] modeled and tested micropillar wicks with 2 extreme cases, that were wick with small thickness but large heater and wick with large thickness and a small heater. The two extreme cases were defined as the heater width/ wick thickness ratio <0.1 and >1. For a wick with small thickness but the large heater, liquid flow resistance played a dominant role and the dryout heat flux was found to be determined by a parameter called liquid phase geometric number. The liquid phase geometric number was $d \times$ wick thickness divided by heater area. On the contrary, the maximum heat flux of the micropillar wick was governed by the vapor phase geometric number *d/* wick thickness in the case of thick wick with a small heater. Ravi *et al.* [80] reviewed the permeability models in the literature and constructed their model based on Darcy's law in predicting the maximum heat load that the micropillar wicks can handle. It was found that the capillary pressure model of Xiao *et al.* [70]and Srivastava *et al.* [71] had an overestimation and underestimation, respectively compared to the experimental results. This was because Xiao *et al.* [70] considered the surface energy change due to the curvature of liquid meniscus while Srivastava *et al.* [71] calculated surface energy change due to the liquid front propagation only. Capillary pressure model of Xiao *et al.* [70] was found to have a higher accuracy, which was in consistent with Hale *et al.* [72]. Hornor *et al.* [81] performed optimization of micropillar geometries through parametric sweep based on the model of Ravi *et al.* [80]. They reported a 3 – 4 times performance

enhancement for micropillar wicks with optimized geometries. Adera *et al.* measured the maximum heat flux of micropillar wicks before the onset of nucleate boiling. The evaporator wicks were tested in the horizontal direction with degassed water supplied from 4 edges of the sample. With a wicking distance of 0.5 cm, a heat flux of 46 W/cm^2 was demonstrated before the onset of boiling. Zhu *et al.* [76] validated their model with varied liquid meniscus curvature along the wicking direction by conducting thermal tests with 45° tilted angle of micropillar evaporators with varies geometries. $d/h = 0.4 – 0.6$ and $l/d \sim 3$ were recommended for micropillars with higher dryout heat flux. Dryout heat flux was also found to decrease with $L^{2.}$

Performance of uniform micropillar evaporators experimentally tested in the literatures are summarized in *Table 3*.

1.3.4. Biporous Evaporators

For uniform micropillar evaporators with periodically distributed micropillars discussed in *1.3.3*, there was only one effective pore size. Although a high capillary pressure P_{cap} and permeability K are desired for better liquid transportation and heat dissipation capabilities of evaporator wicks, P_{cap} and K are in a competing effect. For example, micropillar evaporators with a higher porosity have a larger permeability K, but the capillary pressure P_{cap} is low. Therefore, by combining structures with different effective pore sizes, the advantage of high permeability and high capillary pressure of different structures can be blended. This is the reason of using hybrid wicks in the vapor chambers fabricated by Sigurdson *et al.* [38] Ding *et al.* [41] and Oshman *et al.* [46, 47]. The hybrid wick with two or more distinguished effective pore sizes is known as biporous wicks. In biporous evaporator, the pores with large size can act as low flow resistance pathway which small pores can generate large capillary pressure to extend the capillary limit of a vapor chamber.

A large volume of published studies on biporous evaporators has focused on the sintered powder biporous evaporators with big clusters of small particles. Cao *et al.* [82] investigated the evaporative heat transfer of 9 cm × 30 cm sintered Cu biporous wick with large/small pore ratio of 200/80, 400/80, 800/80 μm. Enhancement in both critical heat flux and heat transfer coefficient was demonstrated by biporous evaporators

compared to that of monoporous evaporators. Semenic *et al.* [22, 83 – 87] fabricated sintered Cu biporous evaporators with a small pore size of 53 – 63 μm and large pore size of 500 – 710 μm. A highest critical heat flux of 494 W/cm^2 was dissipated at a superheat of 128 °C with 1 mm thick wick which had a large to small pore size ratio of 600/60 μm. Optimization of biporous evaporator wick was found to be determined by the best combination of particle size, bonding area between particles, cluster diameter, evaporator thickness and radius. Yeh *et al.* [88] investigated the performance of sintered Ni biporous evaporators. A 6 times higher heat transfer coefficient was demonstrated by the biporous evaporators compared to that of monoporous evaporators. Pore former content was found to play an important role in determining the heat transfer coefficient, which influenced the interconnections between pores and thin film evaporation areas. Sintered Ni biporous evaporators were also studied by some literatures [89 – 91]. Using methanol as the working fluid, heat load of 20 – 160 W was spread with effective thermal resistance of 0.46 – 2.28 °C/W. Byon *et al.* [92] measured the capillary pressure and permeability of sintered glass powder biporous evaporators with particle size of 40 – 600 μm and cluster size of 250 – 1440 μm. A semianalytical model was developed to predict the capillary performance of sintered powder biporous evaporators. A cluster/particle size ratio of 4 – 6 was preferred for biporous evaporators with best capillary performance. Pore sizes, interconnectivity between pores and the evaporator roughness of sintered evaporator wicks highly depend on sintering temperature and time. Therefore, although excellent heat transfer performance was demonstrated by sintered powder biporous evaporators, it is rather difficult to control the sintering process and predict the performance of sintered powder evaporators [84]. Thermal performance of 1 cm × 1 cm carbon nanotube (CNT) biporous evaporator with 210 – 300 μm tall straight and zigzag CNT stripes were investigated by Cai *et al.* [21, 93, 94]. CNT was chosen due to its high thermal conductivity, nano pore size and large porosity. With a heater area of 0.2 cm × 0.2 cm, heat flux of 770 W/cm^2 can be achieved with straight stripe CNT biporous evaporator and dryout was defined as the inflexion point on the boiling curve.

To meet the thermal management challenges brought by semiconductor industry development, provide direct on-hotspot cooling without any thermal interface materials

and eliminate thermal expansion mismatch, biporous evaporators made of silicon have drawn increasing attention in recent years. Coso *et al.* [60] fabricated 1 cm ×1 cm silicon biporous evaporators composed of square micropillars (6 – 29 μm in diameter, 56 – 243 μm tall) separated by 30/61 μm microchannels. A critical heat flux of 119.6 (± 4.2) W/cm^2 was achieved with heat transfer coefficient of 20.7 (± 2.4) W/cm^2·K. Heat transfer coefficient was found to increase with the decrease of pore size. Silicon micropost based biporous evaporators with a square array, staggered array, diamond array, groove array and pseudo groove array were studied by Byon *et al.* [95]. The capillary performance of groove and square array evaporators were found to be 35% and 31% higher than that of monoporous evaporators, while a decrease of solid fraction led to a higher capillary performance. Ravi *et al.* [96] explored the heat transfer performance of in-plane biporous evaporator with various pore sizes throughout the wick and out-of-plane biporous evaporator with porous meshes suspended over micropillar structures. Change of dryout mechanism was observed with the addition of woven stainless steel meshes and dryout heat flux was mainly determined by mesh thickness, while dryout was postponed by thicker meshes.

Performance and geometries of the sintered particle biporous wicks, CNT biporous wicks and Si biporous wicks discussed in the foregoing researches are summarized in *Table 4*.

1.4. Motivations and Objectives of the Thesis

As discussed in *1.2*, silicon vapor chamber is a promising candidate to address the thermal expansion mismatch issue, eliminate the thermal interface resistance and enable direct integration of the cooling device with electronic components. The mature Micro-Electro-Mechanical-System (MEMS) fabrication process, relatively high stiffness and thermal conductivity of Si compare to the polymer can facilitate the fabrication of Si vapor chambers with small form factor, compact design, light weight and excellent heat dissipation capabilities. Evaporators with micropillar structures were proven to be advantageous in terms of the high capillary pressure, permeability, good thermal contact and large thin film evaporation areas according to *1.3*. The liquid transportation and heat dissipation capability of evaporators can be further enhanced with the introduction of biporous structures as evidenced from *1.3.4*.

Although significant insights have been made on vapor chambers and micropillar evaporators, systematic and comprehensive studies are still lacking. The micropillar geometries for uniform and biporous evaporators tested in most of the foregoing studies were chosen randomly. Moreover, the temperature rise of evaporator samples was not taken into consideration by the previous optimization study [72], instead, only the dryout heat flux was considered. However, limitations on the temperature rise of evaporators are rather crucial in the actual case, as the evaporator or vapor chamber that can dissipate large heat flux but result in considerable temperature rise is lack of practical use. In addition, the dryout heat flux of biporous evaporators was not correlated to the biporous evaporator geometrics analytically in any of the literature. Models in predicting biporous evaporator dryout heat flux were inadequate. Apart from the aforementioned research gaps, the micropillar structure in the adiabatic region for liquid transportation and evaporator region for both liquid circulation and heat transfer in a vapor chamber should be optimized separately based on their functionalities.

Therefore, this thesis aims at the modeling, designing, and fabrication of Si vapor chambers with thin thickness and excellent performance. This was achieved by conducting comprehensive and systematic studies of uniform evaporators and biporous evaporators with microchannels. The micropillar geometries of the uniform evaporator, biporous evaporator, Si vapor chamber evaporator and adiabatic sections will be optimized with constrained temperature rise.

Table 3: Summary of literature on thermal performance of uniform micropillar wicks

Literature	Pillar Material	Pillar Shape	Working Fluid	Achievable Heat Flux (W/cm^2)	Heater Size (cm^2)	Wicking Length (cm)	Pillar Diameter *d* (µm)	Pillar Pitch *l* (µm)	Pillar Height *h* (µm)	Dryout (W)
Zhang *et al.* [69]	Si	Nanowire		1.4	–	–	0.11	0.24	3.5	–
Zhang *et al.* [69]	C	Nanotube		1	–	–	0.93	1.3	3	–
Adera *et al. [75]*	Si	Cylindrical	Water	46	1 × 1	0.5	5	12	82	
Cai *et al.* [97]	Si	Hexagonal	Water	300	0.2 × 0.2	0.87	50	100	250	12
Miers *et al.* [98]	Si	Cylindrical	DI water	13			30	150	40	–
Miers *et al.* [98]	Si	Cylindrical	DI water	7			30	190	40	–
Ding *et al.* [99]	Ti	Cylindrical	DI water	–	0.5 × 3	2.5	5	10	50	7.2
Ding *et al.* [99]	Ti	Cylindrical	DI water	–	0.5 × 3	2.25	100	150	50	8.65
Nam *et al.* [78]	Cu/CuO	Hexagonal	Water	800	0.2 × 0.2	1.6	50	80	100	32
Nam *et al.* [78]	Cu/CuO	Hexagonal	Water	950	0.2 × 0.2	1.6	50	100	100	38
Nam *et al.* [78]	Cu/CuO	Hexagonal	Water	190	0.5 × 0.5	1.75	50	70	100	47.5
Nam *et al.* [78]	Cu/CuO	Hexagonal	Water	130	0.5 × 0.5	1.75	50	80	100	32.5
Nam *et al.* [78]	Cu/CuO	Hexagonal	Water	160	0.5 × 0.5	1.75	50	90	100	40
Nam *et al.* [78]	Cu/CuO	Hexagonal	Water	190	0.5 × 0.5	1.75	50	100	100	47.5
Ravi *et al.* [80]	Si	Cylindrical	Water	–	0.5 × 1	2	15	45	100	~11
Ravi *et al.* [80]	Si	Cylindrical	Water	–	0.5 × 1	2	15	45	150	~19
Ravi *et al.* [80]	Si	Cylindrical	Water	–	0.5 × 1	2	15	65	100	~9
Hornor *et al.* [81]	Si	Cylindrical	Water	–	0.5 × 1	1	33	100	100	97.4
Hornor *et al.* [81]	Si	Cylindrical	Water	–	0.5 × 1	2	34	100	100	45.2
Hornor *et al.* [81]	Si	Cylindrical	Water	–	0.5 × 1	3	37	100	100	27.9
Hornor *et al.* [81]	Si	Cylindrical	Water	–	0.5 × 1	4	39	100	100	19.5

Table 4: Summary of literature on thermal performance of biporous evaporator wicks

Literature	Wick Material	Working Fluid	Wick Size(cm^2)	Heater (cm^2)	Small pore (µm)	Large pore (µm)	Wick thickness(µm)	Performance
Cai *et al.* [21]	CNT pillar	Water	1 × 1	0.2×0.2	300	–	210 – 300	q''= 510 W/cm^2
Cai *et al.* [21]	CNT stripe	Water	1 × 1	0.2×0.2	50	100	210 – 300	q''= 700 W/cm^2
Cai *et al.* [21]	CNT zigzag	Water	1 × 1	0.2×0.2	–	–	210 – 300	q''= 186 W/cm^2

Semenic *et al.* [22]	Sintered Cu	Water	4.01	0.322	63	455	3000	q''= 990 W/cm^2 (Superheat 147K)
Semenic *et al.* [22]	Sintered Cu	Water	4.01	0.322	63	455	2000	q''= 589 W/cm^2 (Superheat 100K)
Semenic *et al.* [22]	Sintered Cu	Water	4.01	0.322	83	892	3000	q''= 236 W/cm^2 (Superheat 41K)
Semenic *et al.* [22]	Sintered Cu	Water	4.01	0.322	83	586	2000	q''= 232 W/cm^2 (Superheat 38K)
Coso *et al.* [60]	Square Si pillar + microchannel	Water	2 × 2	1×1	*d*=13.5, *l*=30, *h*=207	31	–	q''= 52 W/cm^2 (evaporation regime)
Coso *et al.* [60]	Square Si pillar + microchannel	Water	1.9 × 2	1×1	*d*=7.1, *l*=16.1, *h*=149	30	–	q''= 119.6 ± 4.2 W/cm^2
Coso *et al.* [60]	Square Si pillar + microchannel	Water	1 × 1.5	1×1	*d*=7.1, *l*=16.1, *h*=149	30	–	q''= 73.6 ± 2.6 W/cm^2
Coso *et al.* [60]	Square Si pillar + microchannel	Water	1 × 1.1	0.25×0.25	*d*=7.1, *l*=16.1, *h*=149	30	–	q''= 160 W/cm^2 (evaporation regime)
Cao *et al.* [82]	Sintered Cu	Water	–	–	80	400	–	q''= 85 W/cm^2
Cao *et al.* [82]	Sintered Cu	Water	–	–	80	800	–	q''= 71 W/cm^2
Cao *et al.* [82]	Sintered Cu	Water	–	–	80	200	–	q''= 53 W/cm^2
Semenic *et al.* [83]	Sintered Cu	DI water	25.52	0.709	60	600	4000	q''=494 W/cm^2 (Superheat 128K)
Semenic *et al.* [83]	Sintered Cu	DI water	25.52	0.709	60	300	4000	q''=202 W/cm^2 (Superheat 81K)
Semenic *et al.* [83]	Sintered Cu	DI water	25.52	0.709	40	600	1000	q''=160 W/cm^2 (Superheat 18K)
Semenic *et al.* [83]	Sintered Cu	DI water	25.52	0.709	60	300	1000	q''=150 W/cm^2 (Superheat 32.5K)
Semenic *et al.* [83]	Sintered Cu	DI water	25.52	0.709	40	300	1000	q''=236.5 W/cm^2 (Superheat 45K)
Semenic *et al.* [84]	Sintered Cu	–	–	–	58 – 81	302 – 892	–	Thermal conductivity $k = 56.54(\frac{d}{D})^{0.823}$
Reily *et al.* [85]	Sintered Cu biporous+ monoporous	Water	–	–	60	300	920	q''=336 W/cm^2 (Superheat 49K)

Yeh *et al.* [88]	Sintered Ni	Ammonia	–	19.48	–	–	–	Q = 570W h=6.4 W/cm^{2}K
Liu *et al.* [90]	Sintered Cu+Ni	Methanol	–	9.62	–	–	–	q''= 168 W/cm^2 (Superheat 85K)
Cai *et al.* [94]	CNT	Water	1 × 1	0.2×0.2	50	100	250	q''= 600 W/cm^2
Byon *et al.* [95]	Si pillar groove type	Methanol	1 × 3	–	60	120	100	K/R_{eff}=0.936(μm)
Byon *et al.* [95]	Si pillar groove type	Methanol	1 × 3	–	60	210	100	Not converged
Byon *et al.* [95]	Si pillar square array	Methanol	1 × 3	–	60	120	100	K/R_{eff} =0.897(μm)
Byon *et al.* [95]	Si pillar square array	Methanol	1 × 3	–	60	210	100	K/R_{eff} =0.914(μm)
Byon *et al.* [95]	Si pillar square array	Methanol	1 × 3	–	60	300	100	Not converged
Byon *et al.* [95]	Si pillar diamond array	Methanol	1 × 3	–	60	200	100	Not converged
Byon *et al.* [95]	Si pillar staggered array	Methanol	1 × 3	–	60	210	100	K/R_{eff} =0.875(μm)
Byon *et al.* [95]	Si pillar pseudo groove	Methanol	1 ×3	–	60	60	100	K/R_{eff} =0.863(μm)
Ravi *et al.* [96]	Segmented in plane Si pillar	Water	1 × 2 – 4.5	0.5 × 1	d=10, l=20, h=100	d=42, l=100, h=100	–	Q = 14.5 W
Ravi *et al.* [96]	Segmented in plane Si pillar	Water	1 × 2 – 4.5	0.5 × 1	d=10, l=20, h=100	d=42, l=130, h=100	–	Q = 12.5 W
Ravi *et al.* [96]	Si micropillar + mesh	Water	1 × 2 – 4.5	0.5 × 1	4	d=42, l=100, h=100	–	Q = 5.5 W
Ravi *et al.* [96]	Si micropillar + mesh	Water	1 × 2 – 4.5	0.5 × 1	5	d=42, l=108, h=100	–	Q=3.5 W
Chen *et al.* [100]	Sintered Ni	Ammonia	–	14.52	2.6 – 53	335	15000	q''= 12.8 W/cm^2

1.5.Scope of the Thesis

In *Chapter 1*, a general overview of available cooling techniques was presented. A brief introduction on vapor chamber working mechanism and categories was also made. As the most significant part of a vapor chamber, evaporators with various types, uniform and biporous structures, were reviewed and compared.

In *Chapter 2*, the theoretical modeling that predicts the dryout heat flux of uniform cylindrical micropillar evaporators, biporous evaporators with micropillar arrays separated by microchannels and vapor chambers will be constructed.

In *Chapter 3*, detailed design and Micro-Electro-Mechanical-Systems (MEMS) fabrication process of evaporators and sealed Si vapor chambers will be provided. After that, the thermal characterization setup and calibration processes will be discussed, followed by the uncertainty analysis in the experimental measurements in *Chapter 4*.

In *Chapter 5*, the wettability, liquid propagation, model validation and parametric studies based on thermal characterization tests will be presented and explained in detail. Parametric studies include the effect of micropillar d/l ratio, height h on the uniform evaporator dryout heat flux and heat transfer coefficient, as well as the effect of micropillar array size and microchannel width on the evaporator and Si vapor chamber's heat dissipation capabilities. Optimization on the micropillar geometries with temperature rise constrains will be conducted in *Matlab*.

In *Chapter 6*, the wettability performance of micropillar surfaces at very high temperature above the saturation point will be characterized and discussed. The lifetime of droplets will be measured on micropillar surface with various geometries. Effect of micropillar geometry on the transition of droplet wetting regimes will be studied systematically.

In *Chapter 7,* conclusions will be drawn and recommendations on future work will be made.

Chapter 2: Analytical Modeling

2.1. Uniform Evaporator Modeling

Schematic illustration of uniform cylindrical Si micropillar evaporator is shown in *Figure 8*. The uniform micropillar evaporator is composed of uniformly and periodically distributed cylindrical micropillars with diameter d, pitch (center-to-center) distance l, and height h. The total size of the evaporator is denoted as $L \times L$ with a wicking distance of L as shown in *Figure 8(a)*.According to *Figure 8(b)*, the liquid is drawn from liquid reservoir/vapor chamber condenser to the micropillar arrays by a capillary effect with velocity u, where 1D liquid propagation was assumed.

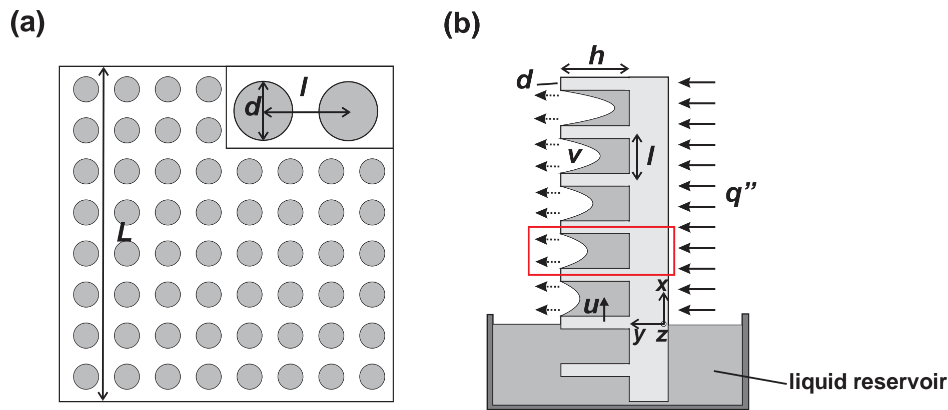

Figure 8: Schematic illustration of uniform micropillar based evaporator (a) Top view of the micropillar evaporator: The uniform evaporator is composed of uniformly distributed cylindrical micropillars with diameter d, pitch l, height h and wicking distance L (b) Cross-sectional view: Liquid reservoir, which mimics the condenser/adiabatic regions of vapor chamber, supplies liquid to compensate the liquid loss through evaporation in micropillar arrays. The liquid propagates in micropillar arrays with velocity u due to capillary pumping effect. Uniform heat flux q'' is applied on the back of the evaporator to induce uniform evaporation on the front side. The evaporation is assumed to be uniform with velocity v

The evaporator is subject to uniform heat flux q'' on the backside, which simulates heat generation of electronic devices. Due to the heating on the backside, evaporation of liquid in between of the micropillars is induced. A uniform evaporation rate v is assumed. All the liquid drawn from the liquid reservoir is assumed to be used for evaporation, thus the system is at steady-state condition.

As all the liquid supplied from liquid reservoir is consumed by evaporation,

$$Q = \dot{m} h_{fg} \tag{1}$$

where Q is the heat load applied to the evaporator and $\dot{m}$ stands for the mass flow rate of liquid, while h_{fg} is the latent heat. With uniform evaporation assumption, *Equation (1)* can be written as:

$$q^{"} = \rho_l h_{fg} v \tag{2}$$

where ρ_l stands for the density of working fluid. The governing continuity equation can be expressed as:

$$-\int_0^h du dy = v dx = \frac{q^{"}}{\rho_l h_{fg}} dx \tag{3}$$

Brinkman equation is used for momentum conservation. Brinkman's equation is an extension form of Darcy's law with an extra viscosity term, and it governs the flow of fluid in porous media. By neglecting the pressure variation in y direction ($dP/dy = 0$), the function can be expressed as:

$$\frac{\partial^2 u}{\partial y^2} = \frac{\varepsilon}{\mu}\frac{\partial P}{\partial x} + \frac{\varepsilon u}{K} \tag{4}$$

where P is the pressure developed in micropillar arrays, ε is the porosity of micropillar wick and $\varepsilon = 1 - (\pi d^2 / 4l^2)$. K represents the permeability of micropillar structures and μ is the viscosity of the fluid. *Equation (4)* can be expressed as $\ddot{u} = au + b$, where $a = \varepsilon / K$ and $b = (\varepsilon / \mu)(\partial P / \partial x)$. The following boundary conditions can be used to solve *Equation (4):*

(1) No-slip boundary condition at the bottom wall of micropillars: $u|_{y=0} = 0$

(2) No-shear condition at the interface of liquid/vapor: $\frac{du}{dy}|_{y=h} = 0$

Equation (4) can be solved and the solution of velocity is:

$$u = \frac{be^{\sqrt{ah}}}{ae^{\sqrt{ay}}(e^{\sqrt{ah}} + \frac{1}{e^{\sqrt{ah}}})} + \frac{be^{\sqrt{ay}}}{ae^{\sqrt{ah}}(e^{\sqrt{ah}} + \frac{1}{e^{\sqrt{ah}}})} - \frac{b}{a} \tag{5}$$

Therefore, the 1st order differentiation of velocity is:

$$du = \left(\frac{e^{\sqrt{a}h}}{ae^{\sqrt{a}y}(e^{\sqrt{a}h} + \frac{1}{e^{\sqrt{a}h}})} + \frac{e^{\sqrt{a}y}}{ae^{\sqrt{a}h}(e^{\sqrt{a}h} + \frac{1}{e^{\sqrt{a}h}})} - \frac{1}{a}\right)db \quad (6)$$

where b is defined as $b = \frac{\varepsilon}{\mu}\frac{\partial P}{\partial x}$, so

$$\frac{db}{dx} = \frac{\varepsilon}{\mu}\frac{\partial^2 P}{\partial x^2}dx \quad (7)$$

Substitute *Equation (7)* into *Equation (6)*, it can be obtained that:

$$du = \left(\frac{e^{\sqrt{a}h}}{ae^{\sqrt{a}y}(e^{\sqrt{a}h} + \frac{1}{e^{\sqrt{a}h}})} + \frac{e^{\sqrt{a}y}}{ae^{\sqrt{a}h}(e^{\sqrt{a}h} + \frac{1}{e^{\sqrt{a}h}})} - \frac{1}{a}\right)\frac{\varepsilon}{\mu}\frac{\partial^2 P}{\partial x^2}dx \quad (8)$$

The following expression can be obtained by rearranging *Equation (8)*:

$$du = \left[\frac{1}{a(e^{\sqrt{a}h} + \frac{1}{e^{\sqrt{a}h}})}(e^{\sqrt{a}(h-y)} + e^{\sqrt{a}(y-h)}) - \frac{1}{a}\right]\frac{\varepsilon}{\mu}\frac{\partial^2 P}{\partial x^2}dx \quad (9)$$

By substituting *Equation (9)* into *Equation (3), Equation (3)* can be written as:

$$-\int_0^h du dy = -\int_0^h \left[\frac{1}{a(e^{\sqrt{a}h} + \frac{1}{e^{\sqrt{a}h}})}(e^{\sqrt{a}(h-y)} + e^{\sqrt{a}(y-h)}) - \frac{1}{a}\right]\frac{\varepsilon}{\mu}\frac{\partial^2 P}{\partial x^2}dxdy = \frac{q''}{\rho_l h_{fg}}dx \quad (10)$$

By integrating the left-hand side of *Equation (10)*, we can get the following expression:

$$\left[-\frac{(e^{2\sqrt{a}h} - 1)}{a^{3/2}(e^{2\sqrt{a}h} + 1)} + \frac{h}{a}\right]\frac{\varepsilon}{\mu}\frac{\partial^2 P}{\partial x^2} = \frac{q''}{\rho_l h_{fg}} \quad (11)$$

At steady-state condition, the pressure is a function of x only, which is caused by liquid meniscus. A parabolic pressure profile with $P = Ax^2 + Bx + C$ is assumed. The pressure at $x = 0$ equals to 0 while that at $x = L$ equals to – P_{cap}, where P_{cap} is the maximum capillary pressure of the micropillar wick. And the expression of pressure profile is:

$$P = -\frac{2P_{cap}}{L}x + \frac{P_{cap}}{L^2}x^2 \quad (12)$$

By substituting *Equation (12)* into *Equation (11)*, the following equation can be obtained:

$$\left[-\frac{(e^{2\sqrt{ah}}-1)}{a^{3/2}(e^{2\sqrt{ah}}+1)}+\frac{h}{a}\right]\frac{\varepsilon}{\mu}\frac{\partial^2 P}{\partial x^2}=\left[-\frac{(e^{2\sqrt{ah}}-1)}{a^{3/2}(e^{2\sqrt{ah}}+1)}+\frac{h}{a}\right]\frac{\varepsilon}{\mu}\frac{2P_{cap}}{L^2}=\frac{q"}{\rho_l h_{fg}} \qquad (13)$$

Rearranging *Equation (13)* with $a=\varepsilon/K$, the capillary limited dryout heat flux of uniform cylindrical micropillar based evaporators can be expressed as:

$$\mathrm{q}"=\frac{2P_{cap}\rho_l h_{fg}hK}{\mu L^2}\left[1-\frac{\tanh(\sqrt{\frac{\varepsilon}{K}}h)}{\sqrt{\frac{\varepsilon}{K}}h}\right] \qquad (14)$$

As discussed by Hale *et al.* [72] and Ravi *et al*. [80], the capillary pressure model developed by Xiao *et al.* [70] provided a relatively accurate solution of capillary pressure in micropillar arrays. This was validated against both simulation and experimental results. Thus, the capillary pressure model of Xiao *et al.* [70] will be adopted in this thesis to correlate the capillary-limited dryout heat flux *q''* with the micropillar geometries. With energy minimization approach, the capillary pressure was defined as the surface energy change ΔE per unit volume of liquid ΔV that fills one micropillar unit cell:

$$P_{cap}=\frac{\Delta E}{\Delta V}=\frac{\sigma rf\cos\theta\pi dh+\sigma\cos\theta A_p-\sigma A_m}{\Delta V} \qquad (15)$$

where σ is the surface tension, θ stands for contact angle and *rf* is the roughness factor that accounts for the rough micropillar sidewalls with scallop structures. The scalloped structures were created in deep reactive ion etching (DRIE) process of MEMS fabrication. A semispherical shape of the sidewall is assumed and $rf=\pi/2$. The first 2 terms in *Equation (15)* energy change due to the wetting of micropillar sidewalls, while the third term stands for energy change due to meniscus formation. *Equation (15)* provides an average estimation of capillary pressure in micropillar arrays and it holds accurately for $h/l > 1$. Only with geometric ratio $h/l > 1$, the time taken for liquid to wet the sidewall of micropillars and to propagation from one unit cell to the bottom of next cell are comparable, and the average approach is accurate.

A_p and A_m are the project and actual liquid meniscus areas, respectively. Expressions of A_p and A_m were obtained by simulating the actual liquid meniscus shapes at different

micropillar geometries with Surface Evolver and curve fitted to obtain the correlation. A_p, A_m and ΔV were micropillar geometry dependent parameters, and

$$A_p = l^2 - \frac{1}{4}\pi d^2 \tag{16}$$

$$\begin{aligned} A_m = [&0.43 + 0.73 rf\cos\theta + 3.76(\frac{d}{l}) \\ &-0.046(rf\cos\theta)^2 - 5.53(rf\cos\theta)(\frac{d}{l}) - 4.05(\frac{d}{l})^2 \\ &-0.124(rf\cos\theta)^3 + 1.77(rf\cos\theta)^2(\frac{d}{l}) + 4.66(rf\cos\theta)(\frac{d}{l})^2] \times (l^2 - \frac{\pi d^2}{4}) \end{aligned} \tag{17}$$

$$\begin{aligned} \Delta V = hA_p - [&-0.175 - 0.345 rf\cos\theta + 4.07(\frac{d}{l}) \\ &+0.924(rf\cos\theta)^2 - 5.83(rf\cos\theta)(\frac{d}{l}) - 2.80(\frac{d}{l})^2 \\ &-0.439(rf\cos\theta)^3 + 2.41(rf\cos\theta)^2(\frac{d}{l}) + 2.71(rf\cos\theta)(\frac{d}{l})] \times A_p(l-d) \end{aligned} \tag{18}$$

Permeability K in *Equation (14)* can be calculated based on the micropillar geometries by using the permeability model developed by Byon *et al.* [74]. The permeability model of Byon *et al.* [74] took the effect of meniscus shape into account, and was proven to accurately predict the permeability with error less than 5%. This model was constructed based on the permeability model of Sangani *et al.* [61]. According to Sangani and Acrivos [61], the permeability of squarely packed cylindrical micropillars with $d/l < 0.57$ can be expressed as:

$$K_{2D} = l^2 \frac{\ln c^{-1/2} - 0.738 + c - 0.887c^2 + 2.038c^3 + o(c4)}{4\pi} \tag{19}$$

where c is the solid fraction of micropillar arrays and $c = 1 - \varepsilon$. The permeability model developed by Byon *et al.* [74] is

$$K = A_1 A_2 K_{2D} \left[1 - \frac{\exp(2\sqrt{\frac{\varepsilon}{K_{2D}}} h_{eff}) - 1}{\sqrt{\frac{\varepsilon}{K_{2D}}} h_{eff} (\exp(2\sqrt{\frac{\varepsilon}{K_{2D}}} h_{eff}) + 1)} \right] \tag{20}$$

where correction factors $A_1 = [h_{eff} + \frac{\varepsilon d}{4(1-\varepsilon)}]/[h + \frac{\varepsilon d}{4(1-\varepsilon)}]$ and $A_2 = h_{eff} / h$ are added to account for the variation of wetted area and channel cross-sectional area. The effective height h_{eff}, which is defined as the actual height of liquid meniscus, was obtained by correlating the meniscus geometry to micropillar geometries through the simulation in Surface Evolver. The fitted correlation is:

$$\begin{aligned} h_{eff} &= h - d[0.01476 + 0.85009\cos\theta + 0.215\frac{d}{l} + 0.18979(\cos\theta)^2 \\ &-3.46929(\frac{d}{l})(\cos\theta) - 0.28868(\frac{d}{l})^2 + 1.05357(\frac{d}{l})(\cos\theta)^2 \\ &+3.12583(\cos\theta)(\frac{d}{l})^2 - 1.4243(\frac{d}{l})^2(\cos\theta)^2] \end{aligned} \tag{21}$$

The capillary limited dryout heat flux of uniform micropillar evaporators can be calculated by substituting *Equation (15) – Equation (21)* into *Equation (14)*. Based on the expressions of *Equation (14) – Equation (21)*, it can be observed that the dryout heat flux *q''* depends on the thermophysical properties of the working fluid and the surface properties of the micropillar material, which are governed by ρ_l, h_{fg}, μ, θ and σ. Once a certain working fluid and micropillar material are chosen, for example water as working fluid and Si as the micropillar material as in this thesis, *q''* is determined by the geometries (d, h and l) of micropillars. Heat flux *q''* can be correlated to the temperature rise of the evaporator, also known as superheat ΔT, by the conduction equation and:

$$q'' = k_{eff}\frac{\Delta T}{h} \tag{22}$$

where ΔT is defined as the temperature difference between sample and saturation ambient. k_{eff} is the effective thermal conductivity of the micropillar wick. Expression of k_{eff} can be obtained by simulation in *Comsol* and curve fitting of the simulation result with micropillar geometries. Area in the red box as shown in *Figure 8(b)* was taken as the unit cell in *Comsol*, which contained half of the micropillar and half of the liquid film in between of two adjacent micropillars. Uniform heat flux condition was applied at the bottom of the evaporator, symmetric boundary conditions were applied at the sides of the micropillar and liquid film, while free convection condition was applied at the top of

micropillars. A flat liquid meniscus was assumed for simplification purpose. k_{eff} can be calculated based on the simulation results of temperatures at the bottom and top of the micropillars. For Si micropillars with water as working fluid, k_{eff} was found to correlate to the micropillar geometries by the following equation:

$$k_{eff} = 6.02633(\frac{d}{l})^2 - 3.19508\frac{d}{l} + 2.12324 \tag{23}$$

2.2. Vapor Chamber with Uniform Evaporator Modeling

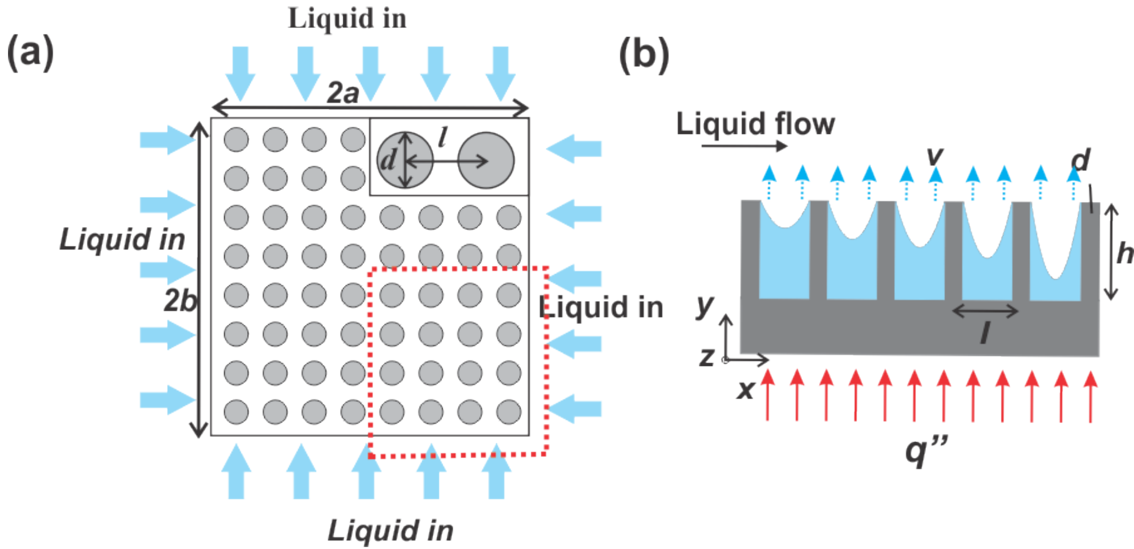

Figure 9: Schematic illustration of uniform micropillar based evaporator in a vapor chamber (a) Top view: the evaporator has a size of 2a×2b with micropillar diameter d, pitch l and height h. Fluid flows from the edges of the evaporator to the center and is driven by the meniscus curvature variation from the edge to the center. (b) Cross-sectional view: uniform heat flux q'' is applied from the back of the evaporator. Evaporation occurs at the liquid/vapor interface with uniform velocity v.

An evaporator inside a vapor chamber is surrounded by adiabatic regions that supply liquid from four sides of the evaporator, as shown in *Figure 9(a)*. Unlike the 1D evaporator case discussed in *2.1.,* where liquid propagates from the reservoir to the micropillar arrays in one direction only, the evaporator in the vapor chamber has liquid propagation from the outer edge of the evaporator to the center, driven by the meniscus curvature difference at various locations. Size of the evaporator is $2a \times 2b$. Uniform heat

flux is applied under the evaporator as presented in *Figure 9(b)*, this induces the evaporation at the liquid/vapor interface. The evaporation rate is defined as v and is assumed to be uniform at various locations. Wang and Peterson [101] solved the 2D Darcy's law to evaluate the maximum heat flux in a uniformly heated thin porous media, the maximum heat flux was expressed as [101]:

$$q" = \frac{\rho_l K h h_{fg} P_{cap}}{\mu} [\frac{a^2}{2} - \frac{2}{a} \sum_{m=1}^{m=\infty} \frac{\sin(\beta_m a)}{\beta_m{}^3 \cosh(\beta_m b)}]^{-1} \quad (24)$$

with $\beta_m = [(2m-1)\pi]/2a$, *Equation (24)* can be rewritten as:

$$q" = \frac{\rho_l K h h_{fg} P_{cap}}{\mu} [\frac{a^2}{2} - 16a^2 \sum_{m=1}^{m=\infty} \frac{\sin(\beta_m a)}{(2m-1)^3 \pi^3 \cosh(\beta_m b)}]^{-1} \quad (25)$$

For various evaporator width and length ratios *b/a*, the summation in *Equation (25)* can be calculated and the values are listed in *Table 5*.

Table 5: Values for the summation series in Equation (25) for different b/a ratios

b/a	$\sum_{m=1}^{m=\infty} \frac{\sin(\beta_m a)}{(2m-1)^3 \pi^3 \cosh(\beta_m b)}$
1	0.0128322
2	0.00278204
5	0.0000250403
10	9.72072×10^{-9}
100	3.89729×10^{-70}

From *Table 5*, it can be observed that for *b/a* >>1, the value of the summation series approaches 0, *Equation (25)* can be simplified into the following expression by neglecting the summation term:

$$q" = \frac{2\rho_l K h h_{fg} P_{cap}}{\mu \mathrm{a}^2} \quad (26)$$

Moreover, since the Brinkman's equation is an extension form of Darcy's law with an extra term to account for viscosity. The velocity profile solved by Darcy's law and Brinkman equation can be correlated with the following expression:

$$u_{Brinkman} = u_{Darcy}\left(1 - \frac{\tanh(\sqrt{\frac{\varepsilon}{K}}h)}{\sqrt{\frac{\varepsilon}{K}}h}\right) \tag{27}$$

Based on *Equation (27)*, Wang and Peterson's model [101] can be modified to obtain the solution of Brinkman's equation and

$$q" = \frac{2\rho_l K h h_{fg} P_{cap}}{\mu \mathrm{a}^2}\left(1 - \frac{\tanh(\sqrt{\frac{\varepsilon}{K}}h)}{\sqrt{\frac{\varepsilon}{K}}h}\right) \tag{28}$$

which is exactly the same solution as the case in *Equation (14).* Thus, for $b/a = 1$, where $b = a$, *Equation (25)* can be simplified based on *Table 5*:

$$\frac{a^2}{2} - 16a^2 \sum_{m=1}^{m=\infty} \frac{\sin(\beta_m a)}{(2m-1)^3 \pi^3 \cosh(\beta_m b)} = \frac{a^2}{2} \text{-} 16a^2 \times 0.00278204 \approx 0.3a^2 \tag{29}$$

By substituting *Equation (29)* and *Equation (27)* into *Equation (25),* the capillary limited dryout heat flux in a square evaporator with 2D liquid supply can be written as:

$$q" = \frac{3.33\rho_l K h h_{fg} P_{cap}}{\mu \mathrm{a}^2}\left(1 - \frac{\tanh(\sqrt{\frac{\varepsilon}{K}}h)}{\sqrt{\frac{\varepsilon}{K}}h}\right) \tag{30}$$

Besides the evaporators, the adiabatic region in the vapor chamber of the thesis is also composed of micropillars to transport liquid. The micropillars in the evaporator regions should be designed such that the heat dissipation capability should be maximized according to *Equation (30).* As the adiabatic region only serves the function of circulating liquid, the liquid transportation capability of adiabatic region should be optimized. The liquid propagation distance x is correlated to the micropillar geometries by Washburn's equation [102] as discussed in [59], where the gravity effect was neglected:

$$x^2 = \frac{K P_{cap}}{\varepsilon \mu} t \tag{31}$$

Therefore, the parameter $\sqrt{KP_{cap} / \varepsilon}$ needs to be maximized for optimal liquid supply in adiabatic region micropillars.

2.3. Biporous Evaporator Modeling

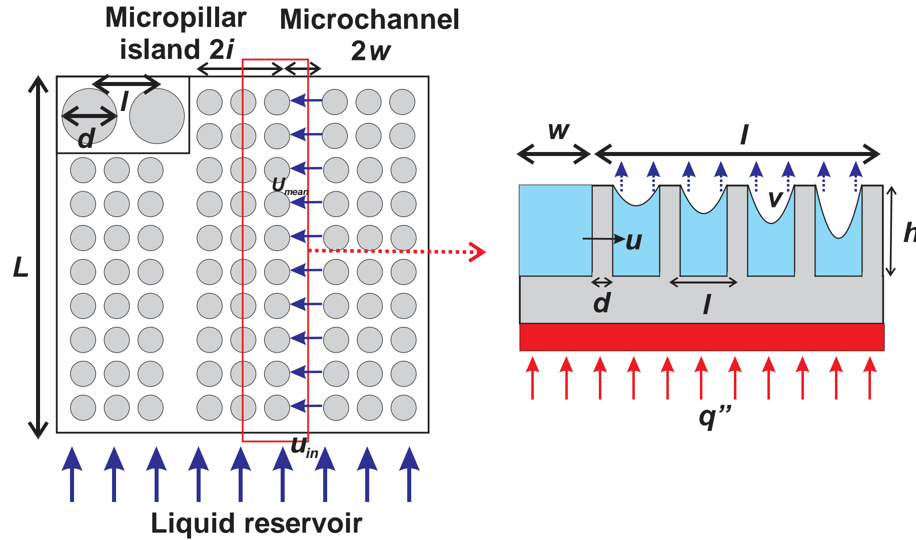

Figure 10: Schematic illustration of biporous evaporators (a) Top view: the biporous evaporator is composed of micropillar arrays, named as micropillar islands with width 2i, separated by microchannels with width 2w. The micropillar islands consist of cylindrical micropillars with diameter d, pitch l and height h. (b) Cross-sectional view of the unit cell in the red box: microchannels serve as local liquid reservoir to shorten the liquid propagation distance. The evaporator is subject to uniform heat flux q'' from the bottom. Evaporation and heat transfer in microchannels are neglected.

As discussed in *1.3.4*, biporous evaporator can be adopted to utilize the advantage of large permeability with large effective pore size structures, while at the same time the excellent capillary performance will not be sacrificed by using structures with small effective pore sizes. Therefore, biporous evaporators with micropillar arrays separated by microchannels will be modeled and discussed in this thesis. As shown in *Figure 10(a)*, the micropillar arrays are named as micropillar islands with width of $2i$, while the microchannel width is denoted as $2w$. The microchannels act as local liquid reservoir that can largely reduce the liquid propagation distance. According to *Figure 10(b)*, uniform heat flux q'' is applied at the backside of the biporous evaporator. Since during

evaporation, more than 80% heat was transferred in the thin film regions as discussed in [103 – 105], the heat transfer from the evaporation in microchannels is too small and can be neglected. For simplification purpose, the liquid meniscus curvature in the microchannels is also ignored. Based on these assumptions, *Equation (14)* can be modified to evaluate the dryout heat flux of biporous evaporators with microchannel structures:

$$q"=\frac{i}{i+w}\frac{2(P_{cap}-P_{la})\rho_l h_{fg} hK}{\mu i^2}\left[1-\frac{\tanh(\sqrt{\frac{\varepsilon}{K}}h)}{\sqrt{\frac{\varepsilon}{K}}h}\right] \tag{32}$$

where P_{la} stands for the pressure drop in microchannels. Liquid transportation inside microchannels is governed by the following equations:

(1) Navier-Stokes equation: $\rho_l u \cdot \nabla u = \mu \nabla^2 u - \nabla P$ (33)

(2) Continuity equation: $\nabla \cdot u = 0$ (34)

(3) Energy balance at evaporation interface: $q"_0 = \frac{\dot{m} h_{fg}}{iL} = \rho_l u_0 h_{fg} = \frac{\sigma \rho_l h_{fg}}{\mu}$ (35)

With the following scaling factors:

$$u_0 = \frac{\sigma}{\mu},\ P_0 = \frac{\sigma}{i}, \dot{m}_0 = \rho_l u_0 iL, \dot{V}_0 = \frac{\dot{m}_0}{\rho_l} = u_0 iL, u = u^* u_0, P = P^* P_0, x = x^* i, \dot{V} = \dot{V}^* \dot{V}_0$$

$$L = iL^*, w = iw^*, h = ih^*, K = l^2 K^*, P_{cap} = P_{cap}{}^* \frac{\sigma}{l}$$

We can have: $q" iL = \dot{m} h_{fg} = q"^* q"_0 iL$ and $q"^* = \frac{\dot{m} h_{fg}}{q"_0 iL} = \frac{\dot{m}\mu}{\sigma \rho_l iL} = \dot{m}^* \frac{i}{L}$

Equation (33) and *(34)* can be non-dimensionalized as:

$$\mathrm{Re}(u^* \cdot \nabla^* u^*) = \nabla^{*2} u^* - \nabla^* P^* \tag{36}$$

$$\nabla^* \cdot u^* = 0 \tag{37}$$

The mean flow velocity at the inlet of microchannels can be expressed as:

$$u_{in} = -\frac{i^2}{\mu}\frac{P_{la}}{L} f(\frac{w}{i}, \frac{h}{i}) \tag{38}$$

The volumetric flow rate of liquid scales to:

$$\dot{V}^* = \frac{i^4}{\mu}\frac{P_{la}}{Lu_0 i^2}\frac{w}{i}\frac{h}{i} f(\frac{w}{i}, \frac{h}{i}) \tag{39}$$

It can be derived that $\dot{V}^* = \dot{m}^*$, from *Equation (39)* we can get:

$$P_{la}^* = \frac{P_{la}}{P_0} = \frac{P_{la}}{\sigma / i} = \frac{\dot{m}^* \frac{L}{i}}{\frac{w}{i}\frac{h}{i} f(\frac{w}{i}, \frac{h}{i})} = \frac{q''^* (\frac{L}{i})^2}{\frac{w}{i}\frac{h}{i} f(\frac{w}{i}, \frac{h}{i})} = \frac{q''^* L^{*2}}{w^* h^* f(w^*, h^*)} \tag{40}$$

The non-dimensionalized form will be:

$$P_{la} = \frac{q'' L^2}{whf(\frac{w}{i}, \frac{h}{i})}\frac{\mu}{\rho_l h_{fg} i} \tag{41}$$

where $f(\frac{w}{i}, \frac{h}{i})$ is a geometric dependent coefficient and $f(\frac{w}{i}, \frac{h}{i})$ depends on the half micropillar island width *i,* half microchannel width *w* and micropillar height *h*. Values of $f(\frac{w}{i}, \frac{h}{i})$ can be obtained through simulation in *Comsol* and curve fitting of the simulation results. The simulation was conducted by applying non-slip condition at the channel bottom, no-shear condition at the top, symmetric condition at the sidewalls, inlet pressure equals to 0 and the liquid velocity at the outlet of the channel equals to mean velocity. Expression of $f(\frac{w}{i}, \frac{h}{i})$ is obtained to be

$$f(\frac{w}{i}, \frac{h}{i}) = [-2.3868\times10^{-4} + 4.8541\times10^{-2}\frac{h}{i} - 1.4325(\frac{h}{i})^2]\times\exp(-\frac{w/i}{0.11073 - 0.23438\frac{h}{i} + 4.57228(\frac{h}{i})^2})$$
$$+[-1.3911\times10^{-4} + 7.1494\times10^{-3}\frac{h}{i} + 0.8331(\frac{h}{i})^2] \tag{42}$$

The values of $f(\frac{w}{i},\frac{h}{i})$ calculated by *Equation (42)* are compared with the values of $f(\frac{w}{i},\frac{h}{i})$ simulated by *Comsol* in *Table 6*. The discrepancies between the simulated and calculated values are less than 1.14%, which is an indication of the accuracy of the curve fitting equation.

Table 6: Comparison between simulation and calculated values of f

w (μm)	**h (μm)**	**i (μm)**	***f* simulation**	***f* – curve fitting**	**Discrepancy**
21	10.5	210	0.001718	0.001738	1.14%
126	10.5	210	0.002287	0.002295	0.34%
84	14.7	210	0.004337	0.004318	0.43%
147	18.9	210	0.0072	0.007223	0.32%

By substituting *Equation (41)* and *(42)* into *Equation (32)* and rearrange, the capillary limited dryout heat flux of biporous evaporators with microchannel 2*w* and micropillar islands 2*i* can be expressed as:

$$q''=\frac{\frac{2\rho_l h_{fg} hK}{i\mu}\left[1-\frac{\tanh(\sqrt{\frac{\varepsilon}{K}}h)}{\sqrt{\frac{\varepsilon}{K}}h}\right]\frac{1}{i+w}P_{cap}}{1+\frac{2hK}{i^2}\left[1-\frac{\tanh(\sqrt{\frac{\varepsilon}{K}}h)}{\sqrt{\frac{\varepsilon}{K}}h}\right]\frac{1}{i+w}\frac{L^2}{whf(\frac{w}{i},\frac{h}{i})}} \tag{43}$$

where P_{cap} and K can be evaluated with *Equation (15) – (21).*

2.4. Summary

In this chapter, models that can predict the capillary limited dryout heat flux of uniform evaporator, actual vapor chamber with uniform evaporator and biporous evaporators were developed by solving Brinkman's equation.

The uniform evaporators are composed of uniformly distributed cylindrical micropillars that are packed squarely. Dryout heat flux of uniform evaporators was derived based on the Brinkman's equation with uniform evaporation assumption. All the liquid supplied from the reservoir was used for evaporation. From the expression of dryout heat flux, it can be observed that the dryout heat flux depends on the thermophysical properties of working fluid, surface tension, contact angle and micropillar geometries d, h, and l. With a certain working fluid and micropillar material, the dryout heat flux depends solely on micropillar geometries. To calculate the temperature rise of micropillar evaporator, the effective thermal conductivity of the wick was modeled using *Comsol* and was correlated to the micropillar geometries.

In actual vapor chamber with uniform micropillar evaporators, the liquid was transported from the outer edge of the evaporator to the center in a 2D manner. Wang and Peterson's [101] in predicting the capillary limited heat flux of 2D porous media based on Darcy's law was evaluated and extended. A Brinkman's solution was obtained for the 2D case to predict the dryout heat flux of a square uniform micropillar evaporator.

Finally, biporous evaporator with uniform micropillar arrays separated by microchannels was also modeled. The meniscus and heat transfer in the microchannels were ignored. Pressure drop inside the microchannels was analyzed and simulated in *Comsol*. The model developed for biporous evaporators can be used to predict the dryout heat flux which was limited by the capillary effect.

Chapter 3: Microfabrication

The micropillar evaporator samples and sealed silicon vapor chambers were manufactured using standard Micro-Electro-Mechanical Systems (MEMS) process. Photolithography was performed to transfer the structures on the chrome masks designed by *L-edit* to the Si wafers. Deep reactive ion etching (DRIE) was conducted to etch micropillars with desired height. The design and fabrication detail of uniform/biporous micropillar evaporators will be discussed in *3.1*, while the microfabrication process and structures of Si vapor chambers will be discussed in *3.2*.

3.1. Evaporator

3.1.1. Evaporator Design

The photomask used in photolithography was designed with *L-edit* (*Tanner Research Inc.*) and is shown in *Figure 11(a)*. The photomask is used for 6-inch Si wafers and contains several pieces of evaporator samples. Each evaporator sample has a width of 2 cm and length of 1.7 cm. The total micropillar area is 1 cm× 1.5 cm, while 1 cm × 1 cm of which is sued for evaporation. 0.5 cm extra spaces on the left and right edges of the sample were left for sample nomenclature and handling purpose. The name of each sample with information of micropillar diameter d and pitch l is defined on the side of each sample. While a rectangular scale bar is designed on the other edge of the sample for alignment convenience during tests. The evaporator wicks have various designs with uniformly distributed micropillars and biporous structures that have microchannels to separate the micropillar arrays. Detail of the evaporator wick design are shown in *Figure 11(b)*. The backside of the evaporator sample has 1 heater and 4 resistance-temperature-detectors (RTDs), this is to simulate the heat generation of electronic components and simultaneously measure the temperature of the evaporator samples by RTDs. Pattern design on the evaporator backside is shown in *Figure 11(c)*. The heater is composed of zig-zag patterned 590 μm wide wires that cover a total area of 1 cm × 1 cm, as shown in *Figure 11(d)*. 4 RTDs locate at the center of the sample are used for local temperature measurement. According to *Figure 11(e)*, the RTDs contain zig-zag patterns of 25 μm thin wires that span over a total area of 2.24 mm × 0.525 mm and connect to 2 contact

pads for electrical connection. The thickness of the metal film for all the heater and RTD wires will be the same, which will be defined by the metal deposition process that will be discussed in detail in the following section.

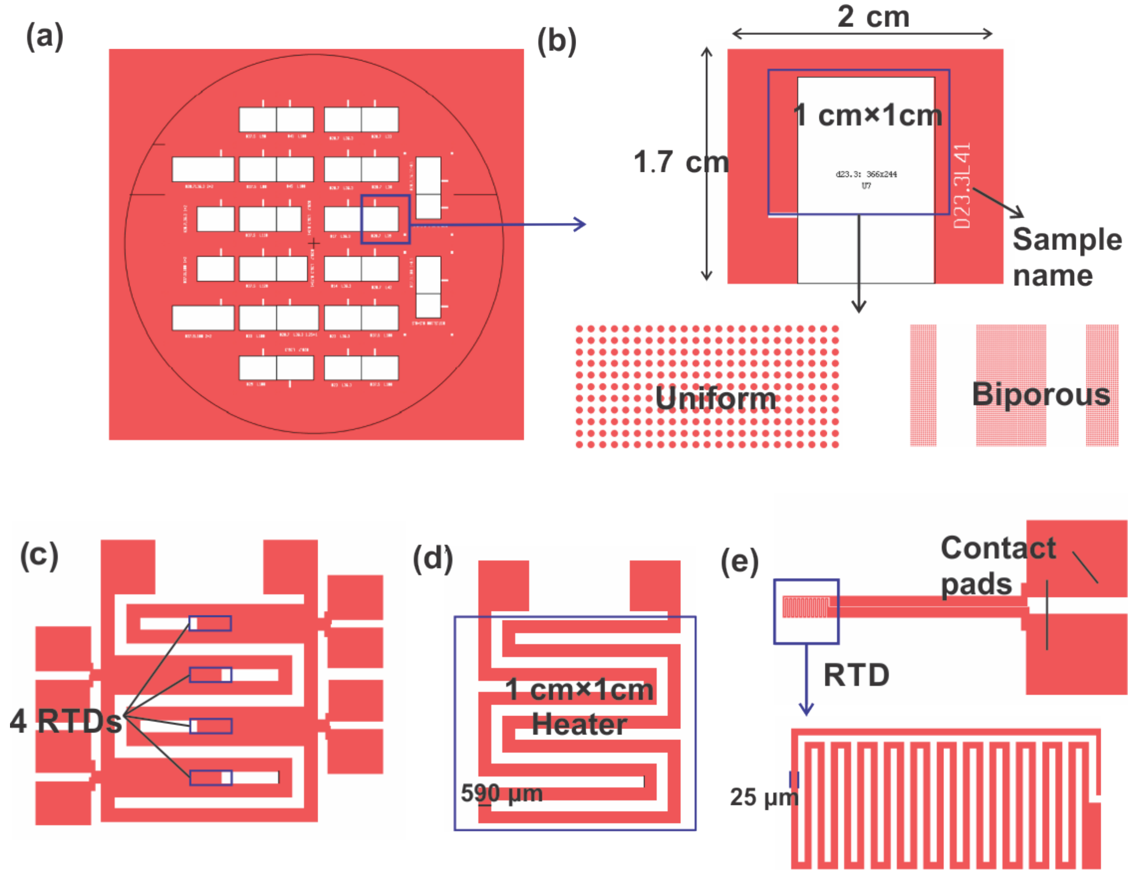

Figure 11: Photomask design for evaporator samples (a) Chrome mask for 6 inch Si wafers contains several pieces of evaporator samples (b) Closer look of evaporator sample with total size of 1.7 cm × 2 cm and total micropillar area of 1.5 cm × 1 cm , out of which 1 cm × 1 cm is used for evaporation (c) Design of heater and 4 resistance-temperature-detectors (RTDs) (d) The heater has a zig-zag pattern of 590 μm wires spans over an area of 1 cm × 1 cm (e) RTD has 25 μm zig-zag wires span over an area of 2.24 mm × 0.525 mm

3.1.2. Evaporator Microfabrication

6 inch double polished Si wafers were used to fabricate micropillar based uniform/biporous evaporators. Detailed fabrication processes are illustrated in *Figure 12*. Prior to microfabrication, the new Si wafers were cleaned with hot piranha solution.

Piranha solution is a mixture of sulfuric acid (H_2SO_4) and hydrogen peroxide (H_2O_2), which was used to remove any organic contaminants and residues on the wafer surface. After that, the wafers undergo 6 cycles DI water cleaning, followed by 5 s dipping in 10:1 hydrofluoric acid to remove native oxide. After the cleaning was done, the thermal oxide was grown on both sides of the double polished Si wafer. With 4 hrs wet oxidation in the furnace (*MRL A4 furnace*), dense and smooth thermal oxide with a thickness of 930 nm was grown, as shown in *Figure 12 (a), step 1*.

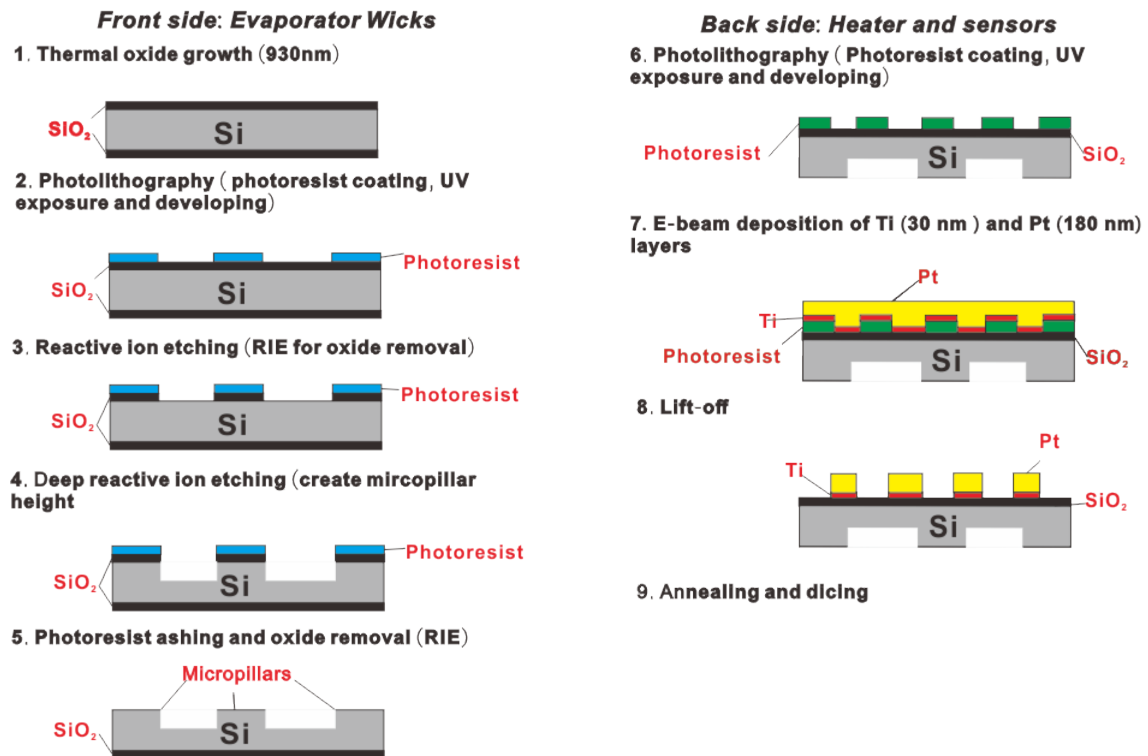

Figure 12: Fabrication process of evaporator sample front side with evaporator wicks

After the thermal oxide growth step, HDMS (hexamethyldisilizane) priming was conducted in the priming oven (*310TA Priming Oven*) at 150℃ to enhance the adhesion between photoresist and Si wafer. Then one side of the Si wafer was coated with 1.25 µm thick S1813 positive photoresist by the spin coater (*Suss RCD8 Photoresist Spin Coater*). After that, the wafers were soft baked at 125℃ for 4 mins on a hotplate (*Blue M oven*). Purpose of the soft bake was to evaporate the photoresist solvent and densify the photoresist layer. The customized chrome mask as shown in *Figure 11(a)* was then

mounted onto a mask aligner (*Karl Suss MA-6 Double Side Aligner*). The soft baked wafer was loaded onto the aligner, which undergo 7 s UV (ultra-violet) exposure to make the exposed area of the positive photoresist soluble in the developer. Developing was done manually with 2.67% TMAH (tetramethylammonium hydroxide) solution. After that the patterns on the wafer were examined under microscope to ensure a complete photoresist removal and excellent pattern shape. Then the wafer was cleaned by 6 cycles of DI (deionized) water rinse, followed by spin drying. These are the processes conducted in *Figure 12, step 2*. In *step 3* of *Figure 12*, reactive ion etching (RIE) was performed to remove undesired SiO_2 (*4520 Oxide Etcher*), so that the Si can be exposed and etched away in subsequent steps. Deep reactive ion etching (DRIE) or Bosch etching that can create highly anisotropic structures was performed according to *step 4*. DRIE is a cyclic process which involves the repeating cycles of plasma etching and passivation steps. Micropillars with desired height and scallop structure sidewalls were defined after this step. The remaining SiO_2 acted as hard masks on top of micropillars during DRIE. Then the photoresist and SiO_2, which covered the top of micropillars, were removed by plasma asher (*Tepla O_2 Plasma Asher*) and reactive ion etching (*4520 Oxide Etcher*), respectively, as shown in *Figure 12,step 5*. From *step 1* to *5* in *Figure 12*, the uniform/biporous evaporator wicks with micropillar arrays or microchannels were fabricated with desired height.

Once the fabrication of front side wick structures was done, the wafers were cleaned with acetone, IPA (isopropanol) and DI water, respectively. This was done by 10 mins immersion in each solution. The purpose of the cleaning was to remove any organic residues on the wafers to ensure good photoresist and metal adhesion in following steps. After that HDMS priming was performed again to ensure photoresist adhesion on the backside of the wafer. Then the wafer was attached to a plain and unprocessed Si wafer by high temperature Kapton tape that was pasted on the edges of the wafer. This was to protect the micropillar structures. The wafer was mounted on to the spin coater (*Suss RCD8 Photoresist Spin Coater*) and MaN 1440 negative photoresist was manually dispensed on the wafer, followed by 3000 rpm spin to distribute the photoresist evenly on the wafer surface. The negative photoresist was soft baked for 3 mins at 160℃. After

soft bake, the protective wafer and the processed wafer were separated. And the wafer with evaporator wicks was loaded onto the mask aligner (*Karl Suss MA-6 Double Side Aligner*) to perform photolithography, as shown in *Figure 12, step 6.* Prior to UV exposure, the front side and the mask was aligned by cross alignment marks to ensure the location of backside heater and RTDs. Then the wafer was irradiated by UV light for 20 s, followed by manual develop in photoresist developer for around 4 mins. The heater and RTD patterns were inspected under microscope to ensure complete photoresist removal, otherwise good metal adhesion cannot be guaranteed. The wafer was cleaned with DI water for 6 cycles and dried with spin dryer. The metal used for heater and RTDs was high purity Pt (platinum) with purity of 99.999%. This was because Pt thin film has excellent linear relationship between its resistance and temperature, and can be used as highly responsive temperature sensor. Deposition of metal films was done with electron-beam deposition technique (*Innotec E-beam Evaporator*) to ensure a continuous and smooth layer of metal film. 30 nm Ti (titanium) film was deposited on the backside of the wafer as an adhesion layer between the wafer and Pt, followed by 180 nm Pt film deposition as shown in *step 7*. The 930 nm thermal oxide grown in *step 1* was used as insulation layer between Si substrate and metal film to prevent electrical short circuit. After electron-beam deposition, lift-off process was conducted by immersing the wafer in acetone solution for prolonged time. This step was illustrated in *Figure 12, step 8,* the metal structures were remained on the wafer at areas without photoresist, while for the area with photoresist, the photoresist was dissolved by acetone and metal films were detached from the wafer. Microscope investigation was conducted to ensure throughout lift-off, so that the thin metal wires in between of the zig-zag patterns were completely removed. Next, the wafer was cleaned with IPA, DI water, followed by spin drying process. After that, the wafer was annealed at 400℃ for 2 hrs in the furnace. This was to stabilize the crystal structures of the metal and avoid shift of resistance readings, as discussed by Cai *et al.* [106]. Once *steps 1* to *9* were performed, the wafer was diced into small pieces with size of 1.7 cm $\times$ 2 cm.

3.1.3. Evaporator Samples

The SEM (scanning electron microscope) images of the micropillars fabricated for uniform evaporators are shown in *Figure 13(a)*. The uniform evaporator wicks have squarely packed cylindrical micropillars with diameter *d*, height *h*, and center-to-center distance *l*. Owing to the cyclic etching and passivation steps of DRIE in *Figure 12 (c)*, scallop structures can be observed on the sidewalls of micropillars. *Figure 13(b)* presented the pictures of evaporator sample front side with micropillar structures and backside with heater and 4 RTDs. Total wick area was 1.5 cm × 1 cm with 1 cm × 1 cm for evaporation. The extra space was left to account for a macroscopic meniscus that forms when the evaporator sample was inserted into the liquid reservoir vertically, as shown in *Figure 13(c)*.

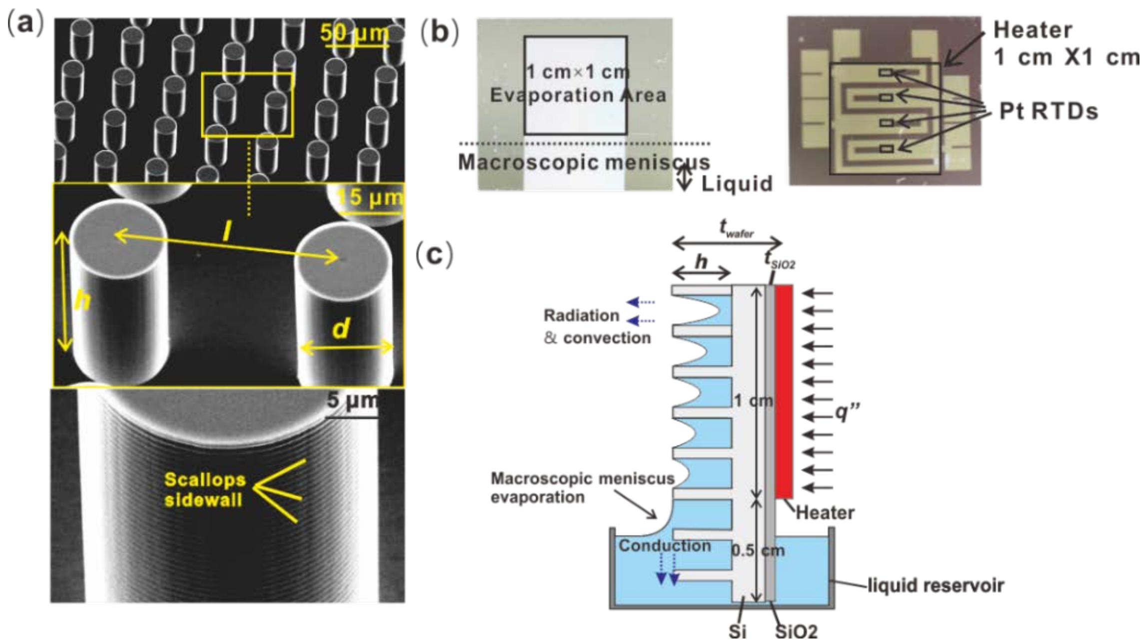

Figure 13: (a) SEM images of cylindrical micropillars with diameter d, height h, and pitch l. The micropillars have scallop sidewalls. (b) Images of front side and backside of uniform evaporator sample (c) Illustration of macroscopic meniscus

The height of the macroscopic meniscus can be calculated with the following equation as discussed by Nam *et al.* [59].

$$h_{macroscopic} = \sqrt{\frac{2\sigma}{\rho_l \, g}}(1-\sin\theta_a)^{1/2} \quad (44)$$

where g is gravitational constant, θ_a represents the apparent contact angle. The macroscopic meniscus was calculated to be around 0.27 cm for water. Therefore, 0.5 cm extra space was left at the bottom of the sample to allow for this macroscopic meniscus plus 0.23 cm immersion of the sample in the water. The zig-zag pattern Pt heater covered an area of 1 cm × 1 cm at the backside of the 1 cm × 1 cm evaporator wick, which was used to provide uniform Joule heating. The 4 RTDs were used for temperature measurement. There were total 10 contact pads for the 4 RTDs and 1 heater, which can be connected to power supply and data acquisition systems, as shown in *Figure 13(b)*.

Uniform evaporators with various micropillar geometries d, h and l were fabricated to conduct parametric studies. List of the sample numbers and corresponding geometric sizes are presented in *Table 7*. The geometric sizes shown in *Table 7* are the actual sizes for the micropillars. Actual sizes of the micropillars were measured using SEM. 10 readings were taken and averaged for each d, h and l values of each sample, respectively. Values in *Table 7* were the averaged results for the geometric sizes.

Table 7: List of uniform evaporator geometries. The d, h, and l values were actual geometric sizes measured by SEM

Sample Number	Measured ***d*** (µm)	Measured ***h*** (µm)	Measured ***l*** (µm)
1	23.4	39.5	41.0
2	25.9	39.5	41.0
3	28.2	39.5	41.0
4	22.1	39.5	41.0
5	23.4	39.5	36
6	23.4	39.5	34
7	23.4	39.5	44
8	23.2	79.7	41.0
9	22.9	84.5	41.0
10	14.7	25.7	25.8
11	17.9	31.9	32.1
12	3.4	8.9	6

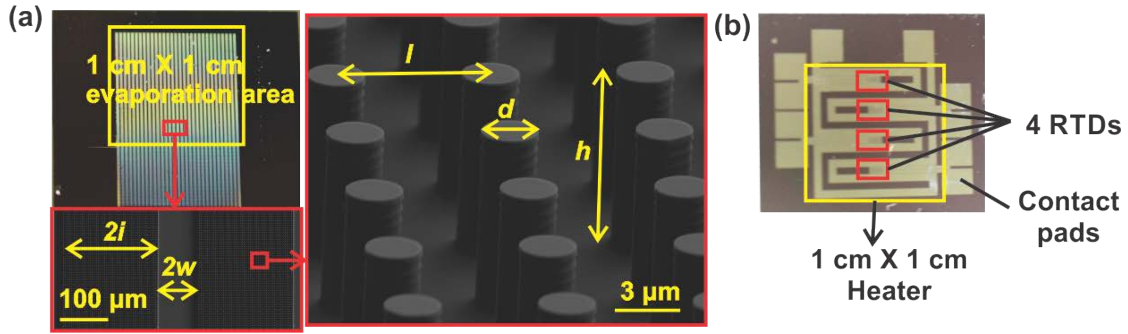

Figure 14: (a) Picture and SEM images of biporous evaporators with micropillar arrays separated by microchannels (b) Backside heater and RTDs of biporous evaporator sample

Images and SEM images of the biporous evaporators' front side and backside are shown in *Figure 14(a)* and *(b)*. Like the uniform evaporators in *Figure 13*, the biporous evaporators have a front side wick structure of 1.5 cm × 1 cm, out of which 1 cm × 1cm was used for evaporation and was uniformly heated by 1 cm × 1cm heater. Besides the micropillar arrays with periodically distributed cylindrical micropillars, the biporous evaporators also have microchannels with a width of 2*w* to act as local liquid arteries. The micropillar arrays were also named as micropillar island, and have a width of 2*i*. The biporous evaporator wicks have alternatively distributed microchannels and micropillar islands. Biporous evaporators with various micropillar island and microchannel widths were fabricated. The actual geometries of micropillars, islands, and microchannels for the biporous evaporators were measured with SEM, where 10 readings were taken and averaged for each parameter. The geometries are listed in *Table 8*.

Table 8: List of biporous evaporator geometries. The d, h, l, 2i and 2w values were actual geometric sizes measured by SEM

Sample number	*d* (µm)	*h* (µm)	*l* (µm)	2*i* (µm)	2*w* (µm)
1	3.4	8.9	6.0	120	117
2	3.4	8.9	6.0	202	117
3	3.4	8.9	6.0	240	117
4	3.4	8.9	6.0	280	117
5	3.4	8.9	6.0	202	60
6	3.4	8.9	6.0	202	90
7	3.4	8.9	6.0	202	150
8	3.4	8.1	6.0	207	120
9	3.4	8.9	7.0	202	117

3.2. Vapor Chamber

3.2.1. Vapor Chamber Design

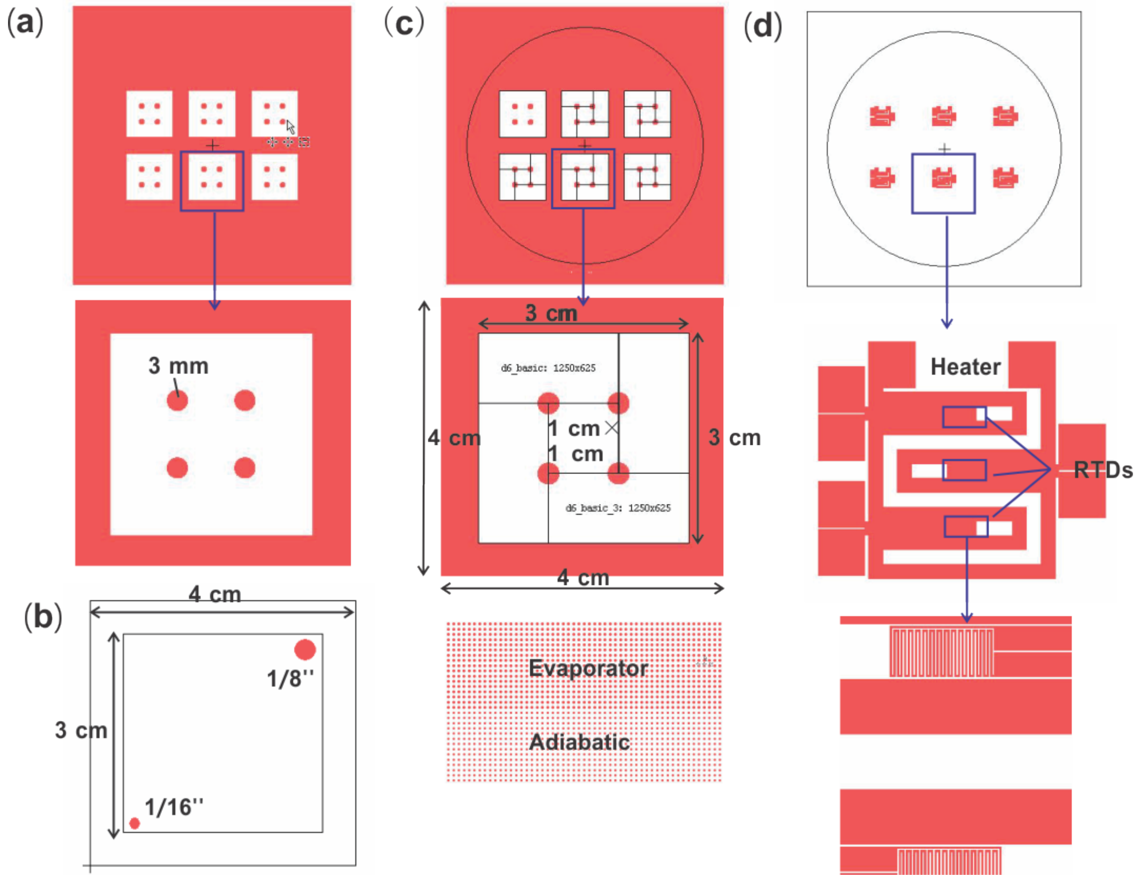

Figure 15: Mask designs for sealed Si vapor chambers (a) Backside of top wafer with cavity and supporting posts (b) Front side of top wafer with 1/8'' and 1/16'' holes (c) Front side of bottom wafer with micropillar structures (d) Back side of bottom wafer with RTDs and heater.

The mask designs for sealed Si vapor chambers are illustrated in *Figure 15*. The sealed Si vapor chamber is made by bonding 2 Si wafers together, thus total 4 chrome masks were designed for the 4 sides of 2 Si wafers. The top wafer of the Si vapor chamber has a cavity as vapor space and 2 holes for vapor chamber evacuation and liquid charging. As shown in *Figure 15(a)*, the backside of the top wafer has 4 circular supporting posts with a diameter of 3 mm. The total size of each Si vapor chamber is 4 cm × 4 cm, while the cavity size is 3 cm × 3 cm. The 0.5 cm extra space on each edge of the square vapor chamber are the bonding areas. There are 2 holes with 1/8'' diameter and 1/16'' diameter,

respectively as shown in *Figure 15(b).* A 1/16'' tube will be soldered to the 1/16'' hole for chamber evacuation purpose, while the 1/8'' hole will be connected to a 1/8'' tube for working fluid charging. The front side of the bottom wafer act as an evaporator and adiabatic regions as shown in *Figure 15(c)*, which circulates working fluid with micropillar structures. Total area with micropillar structures is 3 cm × 3 cm, while 1 cm × 1 cm area in the center serves the function of the evaporator. The 4 supporting posts locate at 4 corners of the evaporator. As discussed in *2.2*, the adiabatic region and evaporator region have micropillars with distinct geometries.

The backside of the bottom wafer has zig-zag patterns for heater and RTDs. Each heater has an area of 1 cm × 1 cm to provide uniform heating for the 1 cm × 1 cm evaporator. There are 3 RTDs on the backside of each vapor chamber, which is connected to 6 contact pads according to *Figure 15(d).* The RTDs has the same zig-zag patterns as that of the RTD on evaporator samples as shown in *Figure 11*.The RTDs act as local temperature sensors.

3.2.2. Vapor Chamber Microfabrication

Detailed fabrication processes of sealed Si vapor chamber are illustrated in *Figure 16.* Prior to the microfabrication, the plain Si wafer was cleaned with piranha solution to remove the organic contaminants on the wafer surface. After that, the wafer was cleaned with DI water followed by HDMS priming to reduce the moisture and enhance photoresist adhesion. Then 1.25 μm thick S1813 photoresist was spin coated (*Suss RCD8 Photoresist Spin Coater*) on one side of the Si wafer. After that, the wafer was soft baked at 125℃ for 4 mins to densify the photoresist. Then the wafer was loaded onto mask aligner (*Karl Suss MA-6 Double Side Aligner*) for photolithography, which was irradiated by UV light for 7 s. The pattern on the chrome mask as shown in *Figure 15(a)* was transferred onto the photoresist layer. The exposed area of the photoresist became soluble in photoresist developer. The photoresist develop was done manually with 2.67% TMAH solution for around 2 mins. Microscope inspection was then conducted to ensure excellent pattern transfer. The processes are the detailed procedure for *step 2* in *Figure 16.*

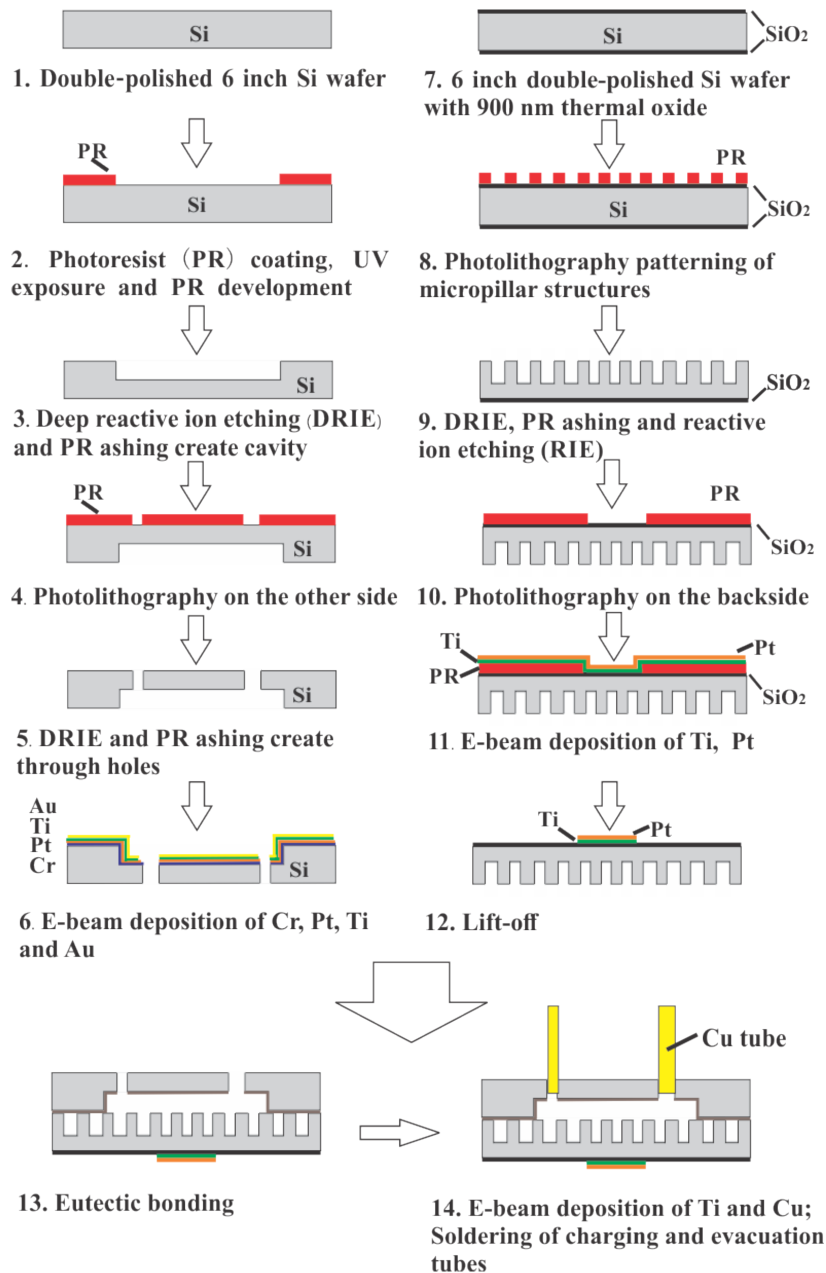

Figure 16: Steps of microfabrication process for sealed Si vapor chambers

After *step 2* was completed, the wafer was hard baked at 125℃ for 4 mins to enhance the adhesion of photoresist layer. The structure of 3 cm × 3 cm cavity with four 3 mm supporting posts on the backside of top wafer was then defined by DRIE, as shown in *step 3* of *Figure 16*. The remaining photoresist layer was then stripped by photoresist asher (*Tepla O2 Plasma Asher*). After that, the wafer was flipped and attached to a protective wafer. HDMS priming, 1.6 μm S1813 photoresist coating, 4 mins 125℃ soft

bake,10 s UV exposure and manual develop with 2.67% TMAH were performed, respectively to transfer the hole patterns in *Figure 15(b)* to the front side of the top wafer, as shown in *step 4* of *Figure 16*. Then DRIE was performed as *step 5* to etch 1/8'' and 1/16'' through thickness holes on the Si wafer, followed by photoresist removal. After the completion of *step 1* to *5*, 30 nm Cr layer, 150 nm Pt layer, 30 nm Ti layer and 500 nm Au layer were deposited subsequently on the backside of the top wafer. The Cr layer was the adhesion layer between Pt and Si substrate, while the 150 nm Pt act as barrier layer in eutectic bonding process. The Ti layer acted as adhesion layer between Au and Pt, while the 500 nm Au serve the function of forming Au-Si eutectic bonding between the top and bottom wafers of Si vapor chamber. By following the *step 1* to *6*, top wafer of the Si vapor chamber was fabricated.

Fabrication processes of the bottom wafer for Si vapor chamber are illustrated in *Figure 16, step 7 – 12*. The bottom wafer has micropillar structures on the front side and heater, RTDs on the backside. The detailed fabrication process of the bottom wafer is the same as the process discussed in *3.1.2* and *Figure 12.* The evaporator and adiabatic regions with micropillar structures were created by photolithography and DRIE by *steps 8 – 9.* The heater and RTDs were fabricated by photolithography, electron beam deposition of Ti and Pt layers and lift-off processes as illustrated in *steps 10 – 12*. By following the procedures from *steps 1 – 12*, 2 Si wafers were obtained. The wafers were cleaned with IPA and DI water. Each Si wafers were diced into 6 pieces of 4 cm × 4 cm dies. Eutectic bonding was then performed at 400°C for 20 mins by the bonding machine (*Karl Suss Bonder*) to create a hermetic sealing. Then 30 nm Ti and 500 nm Cu were coated on the front side of the top wafer to act as soldering pads. 2 Cu tubes with 1/8'' and 1/16'' sizes were then soldered to the sealed Si vapor chamber by heating on the hotplate at 205°C. Detailed soldering process can be found in [107].

3.2.3. Vapor Chamber Samples

Images of diced vapor chambers wafers are shown in *Figure 17*. According to *Figure 17(a)*, the backside of the top wafer has 4 circular supporting posts with a diameter of 3

mm. The purpose of adding 4 posts was to enhance the mechanical strength of the Si vapor chamber, so that the vapor chamber was not broken under vacuum condition.

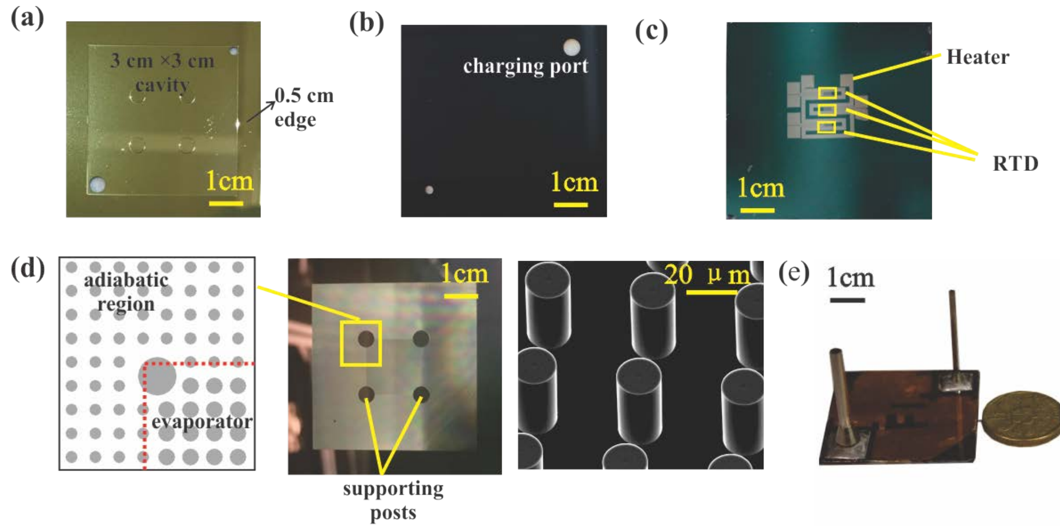

Figure 17: Images of Si vapor chambers (a) Backside of top wafer with 3 cm × 3 cm cavity (b) Front side of top wafer with 1/8'' and 1/16'' holes (c) Backside of bottom wafer with heater and RTDs (d) Front side of bottom wafer with micropillar structures and SEM image of micropillars (e) Sealed Si vapor chamber with thin thickness and 2 tubes.

The backside of the top wafer also has a DRIE etched cavity with 3 cm × 3 cm size and 100 μm depth. The cavity was covered by the metal layers described in *Figure 16, step 6*. Two through thickness holes with 1/8'' and 1/16'' sizes were used for liquid charging and vapor chamber evacuation, as shown in *Figure 17(b)*. The zig-zag pattern metal films on the backside of the bottom wafer were used as heater and RTDs. There are 1 heater and 3 RTDs with 8 contact pads in total according to in *Figure 17(c)*. The size of the heater is 1 cm × 1 cm. The front side of the bottom wafer is composed of micropillar arrays with squarely packed patterns. The evaporator with a size of 1 cm × 1 cm has different micropillar geometries as illustrated in *Figure 17(d)*. The 4 supporting posts locate at 4 corners of the evaporator, and the evaporator is surrounded by the adiabatic region. The total size of the micropillar array is 3 cm × 3 cm. The sealed Si vapor chamber was produced by bonding 2 Si wafers through eutectic bonding. Thus, the Si vapor chamber has thin thickness of around 1.25 mm, which is even thinner than a 1-dollar Singapore coin as shown in *Figure 17(e)*. Two Cu tubes were soldered at the 2 holes on

the sealed vapor chamber, which can be connected to the vacuum pump and charging setup. To conduct parametric studies, Si vapor chamber with various micropillar geometries was fabricated. The geometric sizes of each vapor chamber were measured by SEM and listed in *Table 9.* 10 readings were taken and averaged for the geometric measurements.

Table 9: List of Si vapor chamber with various micropillar geometries

Sample Number	Evaporator Region			Adiabatic Region		
	d **(μm)**	***h*** **(μm)**	***l*** **(μm)**	***d*** **(μm)**	***h*** **(μm)**	***l*** **(μm)**
A	18.9	31.3	30.6	15.8	31.3	30.6
B	15.5	31.3	35	15.8	31.3	30.6
C	15.5	31.3	27	15.8	31.3	30.6
D	16.5	38.0	27	15.8	31.3	30.6
E	4.6	17.7	16	7.8	17.7	16
F	9.2	17.7	16	7.8	17.7	16
G	18.9	30.3	30.6	15.8	30.3	30.6
H	15.8	27.2	30.6	16.1	27.2	30.6

3.3. Summary

In this chapter, detailed explanations of photomask designs for the uniform evaporator, biporous evaporator and sealed Si vapor chamber were discussed. The uniform biporous evaporator samples have micropillar patterns on the front side, which was micro fabricated by photolithography and deep reactive ion etching (DRIE). The backside of the evaporator sample has one 1 cm × 1 cm Pt heater and 4 resistance-temperature-detectors (RTDs) for heat supply and temperature measurement, respectively. The Si vapor chamber was composed of 2 processed Si wafers bonded by eutectic bonding at 400℃. A 100 μm deep cavity, one 1/8'' through wafer hole and one 1/16'' hole were fabricated on the top wafer to serve as vapor space, liquid charging and evacuation ports , respectively. The micropillar structures and Pt thin films were defined on the bottom wafer of the Si vapor chamber to act as evaporator, adiabatic sections and temperature sensors, respectively. Total size of the sealed Si vapor chamber is 4 cm × 4 cm × 1.25 cm, which is very thin. The aforementioned fabrication processes were listed in detail in this chapter.

Chapter 4: Thermal Characterizations

4.1. Thermal Characterization of Evaporators

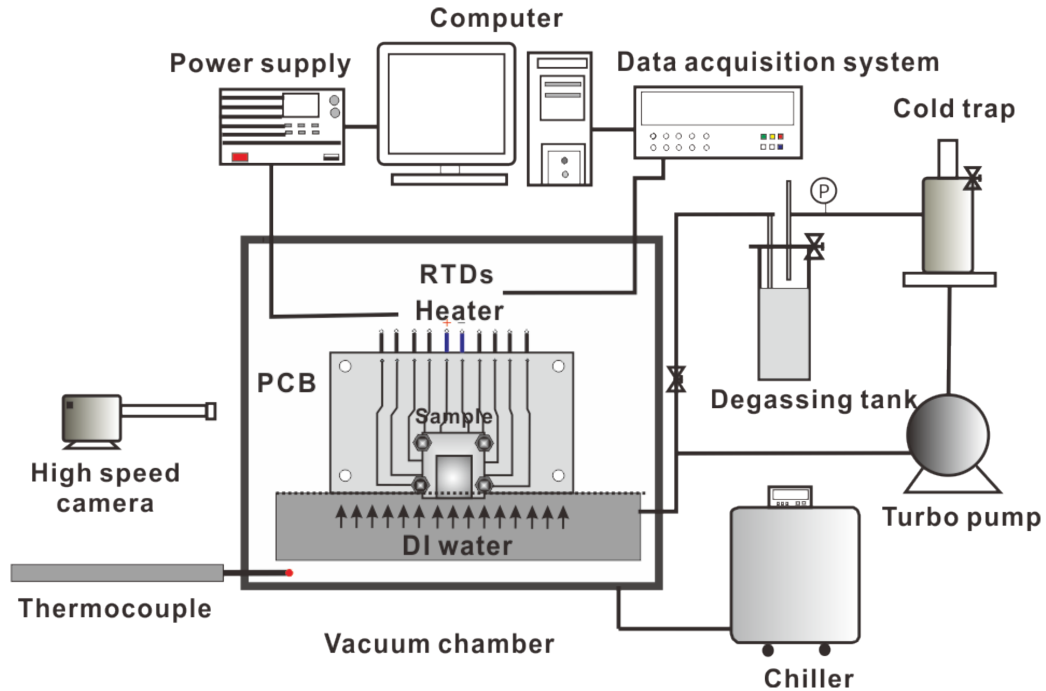

Figure 18: Schematic illustration of the experimental setup for uniform/biporous evaporators: The evaporator sample was mounted on a PCB with pogo pins to connect to power supply and data acquisition system. Thermal characterization was conducted inside vacuum chamber under vacuum condition. Working fluid used in the characterization was degassed in degassing tank. Evaporator dryout was monitored by high speed camera.

The experimental setup to thermally characterize the performance of uniform/biporous evaporators is illustrated in *Figure 18*. Before the thermal characterization tests, the evaporator samples were first cleaned thoroughly to remove any dirt or contaminants on the sample surface. The dirt or contaminants on sample surface may degrade the surface wettability and hinder phase change. Cleaning was done by immersing the sample in acetone, IPA and DI water for 10 mins, respectively, followed by gentle blow drying with compressed air. After that, the sample was plasma treated for 15 mins in a plasma cleaner (*PDC-001, Harrick Plasma*) to further remove any residual organic contaminants. When the cleaning process was completed, the sample was mounted onto a customized

Printed-Circuit-Board (PCB) with a size of 38.7 mm × 85.9 mm as shown in *Figure 18*. The PCB was designed with *Altium Designer 16*. There were 10 contact pads on the PCB with the size of 2 mm × 2.5 mm, which corresponded to the 10 contact pads of 1 heater and 4 RTDs on the sample backside. Each contact pad has a through thickness hole where a surface mount pogo-pin with a diameter of 2 mm and the total length of 3 mm can be soldered to it from the backside. The sample was mounted onto the PCB with a 1 mm thick silicone rubber O-ring on the backside and epoxy layer (*Epoxy Fix, Selleys*) at the bottom to prevent water leakage. The sample was secured tightly to the PCB by 4 M4 screws at the edges. 8 contact pads of the RTDs were connected to an RS232 9-pin connector through the internal wire layout of the PCB, and the 9-pin connector can be connected to a data acquisition system to collect data. DI water was used as working fluid used in the thermal characterization. Degassing was done by 3 freeze-pump-thaw cycles in the degassing tank as illustrated in *Figure 18*. The degassing tank was filled with DI water and closed tightly with 4 clamp screws. DI water in the degassing tank was then frozen by liquid nitrogen, followed by evacuating the tank with a turbo pump (*EXT 75DX, Edwards*) for around 1.5 hrs. Then the ice in the degassing tank was melted by a hotplate. After that, the freezing and evacuating were repeated for 2 times to ensure complete non-condensable gas removal. A comprehensive non-condensable gas removal was essential as the non-condensable gas may form a vapor layer near the micropillar wicks during evaporation, which may prevent further phase change and limit the performance of the evaporators.

After the sample cleaning and degassing, the evaporator sample with PCB sample holder was mounted onto a stand inside the vacuum chamber. The stand was connected to a linear motion push pull (*KLSDBA, Kurt J. Lesker*) and there was a liquid reservoir under the sample. The evaporator sample was held vertically during thermal characterization, this was to prevent flooding of the sample surface and ensure all the liquid was driven purely by capillary force. The vacuum chamber was then sealed and evacuated to a vacuum level of around $5\times10^{-5}\,mbar$ to simulate the actual working condition of a vapor chamber. Once the vacuum level was reached, the evacuation was stopped and the valve between the vacuum chamber and degassing tank was opened. Due to the pressure

difference between the degassing tank and the vacuum chamber, degassed DI water filled the liquid reservoir inside the vacuum chamber automatically. The valve was closed once the water level reached a certain liquid level mark on the liquid reservoir. The sample was then immersed in the liquid reservoir by 0.23 mm, which was controlled by the high accuracy linear motion push pull. One flange of the vacuum chamber was cooled by a chiller (*PD45R-20-A12E, Polyscience*), which served the function of the condenser in a vapor chamber and prevent vapor condensation on the viewing flange. After that, the voltage was applied to the evaporator sample through the connection between PCB and power supply (*PSW 160-21.6, Gwinstek*) with gradual increment. This was to mimic the heat generation of electronic devices in the actual case. Heat flux applied to the evaporator can be calculated by the following equation,

$$q''_{app} = \frac{IU}{A} \tag{45}$$

where U is the voltage applied to the heater and I is the current through the heater. A stands for the area of the heater, which was 1 cm^2 in this experiment. Resistance readings of the RTDs at each voltage was collected by data acquisition system (DAQ *34970a*, *Keysight*), while the chamber ambient temperature was measured by T type thermocouples (*L-0044T, Omega*). A high-speed camera (*SA3-60K, Photron*) was used to monitor the dryout on evaporator surface. Dryout heat flux was defined as the heat flux at which dryout was observed in evaporator wick.

4.2. Thermal Characterization of Vapor Chambers

Experimental setup for thermal characterization of vapor chambers is illustrated in *Figure 19 (a)*. As the case in evaporator sample thermal characterization, a PCB was designed to connect to the vapor chamber *Figure 19 (b)*. 8 gold-plated surface mount pogo-pins were soldered to the 8 contact pads of the PCB, which provided electrical connection between the power supply, data acquisition system and vapor chamber through an RS232 9 pin connector. A polytetrafluoroethylene (PTFE) holder was inserted in between of the vapor chamber and PCB to ensure good thermal insulation, as shown in *Figure 19 (c)*. A copper cooler that was connected to a 600 W temperature-controlled chiller (*PD45R-20-A12E, Polyscience*) acted as the heat sink for the vapor

chamber. Cross-sectional view and top view of the copper cooler are shown in *Figure 19 (a)* and *Figure 19 (c)*.

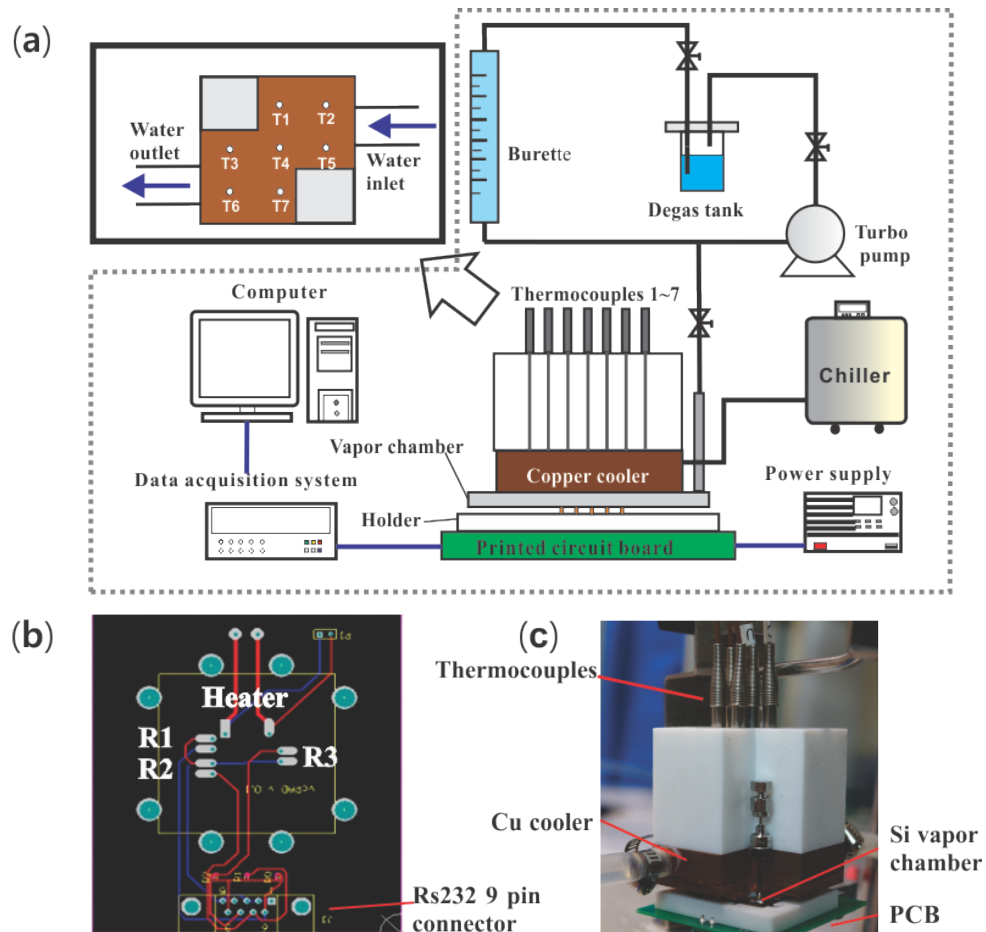

Figure 19:(a) Schematic illustration of the experimental setup for vapor chamber characterization: The vapor was mounted onto a PCB and evacuated by the turbo pump. Degassed DI water was filled into the vapor chamber to serve as working fluid. A copper cooler was used to cool the condenser side of the vapor chamber. Power was applied to the vapor chamber while resistance readings of RTDs were measured by DAQ. (b) The design of PCB: 8 contact pads corresponded to 3 RTDs and 1 heater, which were connected to an RS232 9 pin connector (c) Layout of vapor chamber mounted on PCB with 7 thermocouples to measure condenser temperature.

Prior to thermal characterization tests, the vapor chamber was evacuated to a vacuum level of 10^{-4} Pa by the turbo pump (*EXT 75DX, Edwards*). Pressure level inside the vapor chamber was monitored by a Pirani gauge (*TTR 91N, Leyold Thermovac*) to ensure that

there was no leakage. After evacuation, the vapor chamber was charged with degassed DI water. Degassing was done by following the 3 freeze-pump-thaw cycles as described in *section 4.1*. To accurately control the charging amount of liquid, the degassed DI water was first filled into a 3 ml burette which has 10 μl accuracy. To ensure a complete degassing, the burette was observed for over 4 hrs to make sure no bubble can be found inside it. Desired charging amount was calculated based on the micropillar geometries in evaporator and condenser region so that the space between micropillars was filled with liquid without any flooding. Then the chiller (*PD45R-20-A12E, Polyscience*), was turned on with a target temperature of 15°C. The cool liquid circulated inside the copper cooler on top of the vapor chamber.

After sample mounting, evacuation and charging, the thermal characterization was conducted by powering the heater with a power supply (*PSW 160-21.6, Gwinstek*). The power applied to the vapor chamber was increased gradually. Applied voltage ranged from 0 V to 140 V. At each voltage, resistance readings of the RTDs were recorded by the DAQ (*34970a, Keysight*) once steady state resistance was achieved. The temperature of the condenser side was measured by 7 thermocouples (*TJ160-CPSS-040U-2, Omega*) and recorded by the DAQ (*34970a, Keysight*). The layout of the 7 thermocouples is illustrated in *Figure 19 (a)*. Among the 7 thermocouples, T2 and T5 located near the inlet of water, while T3 and T6 located near to the water outlet. Heat flux applied to the vapor chamber can be calculated by *Equation (45)*.

4.3. Calibration and Data Interpretation

Pt based thin film RTDs were adopted in the thermal characterization of evaporators and vapor chambers. This was because Pt thin film has a linear relationship between its resistance and temperature. To correlate the resistance readings in *section 4.1* and *4.2* to temperature values, calibration of the RTDs for evaporator and vapor chambers was conducted. Evaporator and vapor chamber samples were mounted on the PCB holders and put into an oven (*OMH60, Heratherm*). Calibration was performed within a temperature range of 30℃ – 80℃ with increment of 5℃. The oven temperature was measured by a high precision Pt 100 RTD (*Omega*). At the steady state of each

temperature point, at which the temperature readings of Pt 100 RTD varied within 0.1°C, resistance readings of the RTD on the sample backside and temperature readings of the Pt 100 RTD were logged by the DAQ (*34970a, Keysight*). Then the temperature data versus resistance readings were plotted and fitted linearly to obtain the relationship between the resistance and temperature of the RTDs. Plots of temperature versus RTD resistance for 4 RTDs are shown in *Figure 20*. The coefficient of determination R^2 ranged from 0.9975 to 1, which indicated a good linearity of the resistance-temperature dependence. The relationship between sensor temperature T_{sensor} and RTD resistance R can be expressed as $T_{sensor} = aR + b$, where a and b are the slope and intercept of the fitted curve.

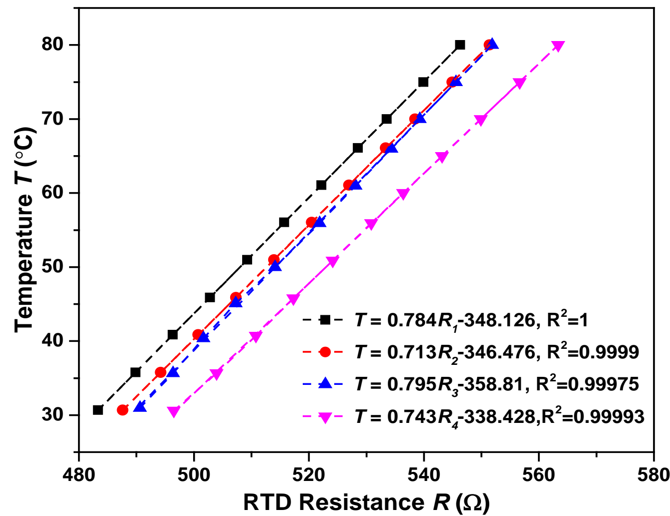

Figure 20: Temperature versus resistance readings of RTDs obtained by calibration inside an oven against a high precision Pt 100 RTD. Good linearity can be observed with $R^2 \approx 1$

Test results of thermal characterization will be plotted as dissipated heat flux *q''* versus superheat *ΔT* curves. The dissipated heat flux was denoted as heat flux removed by evaporative heat transfer and can be calculated by the following equation for evaporator samples:

$$q" = q"_{app} - q"_{loss} \tag{46}$$

where $q"_{loss}$ represents the heat loss. During the thermal characterization tests of evaporators, the heat flux dissipated was not entirely due to the evaporative phase change

heat transfer in micropillar wicks. Instead, the conduction from the evaporator to the liquid reservoir, the evaporation of the macroscopic meniscus at the bottom of the evaporator, heat spreading, the convection and radiation heat transfer also contributed to the heat dissipation of the evaporator samples, as shown in *Figure 21*. Therefore, heat loss due to these heat transfer modes needs to be evaluated and taken into consideration in data interpretation. Heat loss estimation was achieved by conducting thermal characterization tests for samples with heater and RTDs on the backside but without the micropillar structures on the front side, *i.e.,* the bare silicon samples. The thermal characterization and calibration procedures followed the steps described in *section 4.1*. Correlation between the measured heat flux and temperature was curve fitted to be $q''_{loss} = 0.1798\Delta T + 0.1173$. Using this fitted curve, the heat loss at a certain superheat can be evaluated. Since the bare silicon sample does not have any micropillar structures on the front side, this estimation provides an over-prediction of heat loss and is a conservative way of measuring the evaporator performance. Based on the heat loss curve, the heat flux dissipated by the evaporators can be calculated by $q'' = q''_{app} - q''_{loss}$.

Superheat was defined as the temperature difference between micropillar bottom T_{pillar} and chamber ambient temperature T_{sat}. Chamber ambient temperature referred to the saturation temperature T_{sat} of the vacuum chamber measured by type-T thermocouples (*L-0044T, Omega*). By assuming a 1D heat conduction through the silicon wafer, the micropillar temperature T_{pillar} can be calculated by the following equation:

$$T_{pillar} = T_{sensor} - q''\left(\frac{t_{wafer} - h - t_{SiO_2}}{k_{Si}} + \frac{t_{SiO_2}}{k_{SiO_2}}\right) \tag{47}$$

where the thickness of thermal oxide layer t_{SiO_2} and silicon wafer t_{wafer} equal to 930 nm and 650 μm, respectively. k_{Si} and k_{SiO_2} are the thermal conductivity of silicon and SiO_2, respectively. Thus, the superheat can be obtained as:

$$\begin{aligned} \Delta T &= T_{pillar} - T_{sat} \\ &= T_{sensor} - q''\left(\frac{t_{wafer} - h - t_{SiO_2}}{k_{Si}} + \frac{t_{SiO_2}}{k_{SiO_2}}\right) - T_{sat} \end{aligned} \tag{48}$$

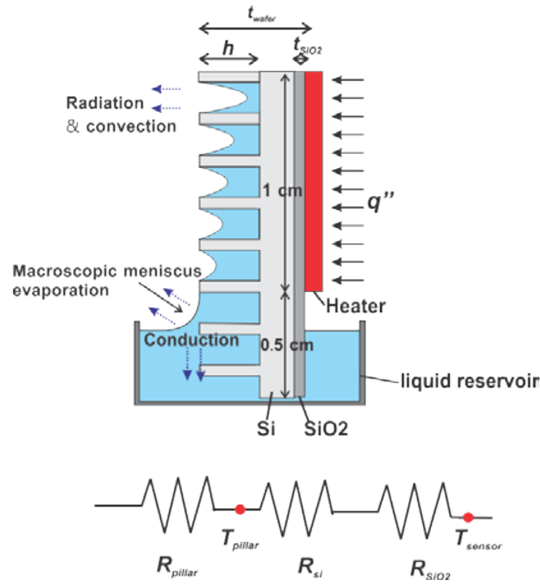

Figure 21: Heat dissipation not via evaporation in micropillar wicks, which includes evaporation from the macroscopic meniscus, convection, conduction and radiative heat transfer. And 1D conduction assumption of heat from the sensor to the micropillar bottom

The heat transfer coefficient h_c is also an important parameter to evaluate the effectiveness of the micropillar evaporator, which can be calculated by:

$$h_c = \frac{q"}{\Delta T} = \frac{q"_{app} - q"_{loss}}{\Delta T} \tag{49}$$

Moreover, the effective thermal resistance of silicon vapor chamber was also calculated, which was defined as the temperature difference between the evaporator and condenser section of the silicon vapor chamber divided by the heat flux. It can be expressed by the following equation:

$$R = \frac{T_{bottom} - T_{top}}{q"} \tag{50}$$

where T_{bottom} and T_{top} are the evaporator and condenser side temperature, respectively.

4.4. Uncertainty Analysis

Uncertainty for a calculated parameter can be obtained by adopting the uncertainty propagation equation [108]:

$$D_s = \sqrt{\sum_{1}^{N}((\frac{\partial S}{\partial m_n})D_{m_n})^2} \quad (51)$$

Based on *Equation (51)*, the uncertainty D_m of each measured parameter m contributes to the total uncertainty D_s of the calculated parameter S. Therefore, the uncertainty of heat flux q'', heat transfer coefficient h_c, and superheat ΔT can be calculated by uncertainty propagation of *Equation (51)*. The mean sources of the uncertainties were the uncertainties of DAQ, power supply, the standard deviation of the data *etc.*, and are listed in *Table 10*. Based on the calculations, the uncertainties in q'', h_c and ΔT were 9.84%, 15.9% and 0.114% ± 1.06˚C, respectively.

Table 10: Sources and values of uncertainties in thermal characterization

Parameter	Source	Uncertainty
Voltage V	DAQ	Reading × 0.0045% + 0.6 mV
	Power supply	Reading × 0.1%+100mV
	Standard deviation	0.003%
	Voltage drop along wire(0.6Ω)	0.01%
Current I	DAQ	Reading × 0.1% + 0.1 mA
	Power supply	Reading × 0.1% + 30 mA
	Standard deviation	0.004%
Superheat ΔT	Standard deviation	0.03%
	DAQ R measurements	Reading × 0.11%
	Curve fitting	0.06 K
	Thermocouple accuracy	1.0 K
Applied heat flux q''_{app}	V	0.352%
	I	5.163%
	A	1%
Heat loss q''_{loss}	V	0.88%
	I	8.21%
	A	1%
Heat flux q''	q''_{app}	5.27%
	q''_{loss}	8.32%
	Total	9.84%
Heat transfer coefficient h_c	q''	9.84%
	ΔT	0.114%±1.06K
	Total	15.9%

4.5. Summary

In the chapter, the experimental methodology adopted to thermally characterize the heat dissipation performance of uniform/biporous evaporators and vapor chambers was discussed.

After solution and plasma cleaning, the uniform/biporous evaporators were mounted onto a customized printed circuit board (PCB) to provide electrical connections. The sample was kept in a controlled vacuum chamber to simulate the pressure condition inside actual vapor chamber. DI water was degassed and used as working fluid. The evaporator sample was subjected to heat flux provided by Joule heating of the heater. The temperature of the evaporator was measured by resistance readings of the RTDs. In the thermal characterization of a vapor chamber, the vapor chamber sample was evacuated and charged with degassed DI water. After that, increasing voltage was applied to the heater while resistance readings of RTDs were taken. Condenser side temperature was measured by 7 thermocouples and connected to a copper cooler. To convert the RTD resistance readings into temperature measurements, calibration was done with a high accuracy Pt 100 RTD within a temperature range of 30˚C – 80˚C. The resistance at a certain temperature was recorded and plotted against temperature to obtain the relationship between R and T. Besides the thermal characterization tests and calibration, heat loss was estimated to calculate the heat flux dissipated by evaporation inside micropillar wicks. Lastly, the uncertainties in the measured parameters were analyzed and calculated.

Chapter 5: Performance, Optimization and Parametric Studies

5.1. Uniform Evaporator

5.1.1. Wettability

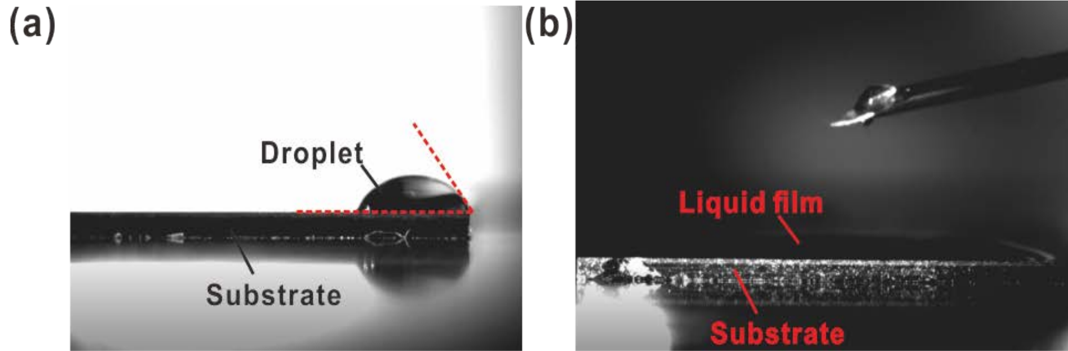

Figure 22: High speed camera image of (a) Water droplet on the plain silicon surface. The plain silicon surface is hydrophilic (b) Liquid spreading on uniform micropillar structured surface with superhydrophilic liquid spreading

The wettability of water droplet on plain silicon surface without any microstructures and on micropillared surface with uniformly distributed cylindrical micropillars are shown in the high-speed camera (*SA3-60K, Photron*) images in *Figure 22*. According to *Figure 22 (a)*, the plain silicon surface was hydrophilic with contact angle less than 90 ˚ as indicated by the dotted line. By introducing microstructures to the silicon surface, the liquid spreading was further enhanced with complete water spreading and ~ 0˚ contact angle for all samples after plasma cleaning as shown in *Figure 22 (b)*. This can be explained by Wenzel's relation, which can be expressed as:

$$\cos\theta_m = rf\,\cos\theta_p \tag{52}$$

where θ_m stands for the contact angle of microstructured rough surface and θ_p represents the contact angle of plain surface, *rf* is the roughness of the rough surface. This relationship was developed by Wenzel in 1936 [109] and valid for a droplet size that is 2 to 3 times order of magnitude larger than the roughness scale. The roughness *rf* can be calculated as the projected area of the surface divided by the actual area, which is larger than 1 for the rough surface. Thus, according to *Equation (52)*, by increasing surface roughness of a certain surface, an intrinsically hydrophilic surface appeared to be more hydrophilic. Similarly, an intrinsically hydrophobic surface also became more

hydrophobic by having more roughness structures on it. Therefore, the microengineering process of introducing micropillar structures to the silicon surface made it superhydrophilic. This is favorable in facilitating liquid spreading and promoting liquid circulation in a vapor chamber.

5.1.2. Liquid Propagation

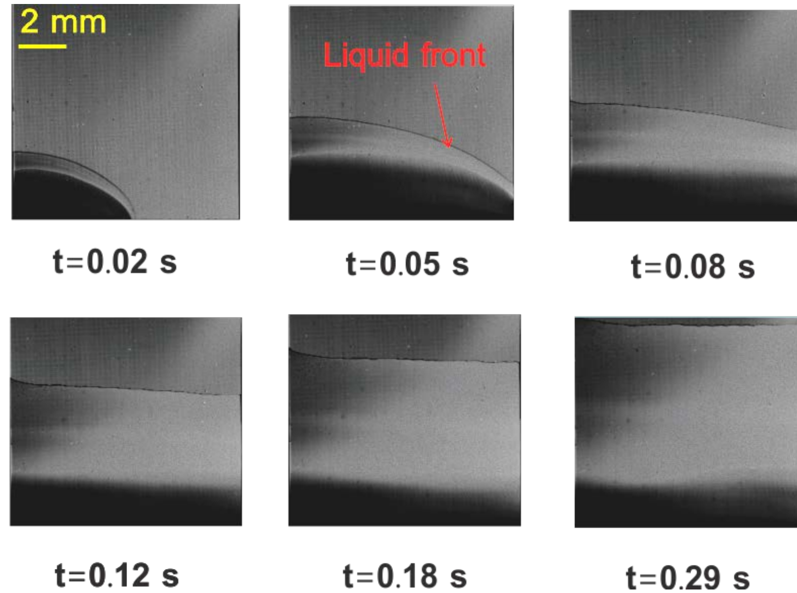

Figure 23: High-speed camera image of liquid climbing in a vertically aligned uniform micropillar evaporator at different time. Liquid front is indicated by the dotted lines.

In *section 5.1.1*, it has been proven that the uniform micropillar evaporators had excellent liquid spreading capability with low contact angle. Besides the liquid spreading capability on the uniform micropillar evaporators, the liquid climbing phenomena was also observed by a high-speed camera (*SA3-60K, Photron*) and the images are shown in *Figure 23*. Locations of the liquid front at t = 0.02 s, 0.05 s, 0.08 s, 0.12 s, 0.18 s, and 0.29 s were indicated by the dotted lines. Once the uniform micropillar evaporator was aligned vertically with its bottom touched the liquid reservoir, liquid can be driven to the micropillar wick by capillary pressure. Pumping of the liquid to the micropillar wick was automatic and anti-gravitational. This was attributed to the capillary force developed in the porous micropillar structures.

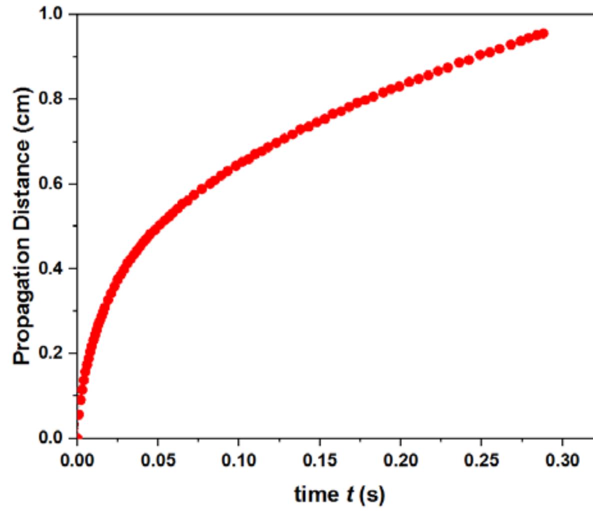

Figure 24: Liquid propagation distance as a function of time

According to *Figure 24*, it took only around 0.29 s for the liquid to climb about 0.99 cm along the vertical direction, which indicated that the liquid propagated at a very fast speed. For *sample 1 – 12*, the time it took for the liquid to climb along the entire 1 cm micropillar array height was 0.27 s, 0.29 s, 0.31 s, 0.27 s, 0.32 s, 0.33 s, 0.26 s, 0.28 s, 0.29 s, 0.37 s and 0.40 s, respectively. It can also be observed that the liquid propagation rate decreased as liquid moved upward. This was due to the viscous drag and gravitational effect that caused the decrease of liquid propagation velocity. The propagation distance versus time curve was in consistent with the capillary rate of rising experiment conducted by Nam *et al.* [78].

5.1.3. Optimization

Capillary limited dryout heat flux *q''* for uniform evaporator with cylindrical micropillars was derived in *section 2.1*. According to *Equation (14)*, the dryout heat flux is a function of the thermophysical properties of working fluid, material property of the micropillars and geometries of the micropillars. As discussed in *section 2.1*, for certain working fluid and micropillar material, for instance DI water and silicon as the case in this thesis, the dryout heat flux *q''* is determined by the micropillar geometries. The two important factors that govern the liquid propagation in micropillar wicks, capillary pressure P_{cap} and permeability K, are in competing effect. For example, for denser micropillar arrays, larger capillary force can be generated, however the reduction of

permeability will result in larger viscous loss as the liquid propagates. Therefore, an optimal geometric combination for uniform evaporator exist by balancing the permeability with capillary pressure. Optimization need to be conducted to find the optimal geometric combinations for micropillar. In actual case, micropillar evaporators that can dissipate large amount of concentrated heat with low temperature rise are desired. Therefore, to design an evaporator with large dryout heat flux and low temperature rise at the same time, optimization was conducted in *Matlab* with the following constraints applied:

$$\begin{cases} h/l > 1 \\ d/l < 0.57 \\ q'' = k_{eff}\dfrac{\Delta T}{h} \end{cases} \tag{53}$$

h/l ratio needs to be larger than 1 as the average assumption in the capillary pressure model was accurate only for $h/l > 1$. The d/l ratio was less than 0.57 as constrained by the permeability model of *Equation (19).* The expression for effective thermal conductivity of the micropillar wick, k_{eff}, was discussed in detail in *section 2.1* and was expressed in *Equation (23)*. Lower bound (*lb*) and upper bound (*ub*) for geometric sizes *d, h, l* were set to be *lb* = [3, 6, 6] and *ub* = [100, 100, 100] with a unit of μm for uniform evaporator optimization with superheat range of $\Delta T = 1 \sim 15°C$ at saturation temperature of 25 °C.

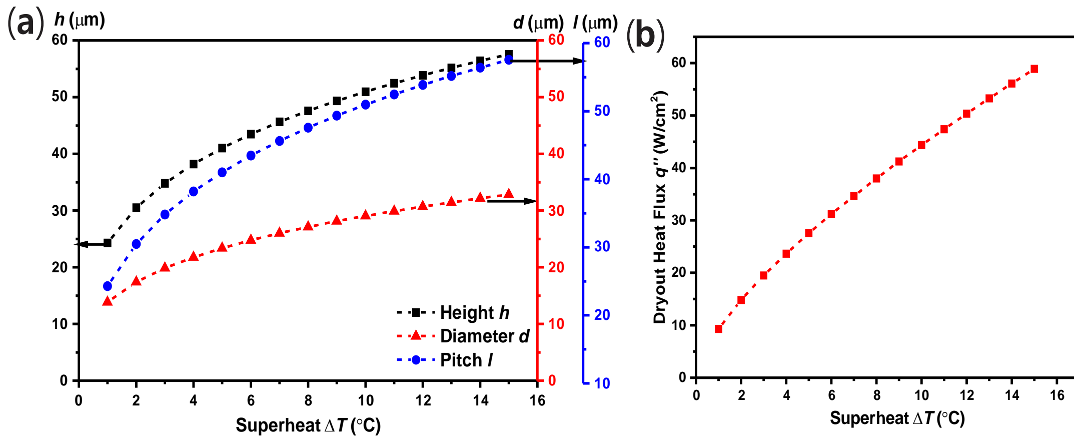

Figure 25:(a) Optimized geometric combinations with superheat range of 1 – 15 ℃ (b) The corresponding dryout heat flux at different superheat.

Temperature-dependent thermo-physical properties of water and material properties of silicon were used in optimization. Water temperature was taken as the average of sample surface temperature and ambient saturation temperature. Results for optimization for evaporator wick with wicking length L = 1 cm and receding contact angle θ = 10 ° [110] were plotted in *Figure 25(a)* and *Figure 25(b)*.

For each superheat value, there was a combination of d, h, l geometries that gave the highest dryout heat flux. The corresponding capillary-limited dryout heat flux for the evaporators at a certain superheat were shown in *Figure 25 (b)*. The optimal d, h, l sizes increase as superheat increases. This can serve as design guidance for micropillar evaporators with known allowable temperature rise. To investigate the parametric effect of micropillar geometries, geometric combination at ΔT = 5 °C was chosen as the benchmark. This corresponds to d = 23.3 µm, h = 41.0 µm, l = 41.0 µm as shown in *Table 7*, *sample 1*. The corresponding theoretical dryout heat flux was q'' = 27.5 W/cm^2. Parametric studies were conducted by changing the value of one of the parameters d, h, l while keeping the other two as constants in the following section.

5.1.4. Parametric Studies

Effect of *d/l*

Effect of micropillar d/l ratio on the evaporators' performance was studied by changing d or l while keeping the other two geometries as constants. The results were plotted in *Figure 26*. *Figure 26 (a) and (b)* plotted the test results with constant h = 39.5 µm, l = 41.0 µm while d ranged from 28.2 µm to 25.9 µm, 23.4 µm and 22.1 µm, while *Figure 26 (c) and (d)* shown the results with constant h = 39.5 µm, d = 23.4 µm and l varied from 34.0 µm to 36.0 µm, 41.0 µm and 44.0 µm. *Sample 1* has the optimized geometric size d = 23.4 µm, h = 39.5 µm, l = 41.0 µm and it can dissipate the largest amount of heat flux q'' = 25.8 W/cm^2 at very low superheat ΔT = 4.9 °C when dryout occurred, this corresponded to a thermal resistance of 0.19 K/W. Non-optimized sample with geometric sizes closer to *sample 1* has higher dryout heat flux. This indicated the importance and effectiveness of geometric optimization.

According to the effect of *d/l* ratio results on evaporators' heat transfer coefficient curves in *Figure 26 (b)* and *Figure 26 (d)*, it can be observed that heat transfer coefficient increased with larger *d* and smaller *l*. Thus, an increasing trend of heat transfer coefficient h_c with *d/l* ratio can be concluded. The thin film evaporation area for micropillar evaporators with higher *d/l* ratio was larger. For instance, with the same micropillar *d* and *h*, smaller *l* corresponded to larger number of micropillars, thus larger meniscus areas for evaporation within the same area of micropillar arrays.

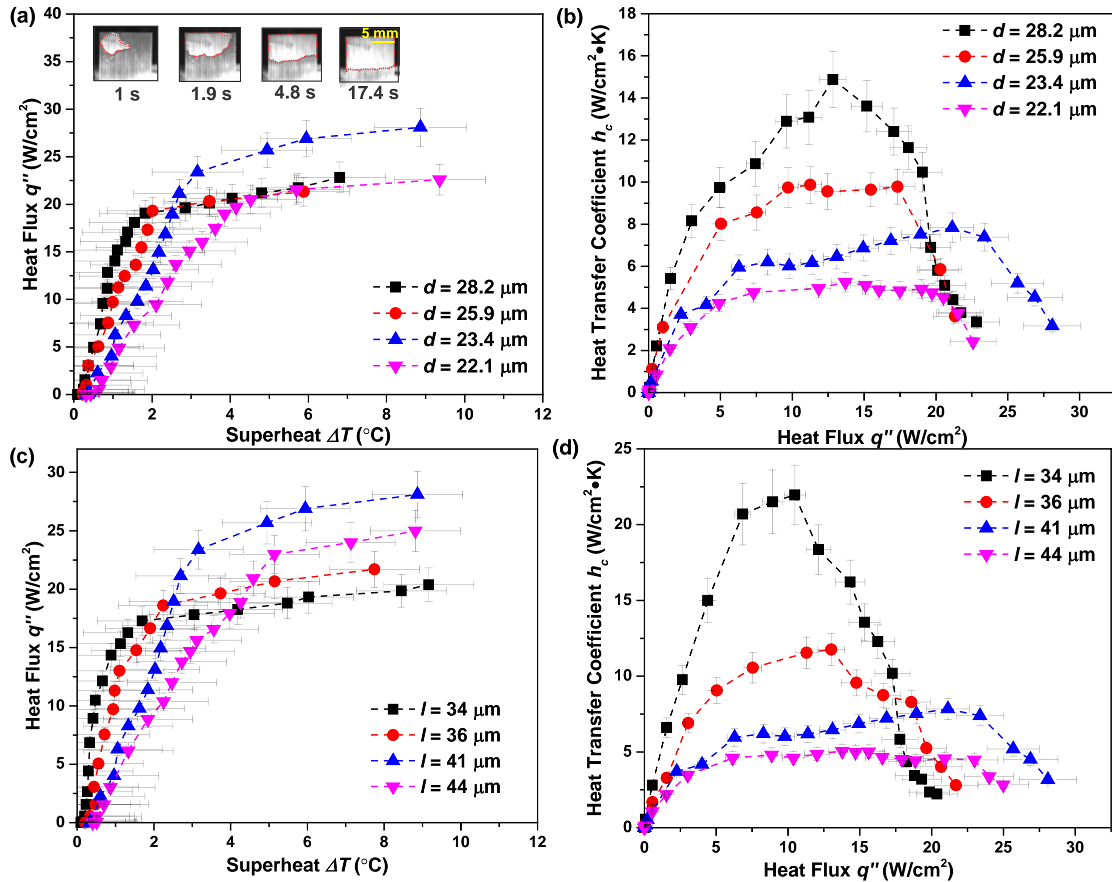

Figure 26: Effect of d/l ratio on uniform micropillar evaporators performance (a) Heat flux vs. superheat curve and (b) Heat transfer coefficient vs. heat flux curve for evaporator samples with constant h =39.5 μm, l = 41.0 μm while d changed from 28.2 to 25.9, 23.4 and 22.1 μm; (c) Heat flux vs. superheat curve and (d) Heat transfer coefficient vs. heat flux curve for evaporator samples with constant h = 39.5 μm, d = 23.4 μm while l varied from 34.0 to 36.0, 41.0 and 44.0 μm.

Based on the literatures [103 – 105], there were three regions of the liquid meniscus around the micropillars. Along the distance away from micropillar sidewall, the meniscus can be divided into intrinsic meniscus region, transition region and non-evaporating region as shown in *Figure 27(a)*. The intrinsic meniscus region and non-evaporating region were governed by surface tension and intermolecular forces, respectively, thus evaporation was restrained in these regions. More than 80% of the total evaporation heat transfer was occurred in the transition region that occupied only 20% of total meniscus areas with a liquid thickness of less than 5 μm. Thus, higher heat transfer coefficient was obtained with larger *d/l* ratio due to more thin film evaporation areas with same *d* and smaller *l* as shown in *Figure 27(c)*.

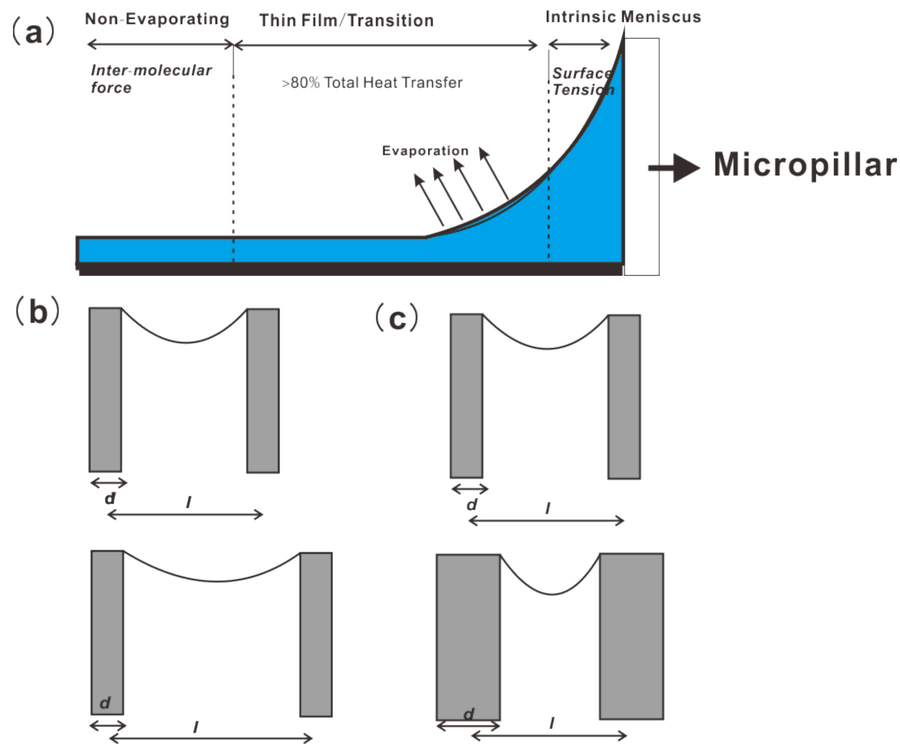

Figure 27: (a) Regions of liquid meniscus around a micropillar: intrinsic meniscus region governed by surface tension and non-evaporating region governed by intermolecular force, where evaporation was suppressed. The transition region accounted for more than 80% total heat transfer (b) Micropillars with same d, different l (c) Micropillars with same l, different d

Moreover, higher *d/l* ratio corresponded to a lower porosity ε and higher solid fraction *c*. With larger solid fraction, the evaporator was composed of more solid part with higher thermal conductivity (149 W/m·K for Si) rather than the less conductive liquid part (0.6 W/m·K for water). Thus, the total thermal resistance of the evaporator was lower with higher *d/l* ratio, which resulted in a higher heat transfer coefficient. Due to the aforementioned reasons, evaporator with larger *d/l* ratio can demonstrate higher heat transfer coefficient, which is in agreement with Ranjan *et al.* [103, 111].

Figure 26 (b) and *(d)* also revealed that heat transfer coefficient increased with heat flux first and then decreased after a certain point. This can be explained by the receding of liquid meniscus level between micropillars as heat flux increased. According to the plots in *Figure 28*, as the heat flux increased from low to a moderate level and liquid evaporated (*Figure 28 (a)* and *(b)*), liquid meniscus curvature in between of the micropillars at the top of the evaporator samples became larger. This resulted in more thin film evaporation areas and thus higher h_c.

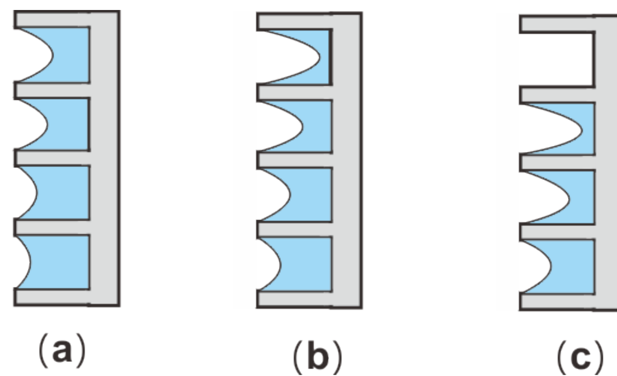

Figure 28:Liquid meniscus at various heat flux levels (a) Low to moderate heat flux (b) Higher heat flux prior to the inception of dryout (c) High heat flux after dryout. The liquid meniscus receded as heat flux increased, curvature and more evaporation areas before dryout (a – b). After dryout (c), evaporation areas decreased as there was no liquid in between of some micropillars

Heat transfer coefficient reached its maximum value when the meniscus was at the stage of *Figure 28 (b).* This critical value usually occurred prior to dryout where the liquid in between of the micropillars was not completely dried while the meniscus had a highest

curvature. When heat flux increased further and local dryout started to occur, less micropillar area was covered by liquid as shown in *Figure 28 (c)*. This caused the decrease of heat transfer coefficient. Due to the change of liquid meniscus from *Figure 28 (a)* to *Figure 28 (c)*, heat transfer coefficient increased to its maximum value first and then decreased. The dynamic recession behavior of the liquid-vapor interface was visualized using interferometry by Antao *et al.* [112]. Increasing number of fringes observed with increasing heat flux was an indication of higher meniscus curvature to compensate the evaporation rate. Beyond a critical heat flux, the meniscus de-pinned from micropillar tips and receded between the micropillars. This receding point was found to be geometric dependent by Antao *et al.* [112].

Effect of *h*

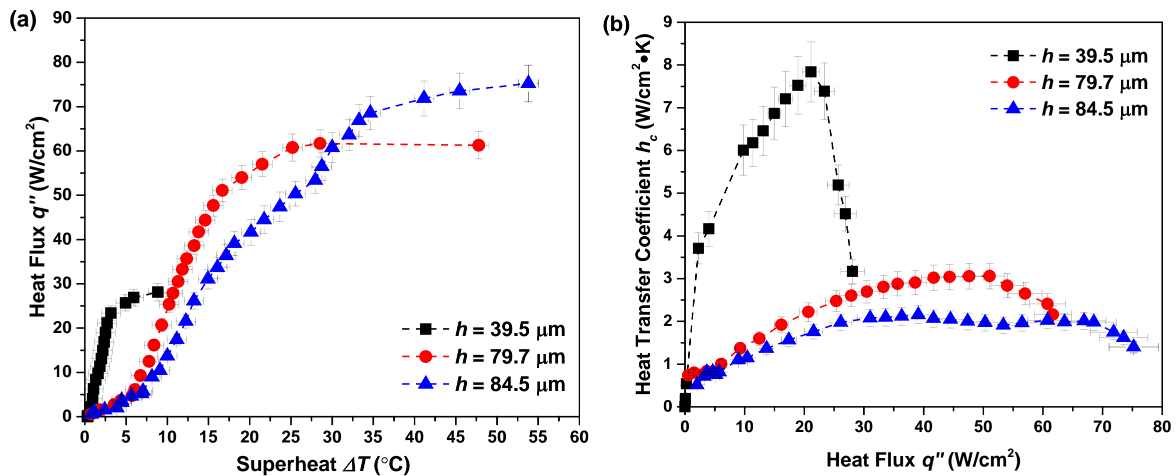

Figure 29:Effect of h on uniform micropillar evaporators performance (a) Heat flux vs. superheat curve (b) Heat transfer coefficient vs. heat flux curve for evaporator samples with h changed from 39.5 to 79.7 and 84.5 μm.

Evaporator samples with different h = 39.5 μm, 79.7 μm, 84.5 μm were tested. The results were plotted in *Figure 29(a)* and *(b)* as heat flux vs. superheat and heat transfer coefficient vs. heat flux curves. The dryout heat flux for h = 39.5 μm, 79.7 μm, 84.5 μm were q'' = 25.7, 60.8, and 68.5 W/cm^2, respectively. The larger dryout heat flux for taller micropillars can be explained by the larger liquid mass flow rate associated with a larger cross-sectional area of taller micropillar arrays. Therefore, taller micropillars have a

larger amount of liquid available for evaporation, which postponed the inception of dryout when the thin film evaporation areas were the same (same *d* and *l*). Moreover, the viscous drag from substrate ($\sim \mu \cdot du/dy$) was less profound for taller micropillars, which also led to a higher dryout heat flux. This trend agreed with previous theoretical and experimental studies [80, 81].

However, from *Figure 29 (b)*, it can be observed that micropillar with larger height has lower heat transfer coefficient and higher superheat, which was consistent with the trend reported in Zhu *et al.*'s work [76]. This observation can be explained by the thermal resistance of micropillars $R_{pins} = h/[(1-\varepsilon)k_{Si}]$, where k_{Si} was the thermal conductivity of silicon. Thus, a larger micropillar height corresponded to larger thermal resistance and lower heat transfer coefficient. As mentioned in the discussion of *d/l* effect, thermal resistance of micropillar was lower than that of liquid. Since the thermal resistance of micropillar and liquid meniscus were in parallel, the thermal resistance of the evaporator was mainly governed by the smaller micropillar resistance. Change of micropillar height had a profound effect in evaporator dryout heat flux and heat transfer coefficient. Although a larger dryout heat flux was desired for evaporator wick, the height of the micropillars cannot be unlimited tall due to the decrease of heat transfer coefficient and large superheat associated with taller micropillars. A larger height of micropillars will also bring in fabrication challenges for micropillars with large aspect ratios. Thus, for each allowable superheat during optimization process, a certain value of micropillar height was obtained instead of converging to the upper bound value as in the case without any superheat constrain in [81]. Since superheat was also a significant performance parameter of evaporator, the allowable superheat value should be taken into consideration during optimization.

5.1.5. Model Validation

The model predicted and experimentally measured dryout heat flux for the samples were plotted in *Figure 30 (a).* The model predictions were calculated by substituting the SEM measured geometric sizes into *Equation (14)*. Error bar for model predicted dryout heat flux was calculated based on the different measurements of micropillar geometric sizes

with SEM. Generally, the theoretical predictions and actual measured dryout heat flux were in good agreement with deviation within 20%. The model calculated dryout heat flux overestimated the dryout values according to *Figure 30*, one of the reasons was the over prediction of micropillar capillary pressure by Xiao *et al.*'s model [70]. Capillary pressure was predicted thermodynamically as the surface energy change per unit volume of liquid in this model. Thus, it captured P_{cap} accurately for transient cases with the wetting of micropillar sidewall with scallop structures. A roughness factor of π/2 was introduced in Xiao *et al.*'s model, which accounted for the *y*-direction scallop sidewall of the micropillars due to the cyclic etching and passivation process in DRIE.

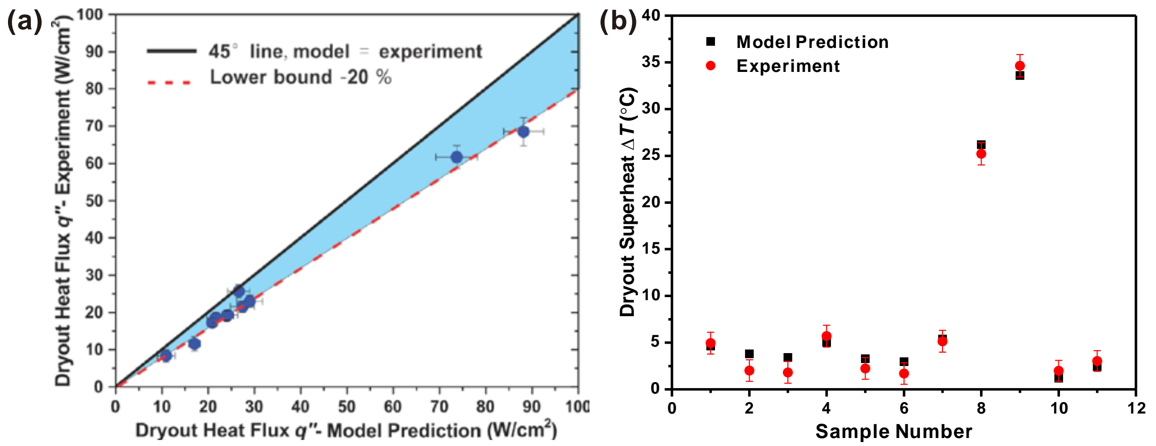

Figure 30: (a) Dryout heat flux for different uniform samples – model prediction vs. experimental measured values. Model overestimated the dryout heat flux within a difference of less than 20%. (b) Dryout superheat for various uniform evaporators, difference between model predicted and experimental measured dryout heat flux was within 2 K.

However, for this experiment with a steady state, the capillary pressure was not significantly influenced by micropillar sidewall roughness. In addition, the microscopic sweeping effect of liquid front that consumed part of the interfacial energy was also not considered in this model, thus the final interfacial energy for capillary pressure was lower than predicted [113]. Due to the aforementioned reasons, the capillary pressure value adopted in *Equation (14)* contributed to the overestimation of dryout heat flux. Moreover, an assumption of uniform thin film evaporation was assumed in developing the model. In actual case, the liquid-vapor interface was not isothermal, and the thin film

evaporation rate was not identical along the entire interface [103]. This was attributed to the variation of liquid film thickness, which resulted in the temperature difference between the liquid near the micropillar and the liquid in the center between micropillars. Due to the temperature difference, evaporation was not uniform and this assumption led to discrepancy between the model and experiment [115]. The aforementioned reasons contributed to the overestimation of dryout heat flux by the model. In general, the model of *Equation (14)* well predicted the dryout heat flux of the evaporators with given geometries with a discrepancy within 20%.

Superheat for uniform evaporators at dryout heat flux was plotted in *Figure 30 (b).* The model predictions of dryout superheat were calculated based on the dryout heat flux q'' of uniform evaporator with certain geometries and effective thermal conductivity of the uniform evaporator wick k_{eff}. By calculating q'' with *Equation (14)* and k_{eff} with *Equation (23)*, superheat was obtained with *Equation (22).* According to *Figure 30 (b)*, it can be observed that the measured dryout superheat and predicted dryout superheat had good agreement with deviation of less than 1.8 K. A flat liquid meniscus was assumed for simplification purpose in simulating the effective thermal conductivity k_{eff} of the wick in *Comsol*. However, in actual case the liquid meniscus curvature exists. Thus, the flat meniscus may lead to an underestimation of micropillar effective thermal conductivity. Moreover, not the entire liquid meniscus contributed to the thin film evaporation areas, as discussed in *section 5.1.4*. The transition/ thin film evaporation region, which occupied 20% of total liquid meniscus area, accounted more than 80% heat transfer. Therefore, different meniscus regions around a micropillar possess different heat transfer rates as discussed in [103, 111]. To obtain an accurate prediction of the micropillar effective thermal conductivity, the liquid meniscus need to be modeled with various heat transfer rates assigned for different regions. However, this out of the scope of this work. Last but not least, the accuracy of the thermocouples used to measure the chamber ambient temperature also contributed to the slight deviation of superheat values. Generally, our model captured the dryout heat flux and superheat accurately with deviation of $< 20\%$ and < 1.8 K, respectively.

5.2. Silicon Vapor Chambers

5.2.1. Optimization

The capillary limited dryout heat flux of a silicon vapor chamber with 2D liquid flow in uniform micropillar evaporator was modeled in *section 2.2* and expressed as *Equation (30)*. Like the capillary limited dryout heat flux of uniform evaporator with 1D liquid flow as discussed in *section 5.1.1*, optimization of uniform evaporator in vapor chamber need to be performed to obtain the best geometric combinations of micropillars that can lead to highest dryout heat flux. Optimization of *Equation (30)* was conducted in *Matlab* by calling the *fmincon* function. Inside a silicon vapor chamber, the evaporator served the main function of heat dissipation while the adiabatic region played an essential role in circulating the working fluid back to the evaporator. Therefore, unlike the optimization of dryout heat flux in uniform evaporator, the liquid propagation in surrounding adiabatic regions needs to be conducted. Optimization of geometric dependent parameter $\sqrt{KP_{cap}/\varepsilon}$ for adiabatic region was conducted in *Matlab*. Lower bound (*lb*) and upper bound (*ub*) for geometric sizes *d, h, l* were set to be *lb* = [3, 6, 6] and *ub* = [100, 100, 100] with a unit of μm for uniform evaporator optimization with superheat range of $\Delta T = 1 \sim 20°C$ at saturation temperature of 25 °C. Temperature related thermophysical properties of water were used in the optimization, where water temperature was calculated as the average temperature between the evaporator and saturation temperature. Since the uniform evaporator in the vapor chamber has a 2D liquid flow from 4 edges, the wicking length of 1 cm × 1 cm evaporator was 0.5 cm. The following constrains were applied in optimization of evaporator region:

$$\begin{cases} h/l > 1 \\ d/l < 0.57 \\ q" = k_{eff}\dfrac{\Delta T}{h} \end{cases} \tag{54}$$

Results for optimization of evaporator wick with wicking length *0.5 cm* and receding contact angle θ = 10 ° [110] were plotted in *Figure 31(a)* and *Figure 31 (b)*. To conduct parametric study, the optimal geometries at ΔT = 15℃ were selected as benchmark. *d*, *h*, *l* sizes varied for various silicon vapor chambers and the geometries for different vapor

chambers are listed in *Table 9* of *Chapter 3*. The optimal micropillar geometries in the uniform evaporator were d =17.4 µm, h = l =30.6 µm, which corresponded to a dryout heat flux of 110.5 W/cm^2. In the optimization of micropillars in adiabatic regions, height of the micropillars were set to be the same as that of micropillars in the evaporator region and h =30.6 µm. With h = l =30.6 µm, the optimized micropillar diameter d = 15 µm and pitch l = 30.6 µm. It can be observed that the optimized adiabatic region has a larger porosity compared to the optimized evaporator region. Adiabatic regions with this micropillar geometric combination can have larger permeability and lower flow resistance for liquid to propagate.

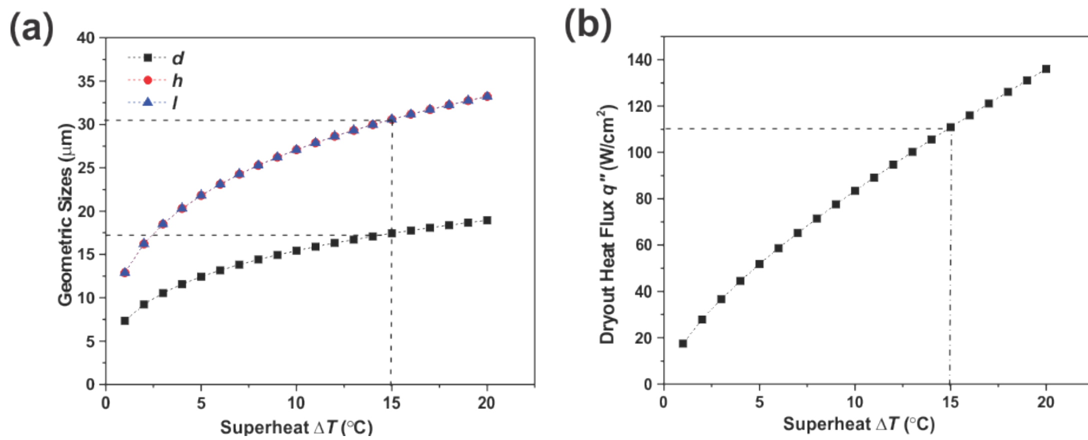

Figure 31: Optimization results of silicon vapor chamber evaporators for a superheat range of 1 ˚C to 20 ˚C (a) Optimized evaporator geometries d, h, and l (b) Corresponding dryout heat flux at various dryout superheats

5.2.2. Transient Temperature

Performances of silicon vapor chambers listed in *Table 9* were thermally characterized to determine the capillary limited dryout heat flux. Transient data for applied heat flux and temperature readings of RTDs for *sample H* are plotted in *Figure 32*. During the thermal characterization, a heat flux that increased in a stepwise manner was applied via the heater on the backside of the vapor chamber. A steady state evaporation was maintained for at least 2 mins before recording any data with DAQ for another 200 s. Steady state evaporation can be assumed when the temperature variation was within 0.1 ˚C. From *Figure 32*, it can be observed that the RTDs responded almost instantly to the

heat flux increment. This indicated that RTD was a fast-responding and reliable embedded temperature sensor that can be used to measure the temperatures on the backside of vapor chambers. Temperature readings plotted in *Figure 32* are the average values of the 3 RTDs on the backside of the sample. Error bars from the standard deviation of the 3 RTD readings was very small, which indicated that the local temperatures measured by the RTDs were nearly identical. Therefore, the vapor chamber worked nearly isothermally at steady-state evaporation. As heat flux increased, the fluctuations of temperatures became larger according to *Figure 32*. This may be attributed to the local dryout in the evaporator region, after which the heat transfer mechanism changed to convection instead of liquid/vapor phase change. Due to the lower heat transfer capability of convection compared to the large latent heat involved in phase change process, the temperature uniformity of evaporator in vapor chamber became worse with local dryout. Moreover, with constant heat flux increment, the temperature increments also became larger at higher heat flux. This was due to the larger evaporation rate of the working fluid at higher heat flux, where the liquid supply from the adiabatic region to the evaporator region became less sufficient to compensate for the liquid evaporated. Therefore, due to the insufficient liquid supply and decrease of thin film evaporation areas at dryout, sharp temperature increase was observed.

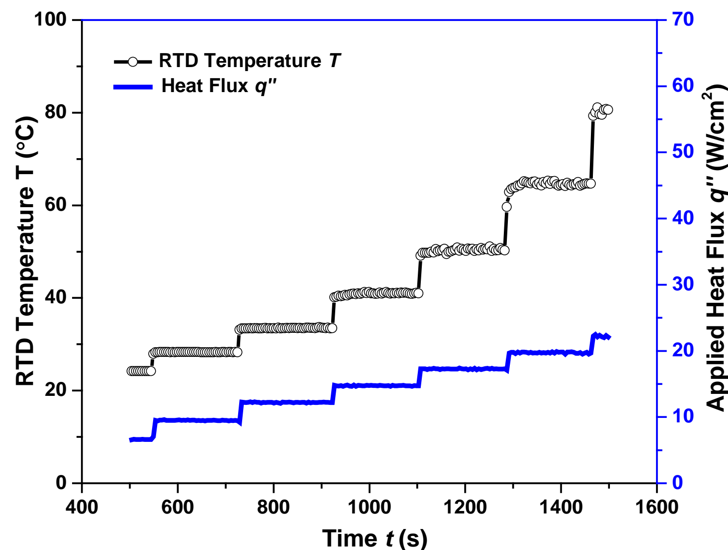

Figure 32: Heat flux and RTD temperature of vapor chamber sample H as a function of time

5.2.3. Parametric Studies

Silicon vapor chambers with various geometries were thermally tested. The results were plotted in *Figure 33(a)* and *(b)* as heat flux versus temperature difference and effective thermal conductivity versus heat flux curves, respectively. Among silicon vapor chambers *A* to *G*, *sample G* was an evacuated vapor chamber without liquid charging and was tested for comparison purpose. The dryout in the evaporators of sealed silicon vapor chambers cannot be observed with high-speed camera. As discussed in *section 5.1*, a sharp temperature increase was observed for 1D uniform evaporators at dryout. Therefore, the bending points of the heat flux versus temperature difference curves were defined as the dryout. Dryout points for various silicon vapor chambers were indicated by the arrows in *Figure 33(a)*. From *Figure 33(a)* and *(b)*, it can be observed that all charged Si vapor chambers (*sample A – F*) outperformed the non-charged *sample G*. Temperature rise of *sample A – F* was much lower than that of *sample G* at the same applied heat flux. This was attributed to the large latent heat involved in the phase change process for working fluid enclosed in *sample A – F*, which allowed heat to be dissipate effectively with low temperature rise. Meanwhile, *sample G* transferred heat purely by conduction and convection. The temperature increase in *Figure 33(a)* and thermal resistance increase in Figure 33*(b)* can be observed after the inception of dryout for *sample A – F*. The thin film evaporation areas in the uniform evaporators of silicon vapor chambers were largely reduced after dryout, which lead to an increase in temperature rise and thermal resistance. The trend of effective thermal resistance for *sample A – F* was decreased first at low to moderate heat fluxes, while increased after dryout. This can also be explained by the schematic drawing in *Figure 28*. As the heat flux increased from low to moderate levels, the meniscus curvature in between of micropillars increased because of faster liquid evaporation rate. This caused an increase in thin film evaporation areas and thus decrease of the effective thermal resistance of vapor chambers at the initial stage. The effective thermal conductivity of the silicon vapor chamber reached its minimal value just prior to dryout, where the curvature of liquid meniscus was largest as shown in *Figure 28(b).* After that, liquid started to recede in the micropillars of the

uniform evaporators, local dryout was initiated and the effective thermal had an upward tendency after that.

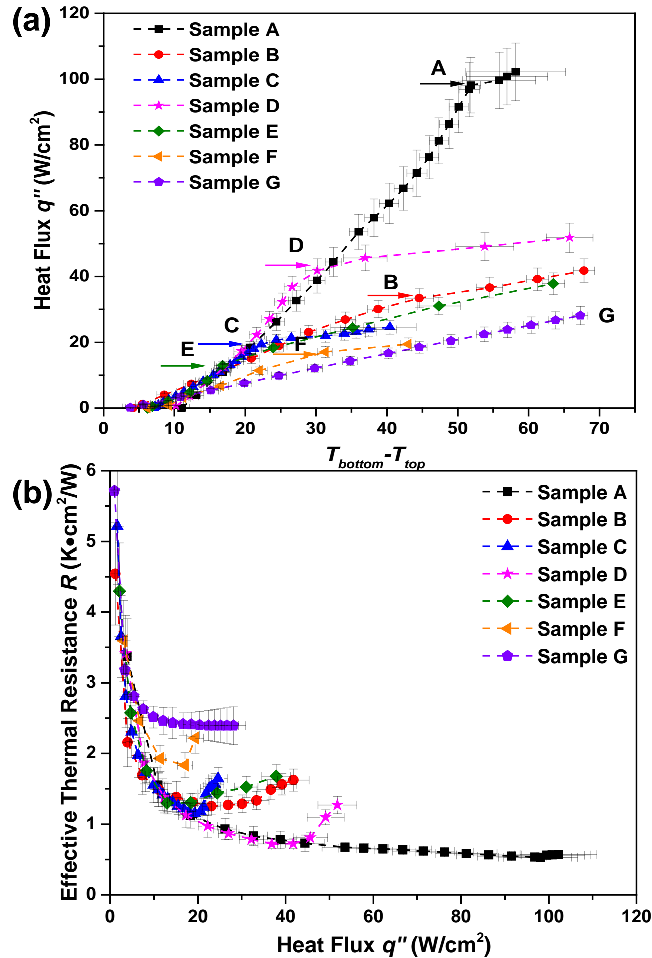

Figure 33: Parametric studies (a) Heat flux q'' versus temperature difference between evaporator and condenser curve for silicon vapor chamber A to G (b) Effective thermal resistance versus heat flux curve. Out of which sample G is a reference sample without liquid charging

Performance comparison among *sample A – F* was also conducted. Among all the silicon vapor chambers, *sample A* had the optimal geometries with d = 18.9 μm, h = 31.3 μm and l = 30.6 μm in the uniform evaporator region while d = 15.8 μm, h = 31.3 μm and l = 30.6 μm in the surrounding adiabatic regions. As shown in *Figure 33(a)*, *sample A* performed best with a highest dryout heat flux of q'' = 98.1 W/cm^2 and lowest effective thermal resistance of 0.53 Kcm^2/W. The dryout heat fluxes of *sample B – F* with non-

optimal geometries were *q''* = 36.6 W/cm^2, 21.3 W/cm^2, 45.7 W/cm^2, 12.9 W/cm^2 and 17.1 W/cm^2, respectively. This was due to the optimized size of *sample A* which gives the best balance between the capillary pressure and permeability for liquid transportation. Moreover, the geometries for micropillars in the uniform evaporators of *sample B – D* are closer to *sample A* compared to that of *sample E* and *F*. Dryout heat fluxes of *sample B – D* were larger than that of *sample E* and *F* as well. Thus, conclusions can be drawn that the vapor chambers with geometries closer to the optimized sizes have higher dryout heat flux, which is in consistent with the observation of the results discussed in *section 5.1.4*. The *d/l* ratio of uniform evaporator in *sample A – C* was 0.61, 0.44 and 0.57, respectively. By comparing the heat transfer performance of *sample A – C* in *Figure 33*, it can be observed that the silicon vapor chamber with denser micropillar arrays in the evaporator has lower temperature difference and smaller effective thermal resistance. There were twofold of reasons for this observation. Firstly, with a higher *d/l* ratio and denser micropillar arrays, the micropillar wick was composed of more highly conductive micropillars instead of less conductive micropillars. Therefore, the effective thermal resistance of silicon vapor chambers with higher *d/l* ratio was smaller. Moreover, micropillar evaporators with higher *d/l* ratio have more micropillars and more thin film evaporation areas available. This resulted in effective heat removal and lower temperature difference between the evaporator side and condenser side of the silicon vapor chamber. Thermal performance of *sample C* and *sample D* was also compared. *Sample D* had micropillar arrays with higher *d/l* ratio of 0.67 and taller micropillar height of 38 µm compared to that of *sample C*. It can be observed from *Figure 33(a)* and *(b)* that *sample D* had higher dryout heat flux and lower effective thermal resistance than *sample C*. The taller micropillars in the evaporator of *sample D* provided more space for a larger volumetric flow rate of the working fluid. Moreover, the viscous drag from the silicon substrate was less profound for evaporators with taller micropillars. The larger *d/l* ratio of *sample D* allowed evaporation in larger thin film evaporation areas, thus led to lower effective thermal resistance of *sample D*. In conclusions, the parametric studies revealed the effectiveness of optimization. Silicon vapor chambers with a higher *d/l* ratio

in the evaporator regions and taller micropillar height could dissipate heat flux at lower effective thermal resistance.

5.2.4. Temperature Distribution

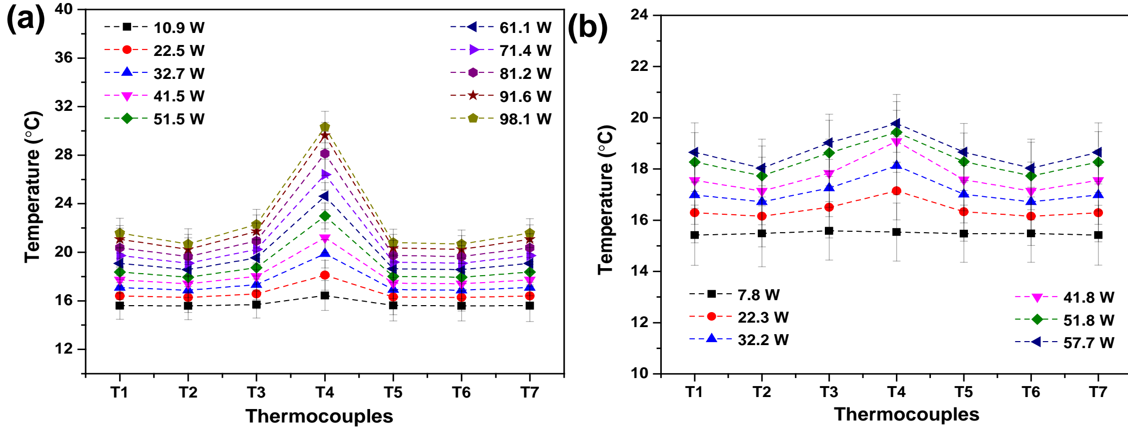

Figure 34: Condenser side temperature distribution of (a) sample A (b) sample D

Temperature distribution on the condenser side of the silicon vapor chamber *sample A* and *sample D* were plotted in *Figure 34(a)* and *(b)* respectively. The temperature on the condenser was measured by the 7 thermocouples with a layout illustrated in *Figure 19*. It can be observed that the temperature distribution was generally uniform for chamber *sample A* and *sample D* at various heat loads according to *Figure 34*. Among the measurements of the 7 thermocouples, *T4* always had the highest temperature reading. According to the locations of the thermocouples, *T4* located at the center of the condenser for the silicon vapor chambers. The Pt heater on the backside of the evaporator located at the center of the bottom substrate of the vapor chamber, which caused more concentrated heat loads in the center part and thus highest temperature of *T4*. Moreover, the silicon vapor chambers were supported by 4 posts to enhance the mechanical strength. Part of the applied heat flux was conducted through the supporting posts to the top substrate directly. This also explained the highest temperature for *T4* compared to that of *T2* and *T5*. The temperature readings of *T3*, *T7* were always higher than that of *T2* and *T5*. As the condenser was cooled by a copper cooler with water circulated inside, the non-uniformity of water temperature at the inlet and outlet may cause the temperature non-uniformity for various thermocouples. As shown in *Figure 19*, *T2* and *T5* located near the water inlet while *T3* and *T7* were at the vicinity of water outlet. Water was heated

up as it flowed above the hot condenser from the inlet to the outlet. According to [37], larger amount of heat can be taken away when the temperature difference between the cold water and hot condenser was larger. Therefore, the inlet water could dissipate more heat while the outlet water dissipated less. As a result, the temperature near the inlet of the cooler was lower than that at the outlet of the cooler.

For both *sample A* and *sample D*, the temperature non-uniformity increased with higher heat loads. The largest temperature difference was 9.64 ˚C at 98.1 W for *sample A* between *T4* and *T5*. Due to the existence of thermal spreading resistance along the horizontal top surface, it was harder to distribute the concentrated heat uniformly on the condenser side at larger heat loads. As shown in *Figure 19*, the condenser side was not entirely cooled by the copper chiller, spaces were left to accommodate the charging and evacuation tubes. This resulted in non-effective heat removal at some part of the condenser and gave rise to the temperature non-uniformity as well. In general, the temperature uniformity of the silicon vapor chamber was excellent, which can be further enhanced by adopting copper chiller that can cover the entire surface of the condenser.

5.2.5. Performance Comparison

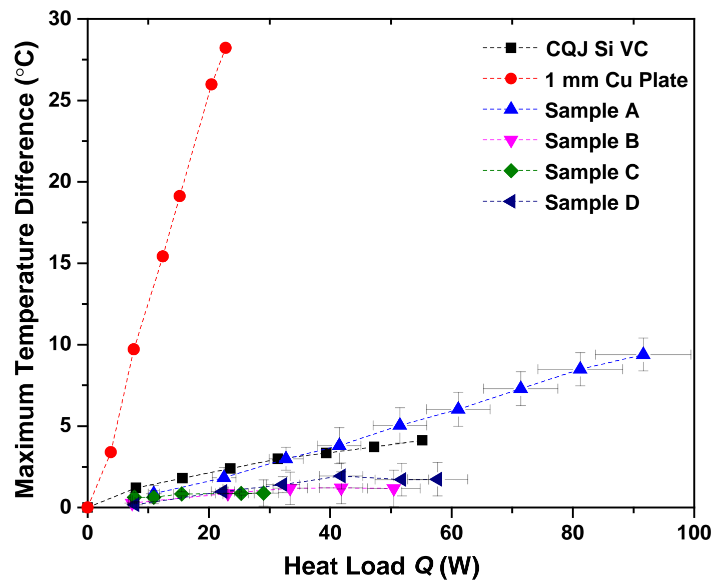

Figure 35: Performance comparison between our silicon vapor chambers and the most up-to-date silicon vapor chamber fabricated by Cai et al. [56]

Temperature uniformity of our silicon vapor chamber *sample A – D* was compared to that of the silicon vapor chamber fabricated by Cai *et al.* [56]. Cai *et al.* [56] fabricated the silicon vapor by bonding 3 silicon substrates with thickness of 350 μm, 350 μm and 300 μm. The evaporator of their silicon vapor chamber was composed of multi-wick structures with cavity size of 5 μm to 100 μm, and height of 150 μm. The condenser side of the three-stack was patterned with cubic micropillars of 200 μm width, 100 μm gaps and 100 μm height. Total size of this silicon vapor chamber was 50 mm × 70 mm × 1 mm. Thermal characterization was performed on this silicon vapor chamber with a heater size of 5 mm × 8 mm. A copper plate with the same geometric size was also tested under the same condition. To compare the performance of the silicon vapor chamber fabricated by Cai *et al.*, the maximum temperature difference versus heat load curves were plotted in *Figure 35*. The largest temperature difference across the surface for the copper plate was 28 ˚C at 24 W and 74˚C at 60 W, respectively. The maximum temperature differences for all the silicon vapor chambers were within 5 ˚C for all the silicon vapor chambers. Thus, silicon vapor chambers perform much superior to copper plates in terms of their better temperature uniformity and larger effective thermal conductivity. Our silicon vapor chamber *sample A – D* outperformed the silicon vapor chamber of Cai *et al.* with a heat load below 50 W in terms of a lower maximum temperature difference at the same heat load. *Sample A* had a higher maximum temperature difference for heat load larger than 50 W. However, it was capable of dissipating a maximum heat load of 98.1 W prior to dryout, which was higher than the heat load of 60 W demonstrated by the silicon vapor chamber of Cai *et al.*. In conclusion, our silicon vapor chamber possesses excellent performance.

5.3. Biporous Evaporators

5.3.1. Parametric Studies

Biporous *sample 1 – 7* were tested to study the effect of biporous evaporator micropillar island width 2i and microchannel width 2w on the dryout heat flux q'' and heat transfer coefficient h_c. Results were plotted in *Figure 36*. *Figure 36 (a)* and *5(b)* presented the performance comparison between *sample 1 – 4* that had the same d = 3.4 μm, h =8.9 μm,

l = 6 µm, 2w = 117 µm and various 2i ranged from 120 µm, 202 µm, 240 µm to 280 µm. While the q'' versus ΔT and h_c versus q'' plots were shown in *Figure 36 (c)* and *5 (d)*, respectively for *sample 2, 5 – 7* with identical d = 3.4 µm, h = 8.9 µm, l = 6 µm, 2i = 202 µm and various 2w ranged from 60 µm, 90 µm, 117 µm to 150 µm. Dissipated heat flux was caculated based on *Equation (45)* and *(46)* with heat loss being substracted from the total applied heat flux.

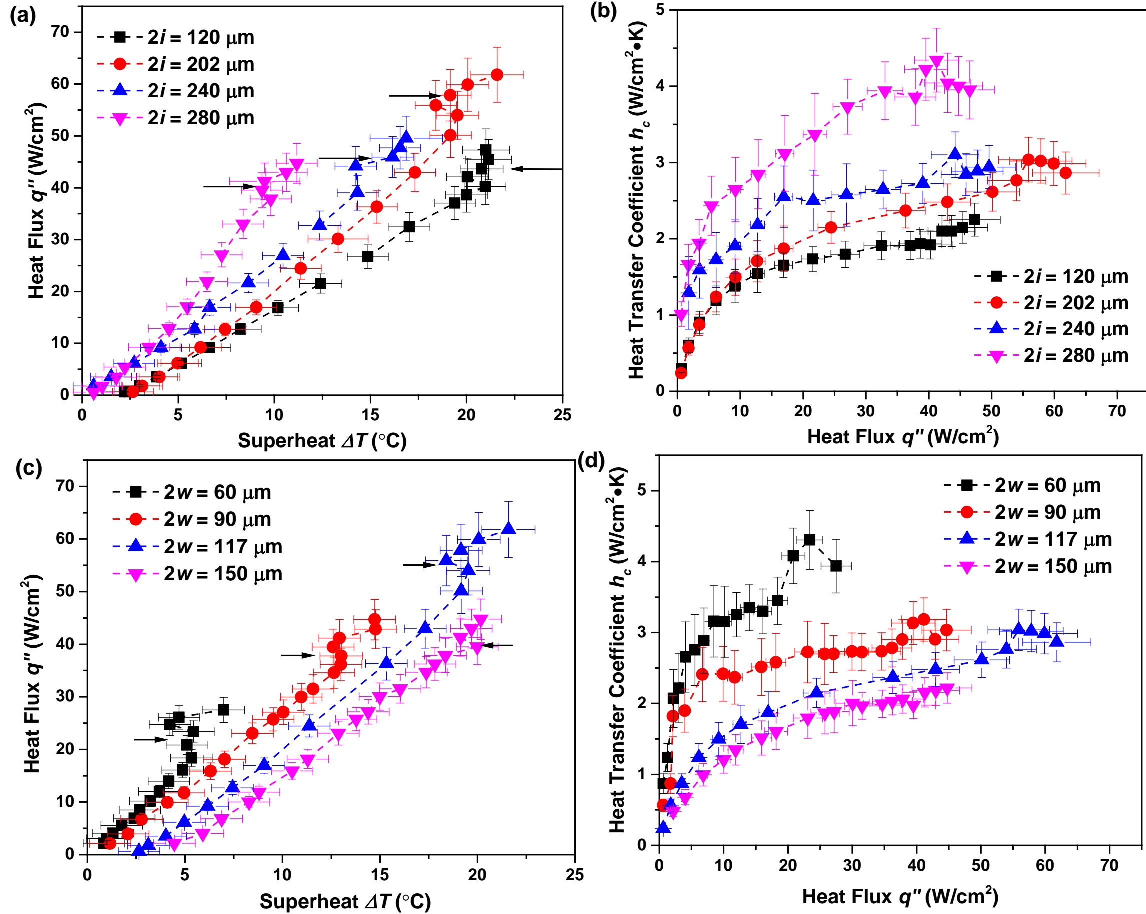

Figure 36:Parametric studies of biporous evaporators with various micropillar island width 2i and microchannel width 2w. (a) Heat flux versus superheat curve and (b) Heat transfer coefficient versus heat flux curve of sample 1 – 4 with constant d= 3.4 µm, h=8.9 µm, l = 6 µm, 2w = 117 µm and various 2i ranged from 120, 202, 240 to 280 µm. (c) Heat flux versus superheat curve and (d) Heat transfer coefficient versus heat flux curve of sample 2, 5 – 7 with constant d= 3.4 µm, h=8.9 µm, l = 6 µm, 2i = 202 µm and various 2w ranged from 60, 90, 117 to 150 µm.

The heat loss due to evaporation from macroscopic meniscus, conduction from sample to liquid reservoir, convection and radiation was around 8.0% of total heat flux applied $q"_{app}$ at a superheat of 15 °C. Superheat was calculated by converting the RTD resistance readings into temperature readings based on calibration curves and *Equation (48),* where 1D conduction across the SiO_2 layer and Si substrate.Error bars in *Figure 36* was calculated based on uncertainty propagation theory in *section 4.4*.

Dryout heat flux of various samples were indicated by the arrows in *Figure 36 (a)* and *36(c).* A dryout heat flux of 55.9 W/cm^2 was demonstrated by *sample 2* with $2i$ = 202 µm and $2w$ = 117 µm, which was the highest among *sample 1 – 7*. As shown in *Figure 36 (a)*, dryout heat flux decreased as micropillar island width increased from 202 µm to 240 µm and 280 µm for *sample 2 – 4*. Microchannels were incorporated in biporous evaporators as local liquid reservoir to shorten the liquid propagation distance and the local liquid propagation distance was half micropillar width i. As micropillar island width increased, the local liquid propagation distance increased. This led to a higher viscous resistance. Since the micropillar islands were composed of uniformly distributed micropillars with the same d, h, l, the capillary pressure P_{cap} generated by the micropillar islands were identical for *sample 2 – 4* according to *Equation (15).* Therefore, biporous evaporators with wider micropillar island widths dry at lower heat flux. This was in consistent with [80, 115]. *Sample 1* with $2i$ = 120 µm possessed a smaller dryout heat flux compared to that of *sample 2* with $2i$ = 202 µm. A narrower micropillar island width corresponded to a smaller thin film evaporation area as the narrower micropillar island can accommodate less number of micropillars. Consequently, once the micropillar island width was too small, the biporous evaporator also dried at lower heat flux due to the reduction of thin film evaporation areas. According to *Figure 36 (c)*, dryout heat flux decreased as microchannel width decreased from 117 µm to 90 µm and 60 µm for sample 2, 6 and 5. This was attributed to the higher pressure drop P_{la} inside narrower microchannels according to *Equation (41)* and *(42).* Dryout occurred when the capillary pressured developed in the evaporator wick was not able to overcome the pressure loss in the wick. Thus, with higher pressure drop of narrower microchannels, inception of dryout for biporous evaporators was triggered at lower heat flux. Moreover, the

volumetric flow rate of working fluid was also larger for wider microchannels with larger cross-sectional areas. Larger amount of liquid was available to compensate the liquid evaporated, thus dryout for wider microchannel evaporators was observed at higher heat flux. Meanwhile, once the increase of microchannel width was beyond a certain critical point, dryout heat flux started to decrease. Dryout heat flux of *sample 7* with $2w = 150$ μm was smaller compared to that of *sample 2* with $2w = 117$ μm. This was because the total biporous evaporator area was identical 1 cm × 1 cm for *sample 2* and *sample 7*. A larger microchannel width also corresponded to smaller micropillar island area and less area for thin film evaporation, which consequently led to a smaller dryout heat flux. Dryout heat flux of *sample 3* with $2i = 240$ μm was larger than that of *sample 4* with $2i = 280$ μm, while dryout heat flux of *sample 6* with $2w = 90$ μm outperformed that of *sample 5* with $2w = 60$ μm. Thus, biporous evaporators with micropillar island width and microchannel width closer to the geometric sizes of *sample 3* had a higher dryout heat flux. This indicated that an optimal island width and microchannel width existed. *Sample 3* was the one with optimal micropillar island width and microchannel width combination among those biporous evaporators.

From the graphs in *Figure 36 (a)* to *36(d),* biporous evaporator samples with wider micropillar islands and narrower microchannels could dissipate the same amount of heat flux at lower superheat ΔT and higher heat transfer coefficient h_c. This can be explained by the thin film evaporation mechanism in micropillar wicks. The liquid meniscus around a micropillar can be divided into 3 regions according to literatures [103 – 105]. Along the distance from the micropillar sidewalls, the liquid meniscus regions were defined as intrinsic meniscus region, thin film evaporation region and non-evaporation regions. Evaporation in intrinsic meniscus region and non-evaporation regions was suppressed by surface tension and inter-molecular forces, respectively. Therefore, the thin film evaporation region, which occupied only 20% of the total liquid meniscus areas, contributed to more than 80% of total heat transfer. Biporous evaporators with wider micropillar islands and narrower microchannels consisted larger number of micropillars. Thus, the total thin film evaporation regions were also larger. This resulted in more effective heat transfer and larger heat transfer coefficient.

5.3.2. Uniform vs. Biporous Evaporator

The experimental measured and model predicted dryout heat flux values of biporous and uniform micropillar evaporators were plotted in *Figure 37*. Model predictions of dryout heat flux for biporous and uniform evaporators were calculated using *Equation (43)* and *Equation (14)*, respectively. Error bars for model predicted dryout heat flux were calculated from the deviations in evaporator geometries measured by SEM and discrepancy between modeled and curve fitted $f(\frac{w}{i}, \frac{h}{i})$.

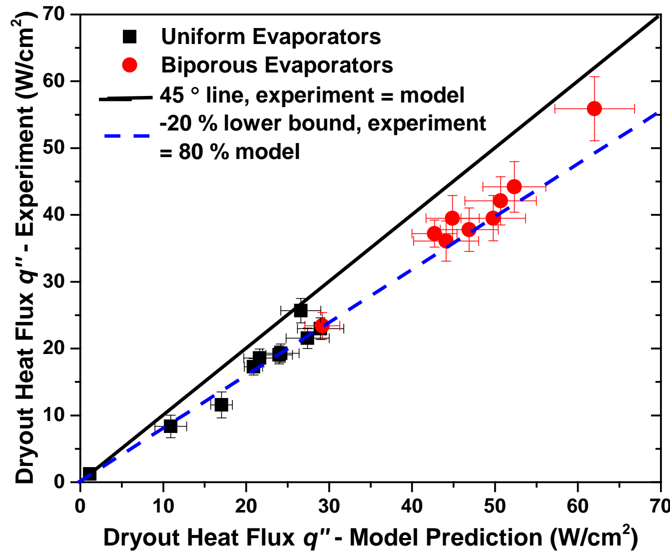

Figure 37:Dryout heat flux of uniform evaporators (black square dots) and biporous evaporators (red round dots): experiment measured vs. model predicted dryout heat flux

It can be concluded from *Figure 37* that the dryout heat flux model predicted the performance of evaporators well with deviation less than 20%. Calculations based on semianalytical models overestimated the actual dryout heat flux. Reasons for the overestimation and deviations were explained as follows. Capillary pressure was calculated using the thermodynamic model of Xiao *et al.* [70], in which a roughness factor was included $rf = \frac{\pi}{2}$ to account for the scallop structures created by cyclic process of DRIE. Additional energy terms were also included in *Equation (15)* to account for the energy change due to the wetting of roughness micropillar sidewalls. However, the

thermal characterization experiments were carried out at steady-state conditions after the formation of liquid meniscus. Thus, the actual steady state was over-predicted by *Equation (15)* as the roughness of micropillar sidewall did not have a profound effect on capillary pressure.

Moreover, a uniform evaporation was assumed in developing the analytical model, while in actual case the liquid film thickness varies along the entire interface [115]. Thus, the thin film evaporation rate was not identical along the evaporator wick surface. Lastly, assumptions of flat liquid meniscus and negligible heat transfer inside microchannels were made. Despite the relative evaporation areas within microchannels in comparison with that in between of large number of micropillars, evaporation existed and contributed to the total heat transfer. Therefore, the overestimation of capillary pressure by thermodynamic approach, simplified assumptions of uniform evaporation, flat meniscus curvature inside microchannels and ignorance of heat transfer within microchannels all led to the deviations between model and experiments. In general, an accurate semianalytical model that captured the dryout heat flux of biporous evaporators with a deviation of less than 20% was constructed.

Biporous evaporators performed superior to uniform evaporators in terms of higher dryout heat flux as shown in *Figure 37*. The dryout heat flux of biporous evaporator is around 1.5-2 times larger than that of the uniform evaporators tested. This was attributed to the existence of microchannels that served as local liquid reservoir to supply working fluid and compensate the evaporated liquid. According to *Figure 38 (a)*, dryout was initiated in the middle of micropillar islands, which was the small regions with brighter colors. This was because the center of micropillar islands had the longest propagation distance and highest viscous resistance for the liquid. The expansion of dryout region on biporous evaporators was relatively slow, the dry area increased from around 1.2% to around 2% of total wick area after 100 s. In contrast, dryout area on uniform evaporators expanded very rapidly after the onset of dryout as shown in *Figure 38 (b)*. After 1s of dryout inception, around 20% evaporator wick area was not covered by liquid. This area was increased rapidly to almost 75% after only 17.4 s. This led to a drastic rise of sample temperature and sharp decrease of heat transfer coefficient according to our previous

work [116]. Therefore, the biporous outperformed uniform evaporators in terms of dryout heat flux and performed better after the onset of dryout due to the slower dryout area expansion rate.

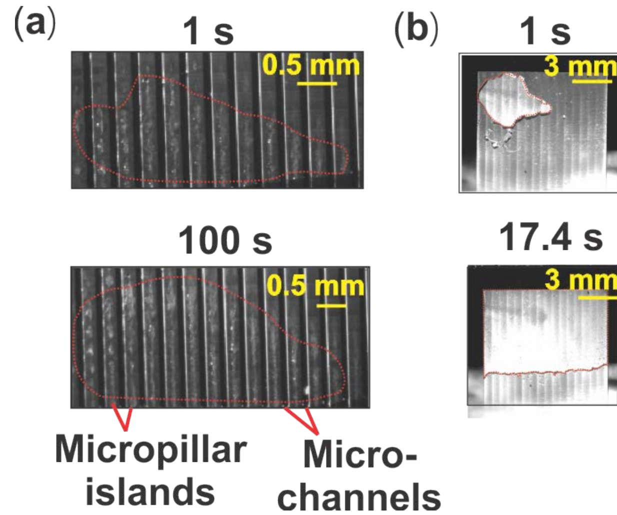

Figure 38:High speed camera images of dryout on evaporator samples (a) 1s and 100s after dryout of biporous evaporator sample (b) 1s and 17.4s after the onset of dryout on uniform evaporator sample.

In comparison with the micropillar evaporators in previous studies, the uniform micropillars can dissipate a maximum heat flux of 300 W/cm^2 with a heater size of 0.2 cm $\times$ 0.2 cm and a wicking length of 0.87 cm as proposed by Cai *et al.* [97]. This can be converted to a maximum heat load of 12 W, which is only 17.5 % – 46.5 % of the performance for our uniform micropillar evaporators as discussed in *section 5.1.4*. The uniform Si micropillar evaporator fabricated by Miers *et al.* [98] can dissipate a maximum heat load of 7 – 13 W, which is also much lower than our uniform evaporators. The uniform evaporator of Adera *et al.* [75] can dissipate a high heat flux of 46 W/cm^2, however, the wicking length was only 0.5 cm compared to our long wicking length of 1 cm. Therefore, our uniform micropillar based Si evaporators could dissipate high heat fluxes prior to dryout in comparison with the literature reported results. Moreover, there were a few studies on Si base biporous evaporators. With segmented Si micropillar structures and the uniform micropillar structures integrated with a screen mesh, Ravi et

al. [96] dissipated a heat load of 3.5 – 14.5 W. Coso *et al.* [60] prepared biporous evaporator samples with square micropillars separated by microchannels. For a micropillar array size of 1 cm × 1 cm, the evaporator could dissipate a maximum heat flux of 160 W/cm^2 with a heater size of 0.25 cm × 0.25 cm. This corresponded to a maximum heat load of 10 W. In this thesis, a maximum heat flux of 55.9 W/cm^2 can be dissipated for a 1 cm × 1 cm biporous evaporator with a 1 cm × 1 cm heater. Therefore, a critical heat load of 55.9 W can be achieved, which is superior to the biporous evaporators reported in the literature.

5.3.3. Biporous Evaporator Optimization

Owing to the competing effect between shorter liquid propagation distance and less thin film evaporation areas for smaller micropillar island width, and the converse relationship between smaller pressure drop and smaller evaporation areas for larger microchannel width, optimal geometries of 2*i* and 2*w* that can result in highest dryout heat flux of biporous evaporators existed, as discussed in *section 5.3.1*. Thus, the semianalytical model that has been validated against experimental results can be used for optimization of biporous evaporator geometries. *fmincon* module in *Matlab* was adopted with the geometric constraints $h/l > 1$ and $d/l < 0.57$ as *Equation (15)* and *Equation (19)* valid within these geometric ratio ranges, respectively. Temperature rise of biporous evaporator was also a significant parameter in evaluating the heat transfer performance of the evaporator. Therefore, optimization was conducted within superheat range of (5 – 30 °C) and the superheat was related to dryout heat flux of biporous evaporator with the following equation:

$$q''\frac{i+w}{i} = k_{eff}\frac{\Delta T}{h} \tag{55}$$

where $k_{eff} = 6.02633(\frac{d}{l})^2 - 3.19508\frac{d}{l} + 2.12324$. Temperature-related thermos-physical properties (ρ_l, h_{fg}, μ and σ) of water were used in the optimization. Water temperature was calculated as the average between sample temperature and ambient saturation temperature (25 ℃).

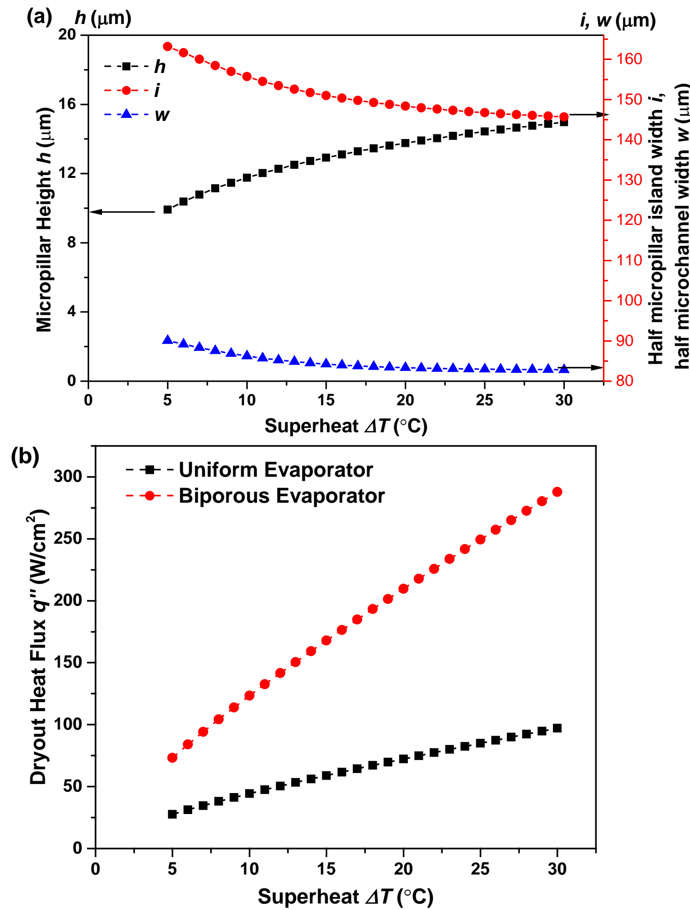

Figure 39:(a) Geometric optimization results (micropillar height h, half micropillar island width i and half microchannel width w) of biporous evaporator for an allowable superheat range of 5 – 30 ℃ (b) Dryout heat flux comparison between biporous and uniform evaporators with superheat range of 5 – 30 ℃

With a receding contact angle of 10˚, total wicking length $L = 1$ cm, the lower bound and upper bound of d, h, l, i, w were set to be 3, 6, 6, 10, 10 and 100, 100, 100, 500, 2000 with a unit of μm, the optimized micropillar diameter $d = 3.42$ μm and $l = 6$ μm. Optimal h, i and w varied with allowable superheat, the results were plotted in *Figure 39*.

As shown in *Figure 39 (a)*, optimal micropillar height increased with superheat, since the volumetric liquid flow rate was larger for taller micropillars. Viscous drag from the substrate was also less profound for taller micropillars. However, the larger height of micropillars led to an increase in thermal resistance and fabrication difficulties of the

evaporator wick. The optimization results can serve as useful design guidance for the selection of biporous evaporator geometries. The dryout heat flux of biporous and uniform evaporators at a certain allowable superheat were compared in *Figure 39 (a)*. It can be observed that biporous evaporator can dissipate larger heat flux prior to dryout, as the presence of microchannels as local liquid reservoir largely shortened the liquid propagation distance and was effective in delaying dryout.

5.4. Summary

In this chapter, the thermal characterization results, optimization and model validation of uniform micropillar evaporator, silicon vapor chamber with uniform evaporator and biporous evaporator were discussed.

Firstly, the high-speed camera images of droplet wetting and liquid propagation on microstructured surfaces have shown that the microengineering of silicon surface made it superhydrophilic to transport liquid rapidly in an automatic manner. Micropillars of uniform evaporator with 1D liquid propagation were optimized with dryout superheat constrain. By comparing the thermal performance of uniform evaporators with various micropillar geometries, the evaporator with optimized of d = 23.4 µm, h = 39.5 µm, l = 41.0 µm could dissipated the highest heat flux of q'' = 25.7 W/cm^2 before dryout. The heat transfer coefficient was found to increase with higher d/l ratio and shorter micropillars, which can be explained by the increase of thin film evaporation area and thermal conductivity with larger d/l ratio and smaller h. The dryout heat flux model were validated against experimental results with < 20% deviation. The deviation was mainly originated from the overestimation of capillary pressure.

After that, sealed silicon vapor chamber with uniform micropillar was optimized. Micropillars in the uniform evaporator section were optimized for heat transfer, and the optimal geometries were d =17.4 µm, h = l =30.6 µm at ΔT = 15℃. While the optimal geometries for the adiabatic region was d =15 µm, h = l =30.6 µm with larger porosity to facilitate liquid propagation. The silicon vapor chamber with optimized micropillar structures and 2D liquid flow was capable in dissipating a maximum heat flux of q'' = 98.1 W/cm^2 without dryout. Excellent response and temperature uniformity have been

demonstrated by the silicon vapor chambers, with a maximum temperature difference of 9.64 K at 98.1 W. Our silicon vapor chamber performed superiorly in terms of lower temperature difference and higher achievable heat load.

Lastly, parametric studies were also done on biporous evaporators with micropillar arrays separated by microchannels. Based on the parametric study result, a competing effect between shorter liquid propagation distance and smaller evaporation area existed when the micropillar island became narrower. Similarly, the smaller pressure drop and reduction of thin film evaporation area were also conversely related. The biporous evaporator could remove a maximum heat flux q'' = 55.9 W/cm^2 with $2i$ =202 µm and $2w$ = 117 µm. Biporous evaporators were proven to dissipate 1.5 – 2 times higher heat flux compared to that of uniform evaporators, owing to the existence of microchannels that shortened the liquid propagation distance and delayed dryout area expansion. Model validation and optimization of biporous evaporators were also conducted at various dryout superheats.

Chapter 6: Heat Transfer Suppression on Microengineered Surfaces

6.1. Background

The heat transfer capabilities and liquid transportation behavior for silicon surface with microengineered structures before dryout were studied and discussed in detail in the previous chapters. The microengineered surfaces were found to facilitate heat transfer prior to and just after dryout due to the large thin film evaporation areas, large permeability and capillary pressure of the micropillar arrays as discussed. Thus, micropillared surfaces were proven to be excellent candidates for vapor chamber evaporators. The feasibility of utilizing micropillar surfaces in other cooling techniques, such as spray cooling and jet impingement cooling, has not been examined. These cooling techniques involved liquid droplets in contact with a superheated surface, thus the droplet dynamics on superheated microengineered silicon surface is still of great interest. According to previous literature, when a droplet is dispensed on a hot surface with temperature slightly larger than the saturation temperature of the liquid, nucleate boiling will occur, and the liquid droplet evaporates rapidly. This is favorable in the cooling of high heat flux components, such as jet impingement cooling, owing to the high heat transfer coefficients associate with nucleate boiling. However, a contrary phenomenon was observed where liquid droplets were lifted by a vapor layer beneath them when the temperature of the surface was increased further. Instead of vigorous boiling with high heat transfer rate, the heat transfer was suppressed by the formation of liquid droplets and vapor barrier layer beyond a certain temperature. This phenomenon was termed as "Leidenfrost effect", which was first discovered by Boerhaave [117] in 1732 and was named after Leidenfrost [118] in 1756.

Leidenfrost effect refers to the phenomenon when a droplet encounters a surface that has the temperature significantly larger than the saturation temperature of the liquid. In this case, the liquid at bottom of the droplet evaporated very rapidly to form a vapor layer that suspends the droplet from the hot surface and inhibits heat transfer. The heat transfer rate of the droplet is largely reduced, and the droplet has very high mobility due to the minimal contact with the hot surface. The surface temperature at which the heat transfer is minimum and droplet lifetime is longest, is defined as Leidenfrost temperature [119].

Leidenfrost effect is not desirable in the metal quenching during metallurgical process, cooling of overheated components and nuclear reactors, but is of great importance in drag reduction applications which can induce up to 85% reduction of hydrodynamic force [120]. Thus, Leidenfrost effect and Leidenfrost temperature were widely studied by many researchers, so that Leidenfrost effect can be avoided or delayed in cooling applications and promoted in drag reduction applications.

The measured Leidenfrost point on flat Si surface was reported to be 200 – 390 ˚C[121 – 124], while that of stainless steel surface with 1.88 mm diameter water droplet was measured to be 290 ˚C according to literature [125].There are a few factors that can affect the Leidenfrost temperature, which include surface chemical factors (surface energy, hydrophobicity and composition), thermophysical properties of liquid/solid interface (density and thermal resistance), especially topographic properties of the surface (nanoengineering and microengineering of surface, surface roughness modification *etc.*). The hydrophobicity alteration can be achieved through surface treatment, surface coating, cleaning or surface engineering. Surface engineering/ texturing can make the inherent hydrophobic surface more hydrophobic and hydrophilic surface more hydrophilic, according to the Wenzel relation expressed by *Equation (52)*. Vakarelski *et al.* [120] studied the Leidenfrost effect on hydrophilic, hydrophobic, superhydrophobic and superhydrophilic stainless steel surfaces, which were produced by organic reagents cleaning, silanization using trichloro silane, treatment with coating agent and plasma cleaning of the hydrophobic coating, respectively. The smooth hydrophobic surface was proven to stabilize the vapor layer at lower temperature, while the textured superhydrophobic surface can prevent nucleate boiling and achieve vapor layer stabilization at all temperature. Wetting regimes of water droplets on flat and smooth hydrophobic and hydrophilic surfaces were investigated by Liu and Craig [126]. Droplets resided on fluorinated SiO_2 coated GaAs surface demonstrated three different regimes, namely vigorous boiling regime with decrease of contact angle, superhydrophobic regime with decrease wettability and Leidenfrost regime. In contrast, no wetting transition was observed on hydrophilic Au and GaAs surfaces up to Leidenfrost regime. The Leidenfrost transition was observed at 210 ˚C and 280 ˚C for hydrophobic and

hydrophilic surface, respectively. The effect of microstructure height, wettability and nanoporous layer on the Leidenfrost point of Si was studied by Kim *et al.* [121]. The Leidenfrost point increased significantly by around 189 ˚C with the deposition of 600 nm SiO_2 nanoparticles, which can be explained by the easier bubble nucleation on nanoporous layer that disturbed the formation of stable vapor film. In addition, the existence of microposts consistently enhanced the Leidenfrost point due to the enhance in wettability and hydrophilicity. Significant Leidenfrost point increase of 175 ˚C was also observed by Kruse *et al.* [127] by modifying the stainless-steel surface with laser machining, which made the surface more hydrophilic with nanoporous layer deposited and intermittent contact between the droplet and surface was induced. Duursma *et al.* [124] patterned the Si surface with various micropillar structures, and obtained a Leidenfrost point enhancement of up to 120 ˚C by changing the micropillar spacing from 10 to 100 μm. The droplet that was placed at the edge of two areas with different micropillar geometries was found to rotate due to the oscillation in supporting vapor film. Similarly, the Leidenfrost point variation of – 10 to 90 ˚C was demonstrated by the silicon micropillar surface compared to plain Si surface according to Park *et al.* [128]. Leidenfrost effect was even suppressed at very high temperature of around 570 ˚C by creating a hierarchical surface with 300 nm Au nanomembrane suspended above 95 μm tall Si micropillars.

Based on the foregoing research, it can be concluded that surface engineering has a profound effect on the Leidenfrost point by changing the surface wettability [120 – 128]. Leidenfrost point was found to increase with increase hydrophilicity and decrease contact angle of a surface in general, where the increase of hydrophobicity or increase of contact angle has the reverse effect. Typical Leidenfrost point increase of 30 – 190 ˚C and Leidenfrost point reduction of around 100 ˚C were demonstrated by making the surface more hydrophilic and hydrophobic respectively. Manipulation of micropillar geometries can also change the Leidenfrost temperature. However, non-wetting droplets were observed at a temperature much lower than the Leidenfrost point on superhydrophilic Si micropillar structures by Adera *et al.* [129]. The existence of non-wetting droplets at low superheat can be explained by the increase of thermal conductivity for the porous

micropillar layer beneath the droplet, which induced rapid evaporation and stabilized the vapor film at low superheats (5 – 50 K). Adera *et al.* [129] studied the transition from nucleate boiling to non-wetting droplets and constructed a model to correlate the transition temperature to micropillar geometries. Although the systematic investigations on this transition temperature were done, the study of droplet regimes was not extended to higher temperature and Leidenfrost state. Dual peak for droplet lifetime may exist at the transition non-wetting regime and Leidenfrost regime, respectively. Systematic parametric study for the effect of micropillar geometries (d, h, and l) on the transition temperature and Leidenfrost temperature is not established yet. Therefore, we would like to conduct research to explore the droplet behavior over a wider temperature range and prove the existence of dual peak for droplet lifetime. The effect of micropillar pitch l and height h on the lifetime and transition temperature of the droplets will also be investigated.

6.2. Experimental Methods

6.2.1. Sample Preparation

Table 11: List of samples with various micropillar geometries for droplet behavior study

Sample Number	d (μm)	h (μm)	l (μm)
A	–	–	–
B	6.0	21.3	20
C	6.0	21.3	30
D	6.0	21.3	50
E	36.4	38.3	80
F	36.4	38.3	110
G	36.4	38.3	120
H	36.1	27.4	120
I	35.8	74.9	120

The microengineered surfaces were prepared with standard silicon fabrication process followed the *step 1 – 5* illustrated in *Figure 12*. The silicon micropillars with various geometries were defined by photolithography and deep reactive ion etching (DRIE). The geometries of tested samples are listed in *Table 11*. The micropillar geometries were measured by SEM and averaged from 10 readings. *Sample A* refers to plain Si surface,

while *sample B – D* and *E – G* have different micropillar pitch, *sample G – I* have different micropillar heights.

SEM images of the tested samples with different micropillar geometries are shown in *Figure 40*. The samples have the same micropillar diameter d and h, while l varies to make the micropillar structures more dense or sparse. Prior to the droplet behavior tests, the microengineered surfaces were cleaned by immersing in acetone, IPA and DI water for 10 mins each, followed by 15 mins plasma cleaning. After that, the samples were left in open ambient for 1 hr to restore the wettability to its intrinsic state.

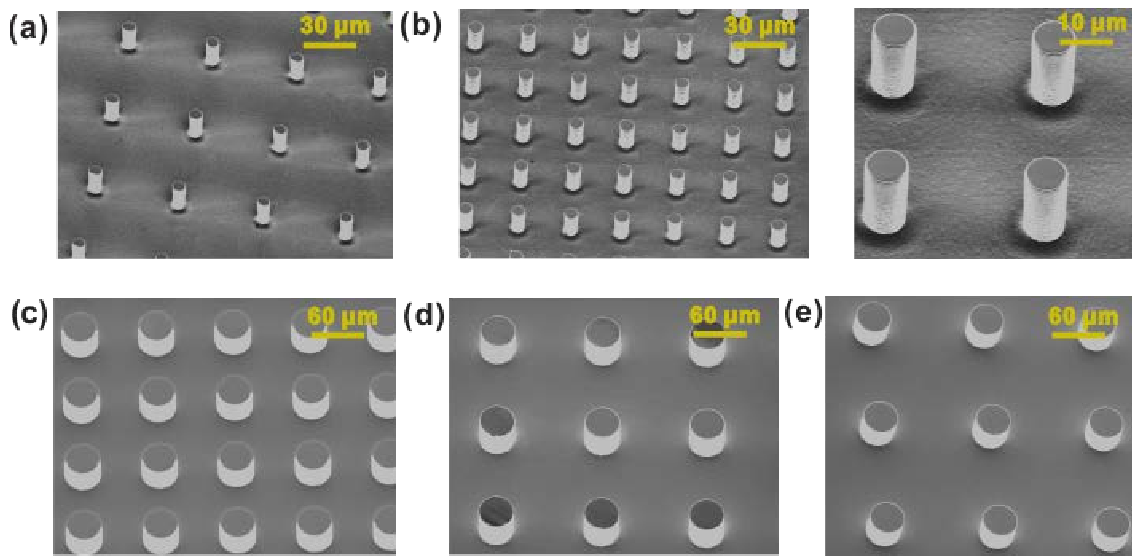

Figure 40: SEM images for the droplet behavior test samples with various micropillar geometries (a) Sample D and (b) Sample C with the same d and h, while l varies from 50 to 30 µm (c) Sample E (d) Sample F and (e) Sample G with the same d and h, while l varies from 80, 110 to 120 µm

6.2.2. Tests

The experimental setup is illustrated in *Figure 41*. The microengineered surface samples were kept on a thick 10.3 cm × 4.8 cm × 2 cm copper block which was heated by a hotplate (*HP88854100, Thermo Scientific*). The thick copper block was adopted to promote better temperature uniformity and prevent localized cooling of the substrate surface, as copper has excellent thermal conductivity. The initial hotplate temperature

was set to be 100 ˚C, and gradually increased to 540 ˚C with 15 ˚C temperature increment. Actual surface temperature of the copper block was measured by three type-K thermocouples (*L-0044T, Omega*). The temperature readings were recorded by data acquisition (DAQ *34972a*, *Keysight*) system. Steady state surface temperature was achieved once the temperature readings varied within 1 ˚C. At each steady state, 10 DI water (*Sigma-Aldrich*) droplets with constant volume of 10 µl, which corresponded to a droplet radius of 1.34 mm, were dispensed by a micropipette (*YE6A820078, Shcheer*) with accuracy of 0.5 µl. This droplet size was chosen to be smaller than the capillary length of water, which can be calculated as $\sqrt{\sigma / \rho_l g} = 2.5$ mm. In this case, the droplet with radius < 2.5 mm can reside on the surface with nearly spherical shape at Leidenfrost state [123]. Ambient conditions for the experiments were ~ 0.998 atm at ~ 22 ˚C room temperature with relative humidity level of ~ 80%.

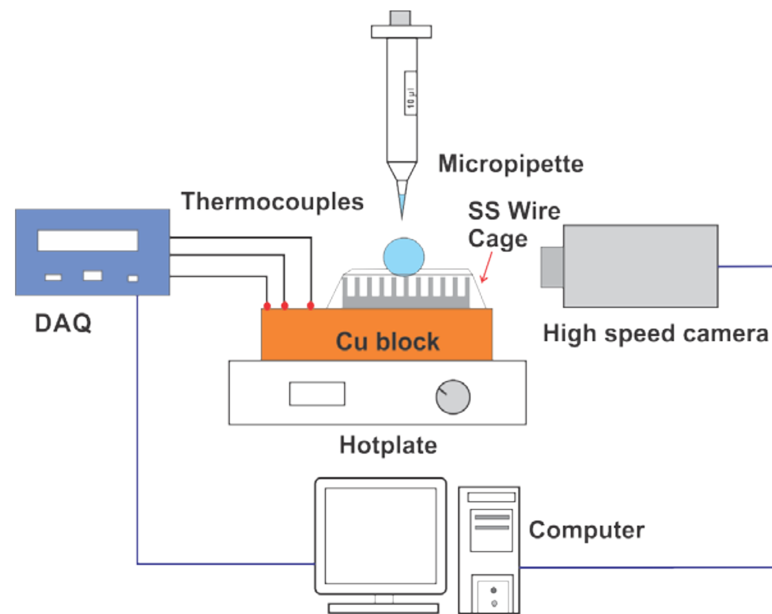

Figure 41: Schematic illustration of experimental setup for droplet lifetime measurement (not to scale): The micropillar structured surfaces were heated by a hot plate with a thick copper block. Droplets with constant volume of 10 µl were dispensed by micropipette on the superheated micropillar surface with stable temperature. Droplet lifetime was captured by high speed camera, while the surface temperature was measured by three K type thermocouples.

The droplets have very high mobility at Leidenfrost state due to the large reduction of friction by the presence of vapor layer. Thus, the droplet movement should be constrained within the high-speed camera viewing area in order to measure the droplet life time. This was achieved with a square wire cage that was made by fixing four functionalized 50 μm diameter stainless-steel wires (*1/16, Malin Co.*) with Kapton tape. Functionalization was done by cleaning the wires with ethanol, water and plasma treatment inside plasma cleaner (*PDC-001, Harrick Plasma*) first. After that, the wires were immersed in 1 mMol TFTS (Trichloro (1H, 1H, 2H, 2H-perfluoro-octyl) silane, *MKBV0653V, Aldrich*) hexane (*SHBH1930V*, *Sigma-Aldrich*) solution and heated to 60 ˚C for 1 hr. Then the wires were rinsed by ethanol and water, respectively, followed by drying of the wires at 120 ˚C on a hotplate for 1 hr (*HP88854100, Thermo Scientific*). Superhydrophobic stainless-steel wires with contact angle > 160 ˚ were obtained after functionalization process, thus the surface tension effect by the wires was minimized by making it superhydrophobic. State of each droplet was captured by the high-speed camera (*V7.1, Phantom*). Droplet lifetime was calculated based on the time elapsed when the droplet first touched the superheated surface and when the droplet completely diminished due to evaporation or boiling. Lifetime of 10 droplets were measured and averaged at each temperature value to make the result statistically reliable.

6.3. Droplets Behavior on Various Surfaces

The test results were plotted as droplet lifetime versus temperature curves for flat Si surface and microengineered surface with $d = 6$ μm, $l = 20$ μm and $h = 21.3$ μm as shown in *Figure 42* and *Figure 43*, respectively. Droplet lifetime was calculated based on the average of 10 measurements, while the error bars represent the standard deviations of the readings. Temperature values were averaged from the readings of three thermocouples. According to *Figure 42*, droplet behavior can be divided into three regimes, namely the nucleate boiling regime, transition regime and Leidenfrost regime. At nucleate boiling regime, the droplet lifetime decreased from 16.9 s to 0.24 s when temperature increased from 104 ˚C to 254 ˚C. The reduction of droplet lifetime with temperature can be explained by the increased heat transfer rate due to more vigorous boiling at higher

temperature, which accelerated the evaporation rate of the life time and reduced the lifetime. The nucleate boiling of droplet was captured by the high-speed camera and is shown on the left in *Figure 42*, the boiling was accompanied by severe liquid splashing as well as bubble formation and bursting. When the temperature was increased further to 264 ˚C, a sharp increase of droplet lifetime to 28.1 s was observed, and the droplet behavior translated to a transition stage. There was a combination of nucleate boiling and Leidenfrost state of droplet with droplet jumping at this regime, as shown in the high-speed camera images in *Figure 42*.

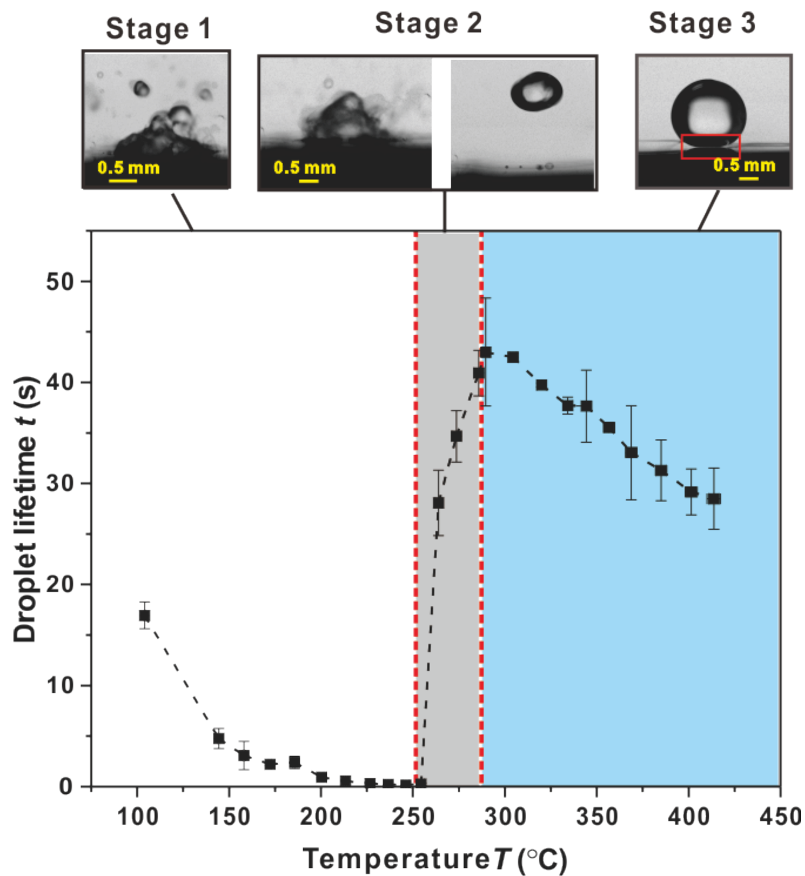

Figure 42: 3 stages for water droplets encountered a superheated plain silicon surface: stage 1 – vigorous boiling stage with droplet lifetime decrease with temperature, the high – speed camera image was captured at 225 ˚C; stage 2 – transition stage between nucleate boiling and Leidenfrost state, image was taken at 255 ˚C; stage 3 – Leidenfrost state with droplet suspended by a vapor layer, image was obtained at 300 ˚C

Droplet size was found to affect the Leidenfrost point, where a droplet with smaller radius required lower temperature for Leidenfrost effect [123]. Thus, when the droplet was initially dispensed onto the hot surface, the vapor generation rate was not rapid enough to form enough vapor layer that can support the entire droplet. Vigorous boiling with liquid splashing was observed first. As the droplet sized decreased due to boiling, the vapor layer generated by boiling could support the smaller droplet to suspend above and around on the microengineered surface. When the surface temperature was further increased, the droplet lifetime kept increasing until it peaked at around 290 ˚C. Thus, the measured Leidenfrost point for flat Si was 290 ˚C, which was in good agreement with previous literature [121 – 124]. The droplets were at Leidenfrost state with a vapor layer to suspend the droplets to move around on the surface from the moment when the droplet touched the surface. The vapor layer can be identified by the light transmitted under the droplet, as shown in the image of *Figure 42* for droplet at stage 3. Beyond the Leidenfrost point, the droplet lifetime decreased with temperature, as high temperature induced a faster evaporation of the droplet. Therefore, the droplet on a flat Si surface can be divided into three regimes, with the longest lifetime of the droplet occurred at Leidenfrost point. In contrast, there were five regimes for droplets on superheated microengineered surface as shown in *Figure 43* with d = 6 μm, l = 20 μm and h = 21.3 μm. Nucleate boiling of water droplets was also observed on microengineered surface initially. The same as the case when a droplet was dispensed onto a flat Si surface, the droplet lifetime decreased with temperature in the nucleate boiling regime. However, abrupt lifetime increases at 164 ˚C was observed for droplet on microengineered surface, which is much lower than the 264 ˚C for that on flat Si surface. There was a combination of nucleate boiling and non-wetting state of droplets at this transition regime. The droplet can reside on top of the microengineered surface with the bottom of the droplet in contact with the top of micropillars. This Leidenfrost-like non-wetting state of droplet was originated from the presence of porous micropillar media beneath the droplet, which increased the effective thermal conductivity of the gap in between of the droplet and the substrate. Moreover, the vapor permeability was also lower in micropillar structure due to the viscous loss at

the sidewalls of micropillars. The existence of the micropillars hindered the escaping of generated vapor and facilitated the formation of vapor layers.

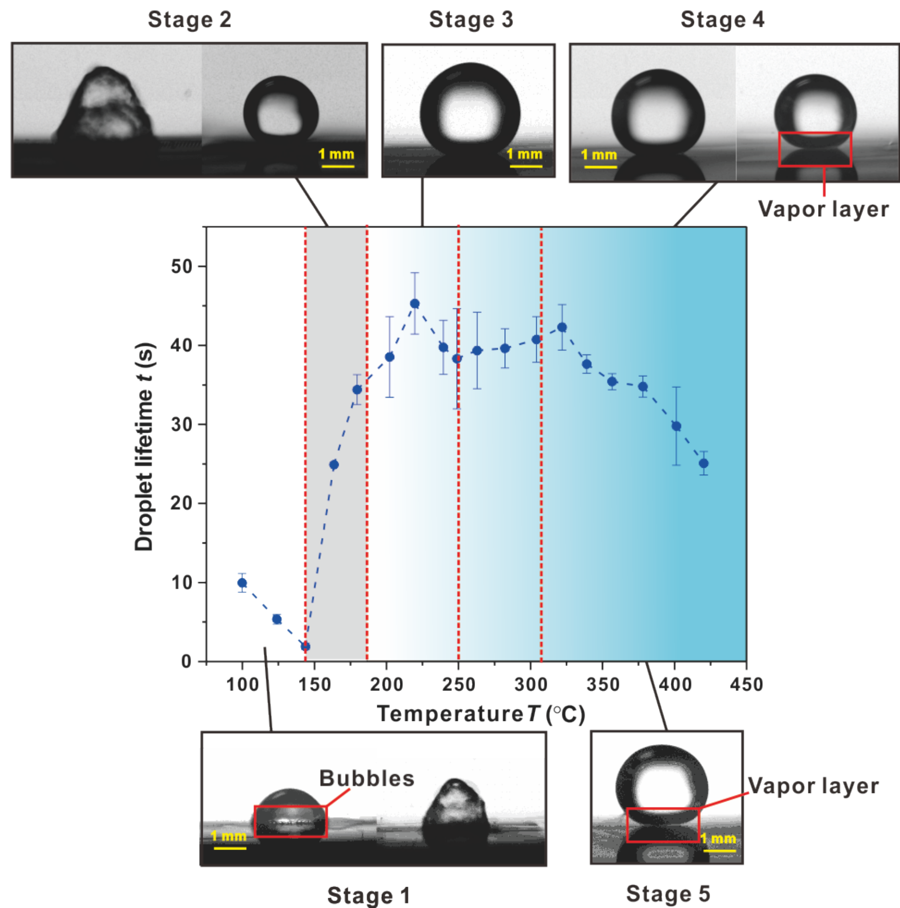

Figure 43: 5 stages when water droplets encountered a superheated microengineered Si surface with micropillar structures. The sample presented was sample B. Stage 1: vigorous boiling, pictures captured at 144 ˚C; Stage 2: first transition regime between boiling and non-wetting stage, image took at 180 ˚C; Stage 3: non-wetting stage, droplet did not wet the superhydrophilic surface, instead it rested on top of the microengineered surface and was in contact with the micropillar tops, picture obtained at 220 ˚C; Stage 4: second transition regime between non-wetting and Leidenfrost state, droplet was in contact with micropillars at first, and then levitated by a vapor layer to suspend above the surface when it became smaller due to evaporation at 282 ˚C; Stage 5: Leidenfrost state with suspended droplet supported by a vapor layer at 357 ˚C

Therefore, the higher effective thermal conductivity and lower vapor permeability promoted the vapor generation and vapor layer formation. Thus, the droplet was lifted

by the vapor layer to stay as non-wetting drops on top of the micropillars, with the bottom touching the micropillar tips. Detail explanations can be found in [129]. The first peak of droplet lifetime was obtained at 220 ˚C, where the droplet was at non-wetting state without nucleate boiling.

The non-wetting state with droplet bottom in contact with the micropillar top, followed by Leidenfrost state with a vapor layer to elevate the droplet, was observed at higher temperature. This is termed as the second transition regime, at which the vapor generation rate was not rapid enough to support the 10 µl droplet at initial dispense. After that, a clear vapor layer gap can be observed according to the image in *Figure 43* stage 5. The Leidenfrost point for the microengineered surface was determined to be 322 ˚C, which is higher than that on flat Si surface and is the second peak for droplet lifetime. This was attributed to the intrinsic superhydrophilic characteristic for microengineered Si surface, which resulted in an increase in Leidenfrost point according to literature. In general, the longest droplet lifetime, which corresponded to the minimal heat transfer rate, was obtained in the non-wetting regime. Dual peaks of droplet lifetime were demonstrated by droplets on microengineered surface. As the minimal heat transfer rate on microengineered surface occurred at a temperature much lower than the Leidenfrost point of flat Si surface, microengineered surface was not recommended to be adopted in cooling applications such as spray cooling and jet impingement cooling. This agrees with the conclusion of Adera *et al.* [129], but in contradiction to some of the previous literature [120 – 128].

6.4. Parametric Studies

Wetting tests on microengineered surfaces with different micropillar geometries (*d*, *h* and *l*) were conducted. The measured droplet lifetime versus temperature graphs for *sample A – I* were plotted in *Figure 44 (a) – (c).* According to the results shown in *Figure 44 (a)* for *sample B – D* with the same *d, h* and *l* increased from 20 to 50 µm, the transition

temperature increased from 164 ˚C to 194 ˚C, while the Leidenfrost temperature increased from 322 ˚C to 349 ˚C with larger *l*.

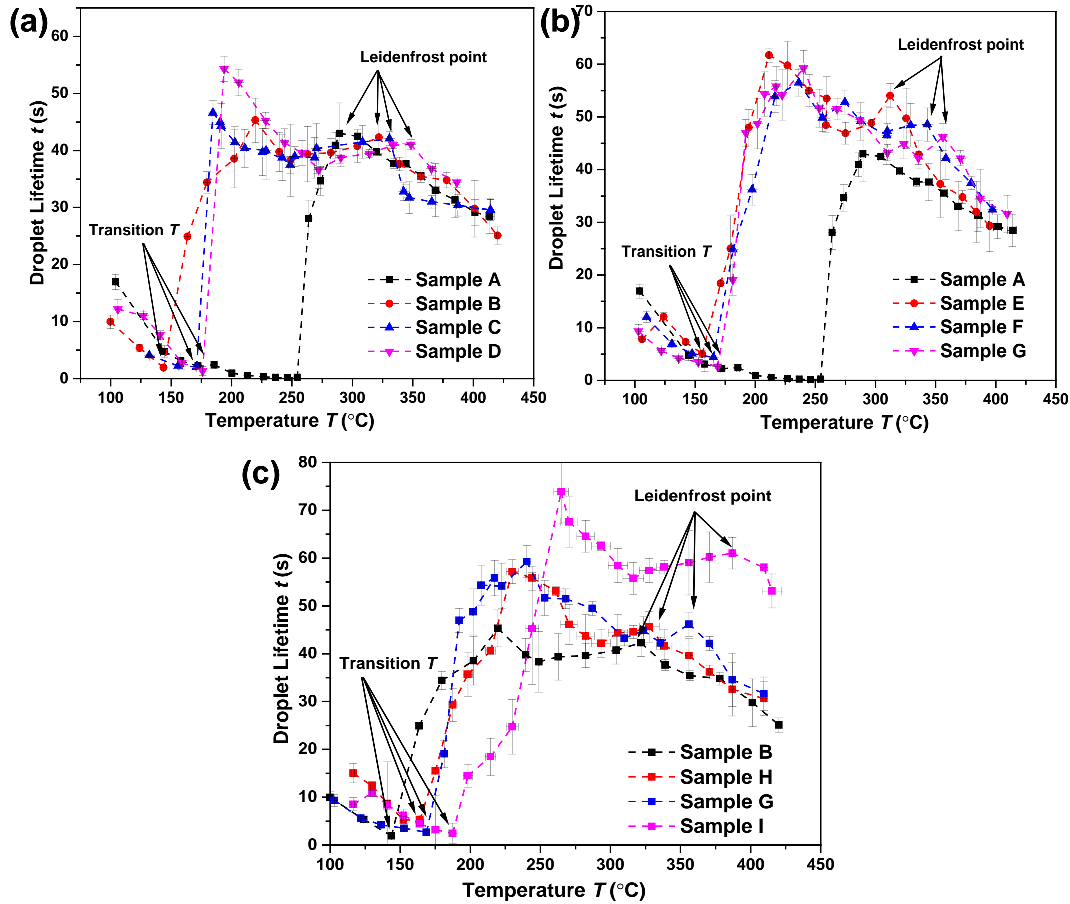

Figure 44: Lifetime of droplets at different temperature for microengineered surfaces with various geometries and flat Si surface (sample A). (a) Effect of l: sample B – D have h = 21.4 µm, d = 6 µm and l ranges from 20 to 50 µm (b) Effect of l: sample E – G with h = 38.3 µm, d = 36.4 µm and l ranges from 80 to 120 µm (c) Effect of h: sample B and sample G – I with the same solid fraction of 0.07 and various h of 21.3, 27.4, 38.3 and 74.9 µm. The transition temperature from boiling to non-wetting regime and the Leidenfrost point were indicated by the arrows. Both transition temperature and Leidenfrost point were found to increase with higher l and larger h.

The same trend was observed for *sample E – G*, where *l* increased from 80 to 120 µm with constant *d* = 36.4 µm*, h* = 38.3 µm, transition temperature and Leidenfrost point increased from 171 ˚C and 312 ˚C to 183 ˚C and 356 ˚C, respectively. When the solid fraction of micropillar arrays was kept as 0.07 and micropillar height *h* increased from

21.3, to 27.4, 38.3 and 74.9 μm, the transition temperature and Leidenfrost point also increased from 164 ˚C and 313 ˚C (*sample B*) to 198 ˚C and 387 ˚C (*sample I*) accordingly, as shown in *Figure 44 (c)*. The droplets were observed to have dual lifetime peaks for wetting tests on microengineered surfaces, while only one peak was observed for that on flat Si surface. The longest lifetime for droplets on microengineered surfaces was obtained in non- wetting regime, instead of that in Leidenfrost regime on flat Si surface

Based on the trends observed in *Figure 44 (a) – (c)*, conclusions can be drawn that the intrinsically superhydrophilic surface can behave as superhydrophobically with water droplets sit on top of the micropillars at a temperature lower than Leidenfrost point. The transition and Leidenfrost temperature were geometric dependent, which increased with *l* and *h*. The microengineered structures under a non-wetting droplet were composed of micropillars and water vapor, which possesses much higher thermal conductivity than the vapor layer under a Leidenfrost droplet. This was attributed to the high thermal conductivity of Si micropillars where $k_{Si} \approx 100W / m \cdot K$ [130] compared to that of water vapor $k_{vapor} \approx 0.025W / m \cdot K$. The high thermal conductivity micropillar layer under the droplet led to faster vapor generation rate due to droplet evaporation. Moreover, as vapor was escaping from the porous micropillar media, a pressure gradient that suspended the droplet on top of the micropillars was resulted. Thus, the non-wetting force was originated from the high-pressure region below the droplet, which was a result of the fast evaporation from the droplet. Due to the inherent superhydrophilic property of the micropillar surface, the surface tension promoted wetting of the droplet and liquid/vapor meniscus concaved outward as shown in [129]. Together with the gravity of the droplet, the surface tension provided the wetting force to prevent the non-wetting stage of droplets. At a critical temperature where the wetting force overcomes the non-wetting force, the droplet appears to be non-wetting and can reside on top of the micropillars. This transition temperature T_{trans} from boiling to non-wetting regime for droplets on superheated microengineered surfaces can be evaluated with the following equation [129]:

$$T_{trans} = T_{sat} + 8\pi\left(\frac{\rho_{vap} h_{fg} \sigma \cos\theta}{\mu_{vap}}\right)\left(\frac{dhK(R_s + R_{evap})}{\varepsilon R_{base}^2}\right) \times \left(1 - \frac{\tanh(\frac{h}{2}\sqrt{\frac{\varepsilon}{K}})}{\frac{h}{2}\sqrt{\frac{\varepsilon}{K}}}\right) \quad (56)$$

where T_{sat} stands for the saturation temperature of the liquid, which is 100 ˚C at 1 atm. ρ_{vap} , μ_{vap} , h_{fg} and σ are the vapor density, vapor viscosity, latent heat of vaporization and surface tension for liquid-vapor interface at 100 ˚C, respectively. θ stands for the apparent contact angle on Si surface, which is 38˚ according to literature [131]. The second and third terms in the brackets are geometric dependent. ε , K, R_{base} R_s and R_{evap} are the porosity, permeability, base radius in contact with the micropillars, spreading resistance, evaporation resistance, respectively. Permeability of the micropillar structures can be calculated with *Equation (20)*. The spreading thermal resistance R_s is expressed by the following equation [129]:

$$R_s = \frac{-0.303(d/l) + 0.332}{k_{water}\sqrt{(\pi d^2/4)}} \quad (57)$$

The droplet base radius can be measured experimentally or estimated with the equation below:

$$R_{base} = R\sin\theta_{CB} \quad (58)$$

where R is the droplet major radius, which is around 1.3 mm in this experiment. θ_{CB} is the apparent Cassie-Baxter contact angle on a rough surface. θ_{CB} is correlated to θ with the following expression:

$$\cos\theta_{CB} = -1 + \frac{\pi d^2}{4l^2}\left(1 + (1 + \frac{\pi dh}{l^2})\cos\theta\right) \quad (59)$$

With identical thermophysical properties of water and water vapor at 100 ˚C, for micropillar structures with higher *l* and *h* while keeping the other two geometries as constants, the effective thermal conductivity for the porous micropillar regions was lower. For micropillar structures with constant *d* and *h*, increased *l* reduced the number of micropillars per unit area. As Si has much larger thermal conductivity compared to the vapor in between of the pillars, the effective thermal conductivity of the porous structure was much lower. Moreover, micropillar arrays with larger *l* corresponded to a higher

vapor permeability that facilitated vapor escaping. Therefore, higher temperature was required to generate enough water vapor and stabilize the vapor layer for micropillar structures with larger l. Similarly, with higher micropillar height at the same d and l, the effective thermal conductivity was also lower. The droplet lifetime was also much longer on micropillar structures with h = 74.9 μm for *sample I* compared to that with h = 21.3 μm for *sample B*. The microengineered structures with lower thermal conductivity hindered the vapor generation rate by evaporation, thus shifted the transition temperature to higher values. This can be verified by *Equation (56)* and the discussions in [129].

The Leidenfrost point (323 ˚C to 387 ˚C) for all the microengineered surfaces were larger than that on flat Si surface (290 ˚C), this can be explained by more heterogeneous bubble nucleation sites on microporous surfaces. The nucleation sites favored the formation of bubbles, and the vapor layer stabilization was disrupted by the bubble bursting [121]. Therefore, the Leidenfrost point was higher for microengineered surfaces compared to that on flat Si surface. A highest Leidenfrost point increment of 97 ˚C was obtained by adopting microengineered surface. Like the trend in transition temperature, the Leidenfrost point was found to increase with l and h as well, this agrees with the observation of Duursma *et al.* [124]. A correlation between Leidenfrost point on micropillared surface was obtained by Duursma *et al.* [124] and expressed as:

$$T_L = C_1 T_{Si} + C_2 (l - d) \tag{60}$$

C_1 and C_2 are fitted coefficients. T_L and T_{Si} are the Leidenfrost point on microengineered and flat surfaces, respectively. Therefore, the Leidenfrost point also increase with larger l.

It can be concluded that the transition temperature and Leidenfrost point increase with h and l. Although the microengineered Si surface can increase the Leidenfrost point up to 97 ˚C, it is not recommended to be used in extreme high heat flux applications such as spray cooling and jet impingement cooling. This is because the droplet wetting was prohibited at lower temperature on microengineered surface, especially for the surface with lower aspect ratio and smaller porosity. However, the microengineered surface could be a great candidate for drag reduction and corrosion prevention applications.

6.5. Summary

The droplet behavior at extremely superheated micropillar surfaces was examined in the chapter. The lifetime of ten 10 μl water droplets were measured on a microengineered surface heated with a hotplate. 3 regimes were identified for droplets on a flat Si surface, namely the nucleate boiling, transition and Leidenfrost point regimes. The longest droplet lifetime and minimal heat transfer was observed at the Leidenfrost point in Leidenfrost regime at 290 ˚C on flat Si surface. In contrast, there were 5 regimes for droplets dispensed on to a microengineered surface. The regimes were divided into nucleate boiling regime, first transition regime with boiling and non-wetting droplets, non-wetting regime, second transition regime with non-wetting and Leidenfrost droplets, as well as Leidenfrost regime. The droplet sits on top of the micropillars with the bottom of the droplet touches the micropillars in non-wetting regime, while suspends above the micropillars at Leidenfrost regime. The non-wetting droplet was observed at a temperature much lower than the Leidenfrost point of flat Si. This can be explained by the enhanced thermal conductivity and reduced vapor permeability for porous micropillar layer under the droplet, compared to the vapor cushion as on the flat Si surface. Two peaks of the droplet lifetime were obtained on microengineered surface, while only one peak was observed for flat Si surface. The minimal heat transfer rate was observed at the non-wetting regime, which occurred at a much lower temperature than the Leidenfrost point of flat Si.

Comprehensive parametric studies which examined the effect of micropillar geometries on the transition temperature and Leidenfrost point were conducted. Both the transition temperature from nucleate boiling to non-wetting regime, and the Leidenfrost point were found to increase with micropillar pitch l and height h. The reduced effective thermal conductivity was the reason for the transition temperature and Leidenfrost point shift on microengineered surface with various structures. This was also validated by previous model and studies. It is suggested that the microengineered surfaces can be adopted for drag reduction and corrosion prevention applications, instead of extreme high-heat flux applications.

Chapter 7: Conclusions and Future Work

7.1. Conclusions

Silicon vapor chambers have been recognized as reliable thermal management devices for dense and miniature electronic devices. This was evidenced from its superior heat removal capability, mature manufacturing technology, direct integration with electronic devices and elimination of thermal expansion mismatch risks. Evaporator is the key feature which dictates the critical dryout heat flux of the vapor chamber. Evaporator with uniform micropillar arrays was found to demonstrate high capillary pressure, large permeability and extended evaporation areas. In this thesis, a comprehensive study was conducted to model, optimize and thermal characterize uniform micropillar based evaporators, silicon vapor chamber with uniform evaporators and biporous evaporators with micropillar arrays separated by microchannels.

Semianalytical models in predicting the capillary limited dryout heat flux of uniform evaporator, silicon vapor chamber and biporous evaporators were developed. The three expressions in evaluating the dryout heat fluxes were obtained by solving Brinkman's equation based on the balance between capillary pressure and viscous resistance. A uniform heat flux, uniform and steady state evaporation were assumed in developing the models. Heat transfer and liquid meniscus of the microchannels were neglected compared to that of evaporation in micropillar arrays. The dryout heat flux of uniform/biporous evaporator and silicon vapor chamber depended on the thermophysical properties of working fluid, material properties of micropillars and geometries of micropillars.

The evaporator samples were fabricated on double polished 6-inch silicon wafers. The chrome masks used in patterning the evaporator structures were designed with *L-edit*. Front side of the uniform/biporous evaporators was composed of 1.5 cm × 1 cm uniform micropillar arrays with or without microchannels. The total area for evaporation was 1 cm × 1 cm while the extra 0.5 cm was left at the bottom to account for macroscopic meniscus and immersion. Height of the micropillars was etched by deep-reactive-ion-etching (DRIE). Thin film Pt heater with size of 1 cm × 1 cm and 4 RTDs were patterned on the backside of the evaporator samples with photolithography, e-beam deposition and

lift off. The metal layers were 180 nm Pt with 30 nm Ti as adhesion layer and 930 nm SiO_2 as insulation underneath. Sealed silicon vapor chambers were fabricated by bonding two silicon wafers with Au-Si eutectic bonding. The top wafer of the silicon vapor chamber had a 100 μm cavity as vapor space, one 1/8'' hole and one 1/16'' hole for liquid charging and evacuation, respectively. Bottom wafer of the silicon vapor chamber was composed of micropillar structures on the front side, Pt heater and RTDs on the backside. The evaporator area was 1 cm × 1 cm with 4 supporting posts at 4 corners. The evaporator was surrounded by adiabatic regions with micropillars. Total micropillar areas was 3 cm × 3 cm, while the fingerprint of the vapor chamber was 4 cm × 4 cm × 1.25 mm.

Thermal characterizations for evaporator samples were conducted inside a vacuum chamber, which was used to mimic the real working condition of actual vapor chamber. The evaporators were mounted onto a PCB and aligned vertically. Degassed deionized water was used as the working fluid and degassed by 3 cycles of freeze-pump-thaw processes. With gradual increment of applied heat flux via the heater, temperature of the evaporator was measured by the RTDs. Silicon vapor chamber was evacuated and charged with desired amount of degassed DI water prior to thermal characterization. After that, the silicon vapor chamber was subjected to increased heat loads and temperature of the vapor chamber was measured by the backside RTDs. Top condenser of the vapor chamber was cooled by a copper chiller and the condenser temperature was measured by 7 thermocouples. The RTDs of evaporators and silicon vapor chambers were calibrated inside an oven to correlate the resistance readings to temperature values. Uncertainties in the measured heat flux, superheat and heat transfer coefficient was calculated to be 8.10%, 9.79% and 0.114% ± 1.16℃, respectively.

Results of thermal characterization and parametric studies were also discussed and analyzed. *Matlab* optimization was conducted to find the optimal geometric combinations in maximizing the silicon micropillar based uniform evaporator dryout heat flux. The superheat constraint was applied during optimization process. Thus, geometries for micropillar evaporators that can dissipate large amount of heat while maintaining a reasonable temperature rise were obtained. Systematic parametric studies

in investigating the effect of micropillar *d/l* ratio and *h* were carried out. Uniform evaporator *sample 1* with optimized geometries d =23.4 µm, h = 39.5 µm and l = 41.0 µm performed best in terms of largest dryout heat flux q'' = 25.8 W/cm^2 at low temperature rise of ΔT = 4.9 ℃ and thermal resistance of 0.19 K/W. Heat transfer coefficient was found to increase with *d/l* ratio (larger *d* or smaller *l*) due to the high solid fraction and more thin film evaporation areas. Evaporator dryout heat flux was observed to increase with *h* while heat transfer coefficient had an inverse trend. The larger dryout heat flux with taller micropillars was explained by higher volumetric flow rate and lower viscous drag from the substrate. However, the thermal resistance and superheat increased with micropillar height, which limited the actual height of micropillar. Thus, the constraint with superheat during optimization was essential in ensuring a reasonable temperature rise. Model predicted dryout heat flux of the samples were validated against experimentally measured results and good agreement was shown with deviation within 20%. This indicated that the model accurately predicted the dryout heat flux.

Moreover, optimization was carried out for the micropillars in the evaporator and adiabatic regions, respectively. Sample with optimized micropillars d =17.4 µm, $h = l$ =30.6 µm in evaporator and d =15 µm, $h = l$ =30.6 µm in adiabatic region can handle a heat flux as high as 98.1 W/cm^2. The instantaneous response of RTD with heat flux increment and low temperature difference at various heat loads indicated that the silicon vapor chambers could dissipate heat flux with excellent temperature uniformity. The maximum temperature at condenser side was 9.64 K at 98.1 W. Condenser temperature at the water inlet of the copper cooler was lower than that at the water outlet. A higher *d/l* ratio and larger *h* were favorable in dissipating higher heat flux with lower temperature rise.

Moreover, thermal characterization of the biporous evaporators inside a vacuum chamber revealed that heat transfer coefficient increased with smaller microchannel width or larger micropillar island width. This can be explained by the increase of thin film evaporation areas. A competing effect between shorter liquid propagation distance and smaller evaporation area existed when the micropillar island became narrower. Similarly, the smaller pressure drop and reduction of thin film evaporation area were also

conversely related. Owing to the competing effects, optimal biporous evaporator geometries existed, biporous evaporator *sample 2* performed best with $q'' = 55.9$ W/cm^2 among the biporous evaporator samples when $2i$ =202 μm and $2w$ = 117 μm. Experimental measured dryout heat flux confirmed the prediction of the model with deviation less than 20%. Therefore, optimization in *Matlab* was conducted with the semianalytical model. Optimal geometries with superheat range of 5 – 30℃ for biporous evaporators were computed. Biporous evaporators were proven to have higher heat dissipation capabilities in comparison with uniform evaporators. 1.5 – 2 times higher dryout heat flux was demonstrated by biporous evaporators compared to that of uniform evaporators. Dryout area also expanded at slower rate for biporous evaporators. Therefore, higher dryout heat flux and better performance after dryout can be achieved by using biporous structures for evaporators.

Lastly, the wetting behavior of micropillar structures at superheated conditions were examined. The liquid droplets dispensed on micropillar surfaces were found to have 5 wetting regimes, with two peaks in its lifetime. The minimal heat transfer rate was found to occur at the non-wetting stage instead of Leidenfrost stage. The wetting of droplets changed from nucleate boiling to non-wetting at a much lower temperature (164 to 198 ˚C) compared to the Leidenfrost point on flat Si surface (290 ˚C). Both the transition temperature and Leidenfrost point were geometric dependent and increase with larger h and l. The transition of droplet wetting behavior at much lower temperature was attributed to the increased effective thermal conductivity of porous micropillar structures compared to vapor layer at Leidenfrost point. Higher micropillar h and l led to a decrease effective thermal conductivity of the porous layer, thus increase both Leidenfrost point and transition temperature.

In conclusions, this work extends our understandings of micropillar based uniform/biporous evaporators and silicon vapor chambers. Deep insights have been made in developing the model, conducting the optimization and thermally testing the evaporators and vapor chambers. Dual peak and various regimes of droplets on superheated micropillar structures was first reported. It can serve as important and useful

design guidance for silicon vapor chambers to address the thermal management issues of electronic devices.

7.2. Future Recommendations

The work reported in this thesis provides fundamental studies of uniform/biporous evaporators and silicon vapor chambers. Based on the understanding and insights obtained from this study, the following recommendations were proposed as future work:

a. The biporous evaporator studied in this thesis contained microchannels to shorten the liquid propagation distance and enhance dryout heat flux. However, this resulted in reduction of thin film evaporation area and lowered the heat transfer coefficient of the evaporator. As both higher dryout heat flux and larger heat transfer coefficient is preferred, micropillar structures with both local liquid reservoir and extended thin film evaporation areas are desired. This could be achieved by creating hierarchical structures on the evaporators, such as patterning the biporous evaporators with nanostructures on the micropillars. In this way, the liquid transportation can be maximized through the incorporation of microchannels, while at the same time, the evaporation areas are increased by the large thin film evaporation areas in the nanostructures.
b. The current study on silicon vapor chamber only considered the thin film evaporation regimes, as boiling regime with bubble formation is not desired due to the large thermal resistance of bubbles. However, the microchannels in biporous evaporators can also serve as vapor ventilation pathways. Therefore, the study can be extended to the boiling regime of biporous evaporators, which may facilitate heat dissipation with good vapor escaping via microchannels.
c. Visualization inside the vapor chamber and at the liquid meniscus interface can be made in the future. This can facilitate the understanding of vapor chamber dryout mechanisms and verify the assumptions adopted in developing the models.
d. Sealed silicon vapor chamber with uniform evaporator was fabricated and tested in this work. As a higher dryout heat flux can be dissipated with biporous evaporators compared to that of uniform evaporators, the evaporator with

biporous structures can be integrated in silicon vapor chamber. This can be a simple and promising way of enhancing the performance of silicon vapor chamber. Instead of parallel microchannels, leaf-vein structure microchannels can be designed to transport liquid back to the center evaporator.

e. Condenser side of our current silicon vapor chamber was smooth surface without any patterning. To facilitate droplet removal from the condenser and returning to the evaporator, surface modifications and patterning of condenser can be conducted to enhance its hydrophobicity. This can be achieved by depositing the condenser with superhydrophobic coating. Jumping droplet removal can be achieved to consistently expose the condenser surface through the surface modification and was reported by literatures [132, 133].

f. Silicon vapor chamber has been proved to be a reliable thermal management device with good performance and similar coefficient of thermal expansion (CTE) with semiconductor devices. However, the brittleness of silicon made the vapor chambers difficult to fabricate and hard to sustain the high-vacuum evacuation process. Thus, high mechanical strength materials without CTE mismatch with semiconductor materials should be considered in developing future vapor chambers. This made AlN an excellent candidate, which has high thermal conductivity (319 W/m·K) and excellent mechanical properties. AlN based vapor chambers with micropillar evaporators can be studied in the future.

References

[1] G. Moore, "The future of integrated electronics," *Fairchild Semiconductor internal publication,* vol. 2, 1964.

[2] K. Rupp, "40 Years of Microprocessor Trend Data," 2015. [online]. Available: https://www.karlrupp.net/2015/06/40-years-of-microprocessor-trend-data/. [Accessed: 20-May-2017].

[3] S.S. Anandan and V. Ramalingam, "Thermal management of electronics: A review of literature," *Thermal science,* vol. 12, pp. 5 – 26, 2008.

[4] "International Electronics Manufacturing Initiative Roadmap iNEMI Roadmap," 2002. [online]. Available: http://www.inemi.org/. [Accessed: 22-May-2017].

[5] M. Rosker, C. Bozada, H. Dietrich, A. Hung, D. Via, S. Binari*, et al.*, "The DARPA wide band gap semiconductors for RF applications (WBGS-RF) program: Phase II results," *CS ManTech,* vol. 1, 2009.

[6] "Report shows thermal mgmt growth by application," 2016. [online]. Available: https://www.electronicproducts.com/Thermal_Management/Heat_Sinks_and_Thermal_Materials/Report_shows_thermal_mgmt_growth_by_application.aspx. [Accessed: 25-May-2017].

[7] W.D. Jeakins and W.J.M. Moizer, "Cooling of electronic equipment," Google Patents, 2003.

[8] J. Michael J. Ellsworth, "High Powered Chip Cooling — Air and Beyond," 2005. [online]. Available: https://www.electronics-cooling.com/2005/08/high-powered-chip-cooling-air-and-beyond/. [Accessed: 25-May-2017].

[9] Semikron, "Water Cooling of Power Modules," 2013. [online]. Available: http://www.powerguru.org/water-cooling-of-power-modules/. [Accessed: 25-May-2017].

[10] E. N. Wang, L. Zhang, L. Jiang, J.M. Koo, J.G. Maveety, E.A. Sanchez*, et al.*, "Micromachined jets for liquid impingement cooling of VLSI chips," *Journal of Microelectromechanical systems,* vol. 13, pp. 833 – 842, 2004.

[11] L. Lin and R. Ponnappan, "Heat transfer characteristics of spray cooling in a closed loop," *International Journal of Heat and Mass Transfer,* vol. 46, pp. 3737 – 3746, 2003.

[12] C.E. Bash, C.D. Patel, and R.K. Sharma, "Inkjet assisted spray cooling of electronics," in *ASME 2003 International Electronic Packaging Technical Conference and Exhibition*, 2003, pp. 119 – 127.

[13] C. Gillot, C. Schaeffer, and A. Bricard, "Integrated micro heat sink for power multichip module," *IEEE transactions on industry applications,* vol. 36, pp. 217 – 221, 2000.

[14] K.H. Chu, "Micro and nanostructured surfaces for enhanced phase change heat transfer," Massachusetts Institute of Technology, 2013.

[15] L.E. Bell, "Cooling, heating, generating power, and recovering waste heat with thermoelectric systems," *Science,* vol. 321, pp. 1457 – 1461, 2008.

[16] H.S. Huang, Y.C. Weng, Y.W. Chang, S.L. Chen, and M.T. Ke, "Thermoelectric water-cooling device applied to electronic equipment," *International Communications in Heat and Mass Transfer,* vol. 37, pp. 140 – 146, 2010.

[17] D. Zhao and G. Tan, "A review of thermoelectric cooling: materials, modeling and applications," *Applied Thermal Engineering,* vol. 66, pp. 15 – 24, 2014.

[18] F.L. Tan and C. P. Tso, "Cooling of mobile electronic devices using phase change materials," *Applied Thermal Engineering,* vol. 24, pp. 159 – 169, 2004.

[19] R. Kandasamy, X.Q. Wang, and A.S. Mujumdar, "Transient cooling of electronics using phase change material (PCM)-based heat sinks," *Applied Thermal Engineering,* vol. 28, pp. 1047 – 1057, 2008.

[20] J. M. Ochterbeck, "Heat pipes," *Heat Transfer Handbook,* vol. 1, 2003.

[21] Q. Cai and Y.C. Chen, "Investigations of biporous wick structure dryout," *Journal of Heat Transfer,* vol. 134, p. 021503, 2012.

[22] T. Semenic and I. Catton, "Experimental study of biporous wicks for high heat flux applications," *International Journal of Heat and Mass Transfer,* vol. 52, pp. 5113 – 5121, 2009.

[23] R. Manimaran, K. Palaniradja, N. Alagumurthi, and J. Hussain, "Factors affecting the thermal performance of heat pipe – a review," *Journal of Engineering Research and Studies,* vol. 3, pp. 20 – 24, 2012.

[24] A. Bar Cohen, A. Watwe, and K.N. Seetharamu, "Fundamentals of thermal management," *Fundamentals of Microsystems of Package, RR Tummala, ed., McGraw – Hill, New York,* 2001.

[25] S. W. Kang, W.C. Wei, S.H. Tsai, and S.Y. Yang, "Experimental investigation of silver nano-fluid on heat pipe thermal performance," *Applied Thermal Engineering,* vol. 26, pp. 2377 – 2382, 2006.

[26] Y.S. Chen, K.H. Chien, C.C. Wang, T.C. Hung, and B.S. Pei, "A simplified transient three-dimensional model for estimating the thermal performance of the vapor chambers," *Applied thermal engineering,* vol. 26, pp. 2087 – 2094, 2006.

[27] R. S. Prasher, "A simplified conduction based modeling scheme for design sensitivity study of thermal solution utilizing heat pipe and vapor chamber technology," *Transactions-American Society of Mechanical Engineers Journal of Electronic Packaging,* vol. 125, pp. 378 – 385, 2003.

[28] J. C. Wang and R. T. Wang, "A novel formula for effective thermal conductivity of vapor chamber," *Experimental Techniques,* vol. 35, pp. 35 – 40, 2011.

[29] R. Ranjan, J.Y. Murthy, S.V. Garimella, D.H. Altman, and M.T. North, "Modeling and design optimization of ultrathin vapor chambers for high heat flux applications," *IEEE Transactions on Components, Packaging and Manufacturing Technology,* vol. 2, pp. 1465 – 1479, 2012.

[30] X. Ji, J. Xu, A. M. Abanda, and Q. Xue, "A vapor chamber using extended condenser concept for ultra-high heat flux and large heater area," *International Journal of Heat and Mass Transfer,* vol. 55, pp. 4908 – 4913, 2012.

[31] S.S. Hsieh, R.Y. Lee, J.C. Shyu, and S.W. Chen, "Thermal performance of flat vapor chamber heat spreader," *Energy Conversion and Management,* vol. 49, pp. 1774 – 1784, 2008.

[32] Y.T. Chen, J.M. Miao, D.Y. Ning, T.F. Chu, and W.E. Chen, "Thermal performance of a vapor chamber heat pipe with diamond-copper composition wick structures," in *Microsystems, Packaging, Assembly and Circuits Technology Conference, 2009. IMPACT 2009. 4th International*, 2009, pp. 340 – 343.

[33] J.S. Go, "Quantitative thermal performance evaluation of a cost-effective vapor chamber heat sink containing a metal-etched microwick structure for advanced microprocessor cooling," *Sensors and Actuators A: Physical,* vol. 121, pp. 549 – 556, 2005.

[34] Y.S. Ju, M. Kaviany, Y. Nam, S. Sharratt, G. Hwang, I. Catton*, et al.*, "Planar vapor chamber with hybrid evaporator wicks for the thermal management of high-heat-flux and high-power optoelectronic devices," *International Journal of Heat and Mass Transfer,* vol. 60, pp. 163 – 169, 2013.

[35] P. Naphon, S. Wongwises, and S. Wiriyasart, "On the thermal cooling of central processing unit of the PCs with vapor chamber," *International Communications in Heat and Mass Transfer,* vol. 39, pp. 1165 – 1168, 2012.

[36] S.C. Wong, K.C. Hsieh, J.D. Wu, and W.L. Han, "A novel vapor chamber and its performance," *International Journal of Heat and Mass Transfer,* vol. 53, pp. 2377 – 2384, 2010.

[37] Y. Tang, D. Yuan, L. Lu, and Z. Wang, "A multi-artery vapor chamber and its performance," *Applied Thermal Engineering,* vol. 60, pp. 15 – 23, 2013.

[38] M. Sigurdson, Y. Liu, P. Bozorgi, D. Bothman, N. MacDonald, and C. Meinhart, "A large scale titanium thermal ground plane," *International Journal of Heat and Mass Transfer,* vol. 62, pp. 178 – 183, 2013.

[39] Y.S. Chen, K.H. Chien, C.C. Wang, T.C. Hung, Y.M. Ferng, and B.S. Pei, "Investigations of the thermal spreading effects of rectangular conduction plates and vapor chamber," *Journal of Electronic Packaging,* vol. 129, pp. 348 – 355, 2007.

[40] M. Lu, L. Mok, and R. Bezama, "A graphite foams based vapor chamber for chip heat spreading," *Journal of Electronic Packaging,* vol. 128, pp. 427 – 431, 2006.

[41] C. Ding, G. Soni, P. Bozorgi, B. D. Piorek, C. D. Meinhart, and N. C. MacDonald, "A flat heat pipe architecture based on nanostructured titania," *Journal of Microelectromechanical Systems,* vol. 19, pp. 878 – 884, 2010.

[42] Y.T. Chen, S.W. Kang, Y.H. Hung, C.H. Huang, and K.C. Chien, "Feasibility study of an aluminum vapor chamber with radial grooved and sintered powders wick structures," *Applied Thermal Engineering,* vol. 51, pp. 864 – 870, 2013.

[43] J.Y. Chang, R. S. Prasher, S. Prstic, P. Cheng, and H. Ma, "Evaporative thermal performance of vapor chambers under nonuniform heating conditions," *Journal of Heat Transfer,* vol. 130, p. 121501, 2008.

[44] X. Ji, J. Xu, and A.M. Abanda, "Copper foam based vapor chamber for high heat flux dissipation," *Experimental Thermal and Fluid Science,* vol. 40, pp. 93 – 102, 2012.

[45] Z. Sun and H. Qiu, "An asymmetrical vapor chamber with multiscale micro/nanostructured surfaces," *International Communications in Heat and Mass Transfer,* vol. 58, pp. 40 – 44, 2014.

[46] C. Oshman, Q. Li, L.A. Liew, R. Yang, Y. Lee, V. M. Bright*, et al.*, "Thermal performance of a flat polymer heat pipe heat spreader under high acceleration," *Journal of Micromechanics and Microengineering,* vol. 22, p. 045018, 2012.

[47] C. Oshman, Q. Li, L.A. Liew, R. Yang, Y. Lee, and V.M. Bright, "Flat Polymer Heat Spreader with High Aspect Ratio Micro Hybrid Wick Operating Under Adverse Gravity," in *ASME 2011 International Mechanical Engineering Congress and Exposition*, 2011, pp. 601 – 606.

[48] C. Oshman, Q. Li, L.A. Liew, R. Yang, V.M. Bright, and Y. Lee, "Flat flexible polymer heat pipes," *Journal of Micromechanics and Microengineering,* vol. 23, p. 015001, 2012.

[49] C. Oshman, B. Shi, C. Li, R. Yang, Y. Lee, G. Peterson*, et al.*, "The development of polymer-based flat heat pipes," *Journal of Microelectromechanical Systems,* vol. 20, pp. 410 – 417, 2011.

[50] S.S. Hsieh and Y.R. Yang, "Design, fabrication and performance tests for a polymer-based flexible flat heat pipe," *Energy Conversion and Management,* vol. 70, pp. 10 – 19, 2013.

[51] K.S. Yang, T.Y. Yang, C.W. Tu, C.T. Yeh, and M.T. Lee, "A novel flat polymer heat pipe with thermal via for cooling electronic devices," *Energy Conversion and Management,* vol. 100, pp. 37 – 44, 2015.

[52] U. Vadakkan, G.M. Chrysler, and S. Sane, "Silicon/water vapor chamber as heat spreaders for microelectronic packages," in *Semiconductor Thermal*

Measurement and Management Symposium, 2005 IEEE Twenty First Annual IEEE, 2005, pp. 182 – 186.

[53] Q. Cai, B.C. Chen, C. Tsai, and C.L. Chen, "Development of scalable silicon heat spreader for high power electronic devices," *Journal of Thermal Science and Engineering Applications,* vol. 1, p. 041009, 2009.

[54] Q. Cai, B.C. Chen, and C. Tsai, "Design, development and tests of high–performance silicon vapor chamber," *Journal of Micromechanics and Microengineering,* vol. 22, p. 035009, 2012.

[55] Q. Cai, A. Bhunia, C. Tsai, M.W. Kendig, and J. F. DeNatale, "Studies of material and process compatibility in developing compact silicon vapor chambers," *Journal of Micromechanics and Microengineering,* vol. 23, p. 065003, 2013.

[56] S.Q. Cai, Y.C. Chen, and A. Bhunia, "Design, development and tests of a compact thermofluid system," *Applied Thermal Engineering,* vol. 102, pp. 1320 – 1327, 2016.

[57] K.S. Yang, K.L. Ho, K.H. Chien, and J.C. Shyu, "Heat transfer of vapor chamber with different types of microchannels," *International Journal of Green Energy,* vol. 13, pp. 1325 – 1333, 2016.

[58] Frostytech, "Heatpipe Wick Structures Exposed: Sintered, Groove and Mesh." [online]. Available: http://www.frostytech.com/articleview.cfm?articleID=2466. [Accessed: 01-Jun-2017].

[59] Y. Nam, S. Sharratt, C. Byon, S.J. Kim, and Y.S. Ju, "Fabrication and characterization of the capillary performance of superhydrophilic Cu micropost arrays," *Microelectromechanical Systems, Journal of,* vol. 19, pp. 581 – 588, 2010.

[60] D. Ćoso, V. Srinivasan, M.C. Lu, J.Y. Chang, and A. Majumdar, "Enhanced heat transfer in biporous wicks in the thin liquid film evaporation and boiling regimes," *Journal of Heat Transfer,* vol. 134, p. 101501, 2012.

[61] A. Sangani and A. Acrivos, "Slow flow past periodic arrays of cylinders with application to heat transfer," *International journal of Multiphase flow,* vol. 8, pp. 193 – 206, 1982.

[62] J. E. Drummond and M.I. Tahir, "Laminar viscous flow through regular arrays of parallel solid cylinders," *International Journal of Multiphase Flow,* vol. 10, pp. 515 – 540, 1984.

[63] B. Gebart, "Permeability of unidirectional reinforcements for RTM," *Journal of composite materials,* vol. 26, pp. 1100 – 1133, 1992.

[64] K. Yazdchi, S. Srivastava, and S. Luding, "Microstructural effects on the permeability of periodic fibrous porous media," *International Journal of Multiphase Flow,* vol. 37, pp. 956 – 966, 2011.

[65] K. Yazdchi, S. Srivastava, and S. Luding, "Micro-macro relations for flow through random arrays of cylinders," *Composites Part A: Applied Science and Manufacturing,* vol. 43, pp. 2007 – 2020, 2012.

[66] M. Sobera and C. Kleijn, "Hydraulic permeability of ordered and disordered single-layer arrays of cylinders," *Physical Review E,* vol. 74, p. 036301, 2006.

[67] A. Tamayol, J. Yeom, M. Akbari, and M. Bahrami, "Low Reynolds number flows across ordered arrays of micro-cylinders embedded in a rectangular micro/minichannel," *International Journal of Heat and Mass Transfer,* vol. 58, pp. 420 – 426, 2013.

[68] A. Tamayol and M. Bahrami, "Analytical determination of viscous permeability of fibrous porous media," *International Journal of Heat and Mass Transfer,* vol. 52, pp. 2407 – 2414, 2009.

[69] C. Zhang, "Analytical and experimental investigation of capillary forces induced by nanopillars for thermal management applications," 2010.

[70] R. Xiao, R. Enright, and E.N. Wang, "Prediction and optimization of liquid propagation in micropillar arrays," *Langmuir,* vol. 26, pp. 15070 – 15075, 2010.

[71] N. Srivastava, C. Din, A. Judson, N. C. MacDonald, and C. D. Meinhart, "A unified scaling model for flow through a lattice of microfabricated posts," *Lab on a Chip,* vol. 10, pp. 1148 – 1152, 2010.

[72] R. Hale, R. Bonnecaze, and C. Hidrovo, "Optimization of capillary flow through square micropillar arrays," *International Journal of Multiphase Flow,* vol. 58, pp. 39 – 51, 2014.

[73] R. Ranjan, A. Patel, S.V. Garimella, and J.Y. Murthy, "Wicking and thermal characteristics of micropillared structures for use in passive heat spreaders," *International Journal of Heat and Mass Transfer,* vol. 55, pp. 586 – 596, 2012.

[74] C. Byon and S.J. Kim, "The effect of meniscus on the permeability of micro-post arrays," *Journal of Micromechanics and Microengineering,* vol. 21, p. 115011, 2011.

[75] S. Adera, D. Antao, R. Raj, and E.N. Wang, "Design of micropillar wicks for thin-film evaporation," *International Journal of Heat and Mass Transfer,* vol. 101, pp. 280 – 294, 2016.

[76] Y. Zhu, D.S. Antao, Z.Lu, S. Somasundaram, T. Zhang, and E.N. Wang, "Prediction and Characterization of Dry-out Heat Flux in Micropillar Wick Structures," *Langmuir,* vol. 32, pp. 1920 – 1927, 2016.

[77] Y. Nam and Y.S. Ju, "Fabrication and characterization of superhydrophilic Cu microposts for micro heat pipes," *Proc. PowerMEMS,* pp. 1 – 4, 2009

[78] Y. Nam, S. Sharratt, G. Cha, and Y.S. Ju, "Characterization and modeling of the heat transfer performance of nanostructured Cu micropost wicks," *Journal of Heat Transfer,* vol. 133, p. 101502, 2011.

[79] S.Q. Cai and A. Bhunia, "Geometrical effects of wick structures on the maximum phase change capability," *International Journal of Heat and Mass Transfer,* vol. 79, pp. 981 – 988, 2014.

[80] S. Ravi, D. Horner, and S. Moghaddam, "Monoporous micropillar wick structures, I – Mass transport characteristics," *Applied Thermal Engineering,* vol. 73, pp. 1371 – 1377, 2014.

[81] D. Horner, S. Ravi, and S. Moghaddam, "Monoporous micropillar wick structures, II optimization & theoretical limits," *Applied Thermal Engineering,* 2014.

[82] X. Cao, P. Cheng, and T. Zhao, "Experimental study of evaporative heat transfer in sintered copper bidispersed wick structures," *Journal of thermophysics and heat transfer,* vol. 16, pp. 547 – 552, 2002.

[83] T. Semenic, Y.Y. Lin, I. Catton, and D.B. Sarraf, "Use of biporous wicks to remove high heat fluxes," *Applied Thermal Engineering,* vol. 28, pp. 278 – 283, 2008.

[84] T. Semenic, Y.Y. Lin, and I. Catton, "Thermophysical properties of biporous heat pipe evaporators," *Journal of Heat Transfer,* vol. 130, p. 022602, 2008.

[85] S. W. Reilly and I. Catton, "Improving Biporous Heat Transfer by Addition of Monoporous Interface Layer," in *ASME 2009 Heat Transfer Summer Conference collocated with the InterPACK09 and 3rd Energy Sustainability Conferences*, 2009, pp. 327 – 333.

[86] J. Wang and I. Catton, "Evaporation heat transfer in thin biporous media," *Heat and mass transfer,* vol. 37, pp. 275 – 281, 2001.

[87] T. Semenic, Y.Y. Lin, and I. Catton, "Biporous sintered copper for closed loop heat pipe evaporator," in *ASME 2005 International Mechanical Engineering Congress and Exposition*, 2005, pp. 21 – 25.

[88] C.C. Yeh, C.N. Chen, and Y.M. Chen, "Heat transfer analysis of a loop heat pipe with biporous wicks," *International Journal of Heat and Mass Transfer,* vol. 52, pp. 4426 – 4434, 2009.

[89] B. Chen, Z. Liu, W. Liu, J. Yang, H. Li, and D. Wang, "Operational characteristics of two biporous wicks used in loop heat pipe with flat evaporator," *International Journal of Heat and Mass Transfer,* vol. 55, pp. 2204 – 2207, 2012.

[90] Z. Liu, H. Li, B. Chen, J. Yang, and W. Liu, "Operational characteristics of flat type loop heat pipe with biporous wick," *International Journal of Thermal Sciences,* vol. 58, pp. 180 – 185, 2012.

[91] H. Li, Z. Liu, B. Chen, W. Liu, C. Li, and J. Yang, "Development of biporous wicks for flat-plate loop heat pipe," *Experimental Thermal and Fluid Science,* vol. 37, pp. 91 – 97, 2012.

[92] C. Byon and S.J. Kim, "Capillary performance of bi-porous sintered metal wicks," *International Journal of Heat and Mass Transfer,* vol. 55, pp. 4096 – 4103, 2012.

[93] Q. Cai, Y. Zhao, C. Tsai, and C.I. Chen, "Investigations of high heat flux cooling using carbon nanotube Bi-wick structure and integrated platinum thermometer/heater," in *ASME 2009 Heat Transfer Summer Conference collocated with the InterPACK09 and 3rd Energy Sustainability Conferences*, 2009, pp. 451 – 457.

[94] Q. Cai and C.L. Chen, "Design and test of carbon nanotube biwick structure for high-heat-flux phase change heat transfer," *Journal of Heat Transfer,* vol. 132, p. 052403, 2010.

[95] C. Byon and S.J. Kim, "Study on the capillary performance of micro-post wicks with non-homogeneous configurations," *International Journal of Heat and Mass Transfer,* vol. 68, pp. 415 – 421, 2014.

[96] S. Ravi, R. Dharmarajan, and S. Moghaddam, "Physics of fluid transport in hybrid biporous capillary wicking microstructures," *Langmuir,* vol. 32, pp. 8289 – 8297, 2016.

[97] "Development of scalable silicon heat spreader for high power electronic devices," *Journal of Thermal Science and Engineering Applications,* vol. 1, 2010.

[98] C. Miers, G. Wehmeyer, and C.H. Hidrovo, "A novel thermo-hydraulic test platform for micropillared array thermal wick optimization," in *ASME 2012 10th International Conference on Nanochannels, Microchannels, and Minichannels collocated with the ASME 2012 Heat Transfer Summer Conference and the ASME 2012 Fluids Engineering Division Summer Meeting*, 2012, pp. 827 – 834.

[99] C. Ding, G. Soni, P. Bozorgi, B.D. Piorek, C.D. Meinhart, and N.C. MacDonald, "A flat heat pipe architecture based on nanostructured titania," *Microelectromechanical Systems, Journal of,* vol. 19, pp. 878 – 884, 2010.

[100] B. Chen, W. Liu, Z. Liu, H. Li, and J. Yang, "Experimental investigation of loop heat pipe with flat evaporator using biporous wick," *Applied Thermal Engineering,* vol. 42, pp. 34 – 40, 2012.

[101] Y. Wang and G. Peterson, "Analytical model for capillary evaporation limitation in thin porous layers," *Journal of thermophysics and heat transfer,* vol. 17, pp. 145 – 149, 2003.

[102] E.W. Washburn, "The dynamics of capillary flow," *Physical review,* vol. 17, p. 273, 1921.

[103] R. Ranjan, J.Y. Murthy, and S.V. Garimella, "A microscale model for thin-film evaporation in capillary wick structures," *International Journal of Heat and Mass Transfer,* vol. 54, pp. 169 – 179, 2011.

[104] P.C. Wayner, "Intermolecular forces in phase-change heat transfer: 1998 Kern award review," *AIChE journal,* vol. 45, pp. 2055 – 2068, 1999.

[105] M. Potash Jr and P. Wayner Jr, "Evaporation from a two-dimensional extended meniscus," *International Journal of Heat and Mass Transfer,* vol. 15, pp. 1851 – 1863, 1972.

[106] Q. Cai, Y.C. Chen, C. Tsai, and J.F. DeNatale, "Development of a platinum resistance thermometer on the silicon substrate for phase change studies," *Journal of Micromechanics and Microengineering,* vol. 22, p. 085012, 2012.

[107] E.R. Murphy, T. Inoue, H.R. Sahoo, N. Zaborenko, and K.F. Jensen, "Solder-based chip-to-tube and chip-to-chip packaging for microfluidic devices," *Lab on a Chip,* vol. 7, pp. 1309 – 1314, 2007.

[108] H.W. Coleman and W.G. Steele, *Experimentation, validation, and uncertainty analysis for engineers*: John Wiley & Sons, 2009.

[109] R.N. Wenzel, "Resistance of solid surfaces to wetting by water," *Industrial & Engineering Chemistry,* vol. 28, pp. 988 – 994, 1936.

[110] R. Raj, S.C. Maroo, and E.N. Wang, "Wettability of graphene," *Nano letters,* vol. 13, pp. 1509 – 1515, 2013.

[111] R. Ranjan, J.Y. Murthy, and S.V. Garimella, "Analysis of the wicking and thin-film evaporation characteristics of microstructures," *Journal of Heat Transfer,* vol. 131, p. 101001, 2009.

[112] D.S. Antao, S. Adera, E. Farias, R. Raj, and E.N. Wang, "Visualization of the Evaporating Liquid-Vapor Interface in Micropillar Arrays," *Journal of Heat Transfer,* vol. 138, p. 020910, 2016.

[113] R. Xiao and E.N. Wang, "Microscale liquid dynamics and the effect on macroscale propagation in pillar arrays," *Langmuir,* vol. 27, pp. 10360 – 10364, 2011.

[114] C. Ward and F. Duan, "Turbulent transition of thermocapillary flow induced by water evaporation," *Physical Review E,* vol. 69, p. 056308, 2004.

[115] M. Wei, S. Somasundaram, B. He, Q. Liang, C.S. Tan, and E.N. Wang, "Experimental characterization of Si micropillar based evaporator for advanced vapor chambers," in *Electronics Packaging Technology Conference (EPTC), 2014 IEEE 16th*, 2014, pp. 335 – 340.

[116] M. Wei, B. He, S. Somasundaram, C.S. Tan, and E.N. Wang, "Optimization and thermal characterization of uniform micropillar based silicon evaporator in advanced vapor chambers," in *2016 15th IEEE Intersociety Conference on Thermal and Thermomechanical Phenomena in Electronic Systems (ITherm)*, 2016, pp. 1019 – 1023.

[117] G.A. Lindeboom, *Herman Boerhaave: The man and his work*: Methuen, 1968.

[118] J.G. Leidenfrost, *De aquae communis nonnullis qualitatibus tractatus*: Ovenius, 1756.

[119] S. Zhang and G. Gogos, "Film evaporation of a spherical droplet over a hot surface: fluid mechanics and heat/mass transfer analysis," *Journal of Fluid Mechanics,* vol. 222, pp. 543 – 563, 1991.

[120] I. U. Vakarelski, N. A. Patankar, J.O. Marston, D.Y. Chan, and S.T. Thoroddsen, "Stabilization of Leidenfrost vapour layer by textured superhydrophobic surfaces," *Nature,* vol. 489, p. 274, 2012.

[121] H. Kim, B. Truong, J. Buongiorno, and L.W. Hu, "On the effect of surface roughness height, wettability, and nanoporosity on Leidenfrost phenomena," *Applied Physics Letters,* vol. 98, p. 083121, 2011.

[122] C. Aberle, M. Lewis, G. Yu, N. Lei, and J. Xu, "Liquid marbles as thermally robust droplets: coating-assisted Leidenfrost-like effect," *Soft Matter,* vol. 7, pp. 11314 – 11318, 2011.

[123] A.L. Biance, C. Clanet, and D. Quéré, "Leidenfrost drops," *Physics of Fluids,* vol. 15, pp. 1632 – 1637, 2003.

[124] G. Duursma, R. Kennedy, K. Sefiane, and Y. Yu, "Leidenfrost droplets on microstructured surfaces," *Heat Transfer Engineering,* vol. 37, pp. 1190 – 1200, 2016.

[125] Z. Tamura and Y. Tanasawa, "Evaporation and combustion of a drop contacting with a hot surface," in *Symposium (International) on Combustion*, 1958, pp. 509 – 522.

[126] G. Liu and V.S. Craig, "Macroscopically flat and smooth superhydrophobic surfaces: Heating induced wetting transitions up to the Leidenfrost temperature," *Faraday discussions,* vol. 146, pp. 141 – 151, 2010.

[127] C. Kruse, T. Anderson, C. Wilson, C. Zuhlke, D. Alexander, G. Gogos*, et al.*, "Extraordinary shifts of the Leidenfrost temperature from multiscale micro/nanostructured surfaces," *Langmuir,* vol. 29, pp. 9798 – 9806, 2013.

[128] I.W. Park, M. Fernandino, and C.A. Dorao, "Effect of Micropillar Characteristics on Leidenfrost Temperature of Impacting Droplets," in *ASME 2016 14th International Conference on Nanochannels, Microchannels, and Minichannels collocated with the ASME 2016 Heat Transfer Summer Conference and the ASME 2016 Fluids Engineering Division Summer Meeting*, 2016, pp. V001T09A001 – V001T09A001.

[129] S. Adera, R. Raj, R. Enright, and E.N. Wang, "Non-wetting droplets on hot superhydrophilic surfaces," *Nature communications,* vol. 4, p. 2518, 2013.

[130] C. Glassbrenner and G.A. Slack, "Thermal conductivity of silicon and germanium from 3 K to the melting point," *Physical Review,* vol. 134, p. A1058, 1964.

[131] R. Williams and A.M. Goodman, "Wetting of thin layers of SiO_2 by water," *Applied Physics Letters,* vol. 25, pp. 531 – 532, 1974.

[132] N. Miljkovic, R. Enright, Y. Nam, K. Lopez, N. Dou, J. Sack*, et al.*, "Jumping-droplet-enhanced condensation on scalable superhydrophobic nanostructured surfaces," *Nano letters,* vol. 13, pp. 179 – 187, 2012.

[133] N. Miljkovic, D.J. Preston, R. Enright, and E.N. Wang, "Jumping-droplet electrostatic energy harvesting," *Applied Physics Letters,* vol. 105, p. 013111, 2014.